工學博士學位論文

Fabrication of Multidimensional Conducting Polymer Nanomaterials *via* Vapor Deposition Polymerization and Their Chem/Bio Sensor Applications

기상 증착 중합을 통한 다차원적인 전도성 고분자
나노 물질의 제조 및 화학/바이오 센서로의 응용

2014年 8月

서울大學校 大學院

化學生物工學部

朴 先 珠

Fabrication of Multidimensional Conducting Polymer Nanomaterials *via* Vapor Deposition Polymerization and Their Chem/Bio Sensor Applications

기상 증착 중합을 통한 다차원적인 전도성 고분자
나노 물질의 제조 및 화학/바이오 센서로의 응용

指導敎授: 張 正 植

이 論文을 工學博士 學位論文으로 提出함

2014年 5月

서울大學校 大學院

化學生物工學部

朴 先 珠

朴 先 珠의 工學博士 學位論文을 認准함
2014年 5月

委 員 長 _____ (인)

副委員長 _____ (인)

委   員 _____ (인)

委   員 _____ (인)

委   員 _____ (인)

**Fabrication of Multidimensional Conducting Polymer
Nanomaterials via Vapor Deposition Polymerization
and Their Chem/Bio Sensor Applications**

by

Seon Joo Park

Submitted to the Graduate School of Seoul National University

in Partial Fulfillment of the Requirements

for the Degree of Doctor of Philosophy

August, 2014

Thesis Adviser: Jyongsik Jang

ABSTRACT

Conducting polymer (CP) have received significant attention, owing to their unusual physical and chemical properties such as rapid charge transfer, stability toward environmental shocks, and biocompatibility. Compared to conventional polymers, CPs can be conductive through a conjugated bond system along the polymer backbone which is composed of alternating single and double bonds along the polymer chain. Among various CPs, poly(3,4-ethylenedioxythiophene) (PEDOT) and polypyrrole (PPy) can be specialized by long-term stability of their conductivity and facile surface-modification. From the point of materials, many researchers have investigated various synthesis strategies of CP nanomaterials to control their morphologies. Template-assisted methodologies are a very promising and powerful tool to design CP nanomaterials because of their easy treatments. Especially, vapor deposition polymerization (VDP) approach using nanotemplates offers a polymer thin-film or shell on the surface of the nanotemplates. Compared to a solvent-process, VDP approach can prevent pinhole defects and cloudiness, so it creates CP nanomaterials with an ideal and controllable surface morphology.

VDP also has many advantages in environmental and healthful concerns because a solvent-related material is harmful and wasteful in environmental concerns, relatively. Interestingly, the expected surface morphologies, including smooth or multidimensional surface, in the deposited CP layers are formed by the consecutive polymerization of vaporized monomer on the nanotemplates under designed vacuum and temperature. In this study, various strategies for new polymeric morphologies are introduced by controlling critical kinetic factors (amount of monomer, a temperature, and a pressure) during VDP process

Such attractive electrical/chemical properties of CP nanomaterials enable to be applied in an electrochemical analysis, leading to the high-performance transistors in the field of chemical and biological sensors. Moreover, oxidation level of CP nanomaterials is affected by chemical and electrochemical doping/dedoping mechanisms, resulting in highly sensitivity and rapid response/recovery time toward target analytes. Furthermore, the enlarged surface area from unique morphologies of multidimensional CP nanomaterials can provide the enhanced interactions to the analytes, leading to the cutting

edge of ultrasensitive sensing geometries.

KEYWORDS: Conducting polymers (CP) ; Nanomaterials; Vapor deposition

polymerization (VDP); Poly(3,4-ethylenedioxythiophene) (PEDOT);

Polypyrrole (PPy), Sensor, Field-effect transistor (FET)

STUDENT NUMBER: 2009–23949

List of Abbreviations

AAO : anodic aluminum oxide

APS : (3-aminopropyl) trimethoxysilane

CPPy : carboxylated polypyrrole

DMF : dimethyl formamide

DMMP : dimethyl methylphosphonate

DMT-MM : 4-(4,6-Dimethoxy-1,3,5-triazin-2-yl)-4-methyl-morpholinium chloride

DR : dopamine receptor

EDOT : 3,4-ethylenedioxythiophene

FE-SEM : field−emission scanning electron microscope

FET : field effect transistor

HEDOT : hydroxylated 3,4-ethylenedioxythiophene

HPNT : hydroxylated PEDOT

MCPEDOT : multidimensional carboxylated PEDOT

MDCP : dichlorophosphate

MFC : mass flow controllers

MPNS : MPPy NT-integrated chemiresistive sensors

MPPy : multidimensional Polypyrrole

ND : nanonodule

NF : nanofiber

NN : nanonodule

NP : nanoparticles

NR : nanorod

NT : nanotube

NW : nanowire

P3CA : pyrrole-3-carboxylicacid

PCA : 1-Pyrenecarboxylic acid

PCA : principal components analysis

PCCN : Pd NPs–CPPy–CNTnanohybrids

PDMS : poly(dimethylsiloxane)

PEDOT : Poly(3,4-ethylenedioxythiophene)

PET : poly(ethylene terephthalate)

PMMA : poly(methyl methacrylate)

PPy : polypyrrole

PVA : poly(vinyl alcohol)

RH : relative humidity

SEM : scanning electron microscope

SL : smooth layer

SM : smooth

TCP : trichlorophosphate

TEM : transmission electron microscope

TMP : trimethyl phosphate

VDP : vapor deposition polymerization

Vds : drain-source voltage

Vg : gate voltage

VOCs : volatile organic compounds

XPS : X−ray photoelectron spectra

XRD : X-ray diffraction

List of Figures

PEDOT nanostructures. The PMMA nanofibers function as template as well as substrate for the growth of PEDOT under different synthetic conditions (temperature and pressure).

PMMA/silicon wafer.

times and measuring it on a flat state. The concentration of DMMP was 100 ppt. The real-time responses were measured by the data based on the parallel resistances (Ry direction). (b) Representative photographs showing finger motions during fatigue test.

0.1 to -1 V in a step of -0.1 V and V_{ds} scan rate was -5 mV s^{-1}).

NTs prepared with 5 and 30% (wt/wt).

Photoresist was deposited on the silicon wafer and patterned by photolithography. d) and e) The fabrication of PDMS sensing substrate. f) The holes are punched for efficient flow of the analyte.

value was reached after exposure to gases.

List of Tables

Table of Contents

1. INTRODUCTION

1.1. Background

1.1.1. Conducting polymer nanomaterials

The greatest challenge in designing molecular-based materials is to predict and control the synthesis of precise assemblies that have well-defined nanostructures and functions.[1-8] From a material viewpoint, the advancement of science and technology provides the smaller dimensions with higher surface area and enhanced performance.[9] For example, in the case of 30 nm size of a particle, about 10 % of its molecules are existed on the surface, whereas at 10 and 3 nm-diameter the ratio increase to 20 % and 50 %, respectively.[10] As the particle size decreased, the number of molecules expressed on the surface of the particle surface exponentially increased. The increase in surface area determines the potential number of reactive groups on the particle surface. The precise size control of materials at the nanometer level leads to superior physical and chemical properties that are quite different from those of their bulky system due to increase in surface to volume ratio exponentially.[11-12] The properties of nanoscopically defined systems are determined by their size, shape, morphology, and composition, which determine their potential applications in optics,[2] electronics,[3] catalysis,[4] sensors,[5-7] and medical diagnostics.[8]These phenomena arise from the quantum chemical effects

1

including quantum confinement and finite size effect as well as the nano-sized filler effect.[13-14] Novel nanostructured materials and devices with the enhanced capabilities can be generated by a combination of nanobuilding units and strategies for assembling them. Currently, nanotechnology is concerned with fabrication and various applications of functional materials and structures in the range of 1 nm to 100 nm using chemical and physical methods.[15-17] Nanomaterials include nanoparticle, core-shell nanostructure, hollow nanosphere, nanofiber, nanotube, nanopattern, nanocomposite, and so forth. They are divided into nanosized metal, inorganic material, semiconductor, biomaterial, oligomer and polymer, etc. Especially, among various types of nanomaterials, conducting polymer nanomaterials have received significant attention, due to their useful properties, such as excellent electrical property,[18] stability,[19-20] and biocompatibility.[21-22] It is rendered conductive through a conjugated bond system along the polymer backbone which is composed of alternating single and double bonds along the polymer chain.[23-24] They are typically formed either through chemical oxidation of the monomer (for example with iron chloride) or electrochemical oxidation of the monomer.[25] Two oxidation reactions occur simultaneously the oxidation of the monomer and the oxidation of the polymer with the coincident insertion of a dopant/counter ion (e.g. Cl-).[26] The dopant or doping level (in the p-type

conducing polymer) is typically below 1 dopant per polymer unit: approximately 0.3-0.5, i.e., 2-3 monomer units per dopant. This is limited by how closely the positive charges (so-called polarons) can be spaced along the polymer chain. Polyacetylene was the beginning of the conductive polymer with the simplest form. Molecular structures of these typical conducting polymers are shown by Table 1.

1.1.1.1. Poly(3,4-ethylenedioxythiophene) (PEDOT)

PEDOT had been developed as one of the PT derivatives by the Bayer AG research laboratories in Germany during the 1980s.[27, 28] It has been recognized as one of the most promising candidates for practical applications owing to its remarkable conductivity and air stability,[29] It was prepared using standard oxidative or electrochemical polymerization methods. Initially, it was found to be an insoluble polymer, yet exhibited some very interesting properties such as high conductivity (*ca*. 300 S cm^{-1}), transparency in oxidized thin film, and excellent stability in an oxidized state. The solubility problem was subsequently overcome by a water-soluble polyelectrolyte such as PSS and this polyelectrolyte was used as the charge-balancing dopant during polymerization to form a PEDOT/PSS solution. The combination of PEDOT and PSS electrolyte resulted in a water-soluble conducting polymer with good

film forming properties: conductivity (*ca.* 10 S cm^{-1}), high visible light transmittance, and excellent stability. It has previously been reported the novel electrical properties of various functionalized PEDOT nanostructures.[30-32]

1.1.1.2. Polypyrrole (PPy)

Of all known conducting polymer, polypyrrole is the most frequently used in commercial applications due to the long-term stability of its conductivity and the possibility of forming homopolymers of composites with optimal mechanical properties. PPy was firstly synthesized in 1912.[33] Electrical conductivity of materials is determined by its structure and proportional to the ability of charge transport.[34] Charge transport is performed by the charge carrier which is an electron of hole in the majority of conductors so the spin number of the charge carriers is 1/2. It was, however, reported that the charge carrier in PPy is spinless and has a positive sign, which means that the charge carrier in PPy is not unpaired electron.[35] To explain the electronic phenomena in PPy, new entity of the charge carrier was claimed and finally identified, called bipolaron.

The concentration of charge carrier in PPy depends on the oxidation level of the PPy chains. In neutral state, the chemical structure of PPy chains is benzoniod-like as shown in Figure 1.[36-37] Since the bandgap is too wide for

electrons in valence band to jump to conduction band at room temperature without any irritation, neutral PPy is as insulator. Upon oxidation, one electron is extracted from a neutral segment of PPy chain. In order to stabilize, structure and electronic rearrangement take place on the polymer backbone and polaron is formed.[36] The presence of the polaron on the chain introduces two localized electronic levels in the band gap. The bonding cation level in the polaron is occupied by an unpaired electron and the polaron has a spin of 1/2. When another electron is removed from the same segment of PPy chain, we have (doubly charged) bipolaron formation. A bipolaron is defined as a pair of delocalized positive charges which extend over about four pyrrole rings(conjugation length) : this separation distance (conjugation length) is dependent on oxidation state. It implies that the energy gained by the distortion into bipolaron structure is larger than the Coulomb repulsion between the two positive charges. The lower energy of bipolaron state is empty, and so the species has a spin of zero. A bipolaron can move along the PPy chain by the rearrangement of double and single bonds in the conjugated system, so the PPy transfer charge in the oxidized state. In the polymer, the pyrrole units have positive charges.
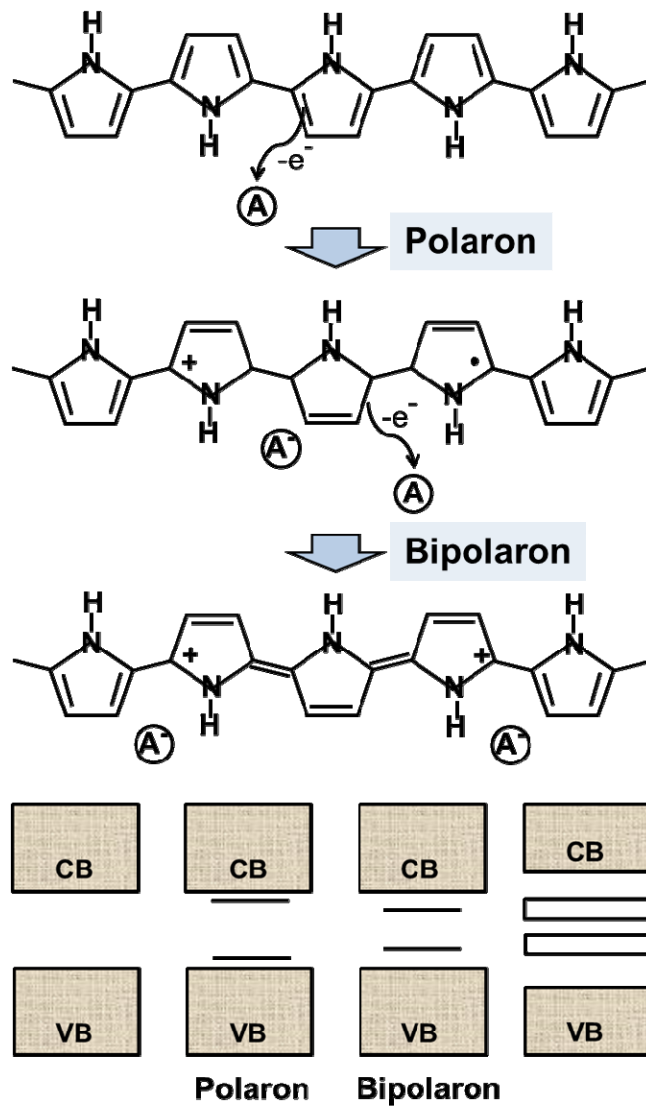
Figure 1. Electronic band model of PPy : Neutral, Polaron, and Bipolaron state.[36]

1.1.2. Fabrication methods of conducting polymer nanomaterials with template

A variety of fabrication methods have been developed for conducting polymer nanomaterials. However, it is still challenging because of their unstable properties including coalescence and Ostwald ripening (Figure 2).[38-51] Among the various synthetic strategies, template method is a very promising and powerful tool to fabricate conducting polymer nanomaterials for overcoming of limitations. Template method involves the inclusion of guests such as inorganic or organic constituents inside the void spaces of a host material. These voids act as the template, deforming the shape, size, and orientation of the compound produced. In general, template method is classified by soft and hard templates. Whereas anodic aluminum oxide (AAO) membrane, track-etched polycarbonate (PC) and zeolite can be used as hard templates, soft templates include surfactant, cyclodextrin, liquid crystal, etc. [52]
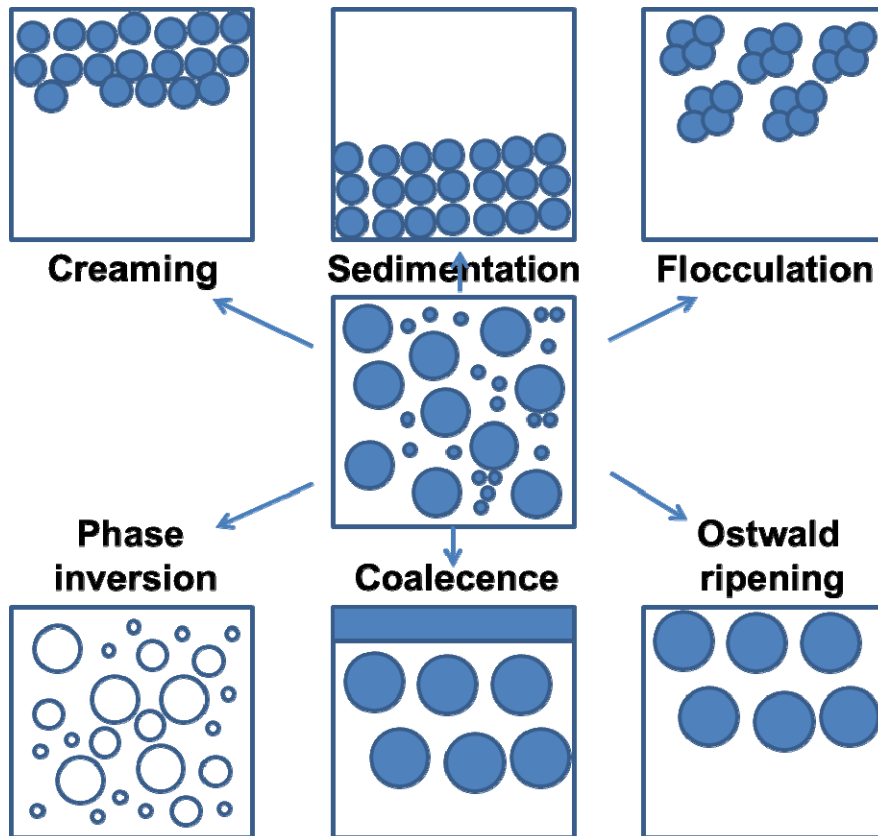
Figure 2. Unstable properties of the materials including coalescence, and Ostwald ripening.[38]

1.1.2.1. Soft template method

Recently, soft template method has been used for the fabrication of various morphologies of polymer nanomaterials. There are several soft templates such as surfactant, liquid crystalline polymer, cyclodextrin, and functionalized polymer.[53-61] Among them, surfactants, which imply cationic, anionic and non-ionic amphiphiles, are mostly used for the for mation of micelle as a nanoreactor.[62-67] Microemulsions are macroscopically homogeneous mixtures of oil, water and surfactant, which on the microscopic level consist of individual domains of oil and water separated by a monolayer of amphiphile. Micelle formations in microemulsion are represented in Scheme 4. Microemulsions should not be regarded as emulsions with very small droplet size; micro- and macroemulsions are fundamentally different. Macroemulsions mean conventional emulsions. Whereas emulsions are inherently unstable systems in which the droplets eventually will undergo coalescence, microemulsions are thermodynamically stable with a very high degree of dynamics with regard to the internal structure. In emulsion, phase separation is rapid unless the system is well mixed. Droplets continuously collide and coalesce, and are broken by the shear exerted on the system. The droplet size is dependent on the system components (oil, stabilizer, phase ratio) and the mixing characteristics. On the other hand, microemulsions are

thermodynamically stable (i.e., indefinitely stable) with droplet sizes varying from 10 to 100 nm. Relatively large quantities of mixed emulsifiers typically consisting of an ionic surfactant (e.g., sodium dodecyl sulfate (SDS)) and a short chain alcohol are usually used to prepare these emulsions.[68] During the polymerization, in a conventional emulsion polymerization, the monomer is located in the following four locations: (1) monomer droplets; (2) inactive monomer swollenmicelles; (3) active micelles that become monomer-swollen polymer particles where the polymerization occurs; (4) solute monomer in an aqueous phase. Two characteristics of oil-in-water microemulsion polymerization are different from those of conventional emulsion polymerization: (1) no monomer droplets and no inactive micelles exist; (2) the system is optically transparent. Microemulsions act as attractive media for polymerization reactions. Microemulsion polymerization is a novel fabrication technique which allows the preparation of ultrafine latex particles within the size range from 10 nm to 100 nm and with narrow size distribution. However, the formulation of microemulsions is subject to severe constraints due to high emulsifier level (over 10 wt%) needed for achieving their thermodynamic stability.[69] Miniemulsion systems are somewhere in between macro- and microsystems. They contain both micelles and monomer droplets, but the monomer droplets are smaller than in macrosystems.[70-73] For both micro-

and minireaction systems in which the initiator is soluble in the continuous phase, the mechanism for polymerization is determined by the relative surface areas of micelles versus monomer droplets. Compared with the miniemulsion (5–10 wt% of surfactant used), high concentration (15–30 wt%) of surfactant forms robust and compact micelle, and the inner space of micelle can be used as a nanoreactor. Besides sphere and layer morphologies, a wide range of morphological spectra could be obtained by carefully controlling the synthetic conditions. In general, microemulsion polymerization has been widely accepted for synthesizing conducting polymer nanoparticle, hollow nanosphere, coreshell nanostructures, and nanofibers.[74-88] Various morphologies of PPy nanomaterials, such as ellipse, hexagon, tetrahedron, rod, needle, and comb shapes were observed in a specific condition. The driving force in determining the morphogenesis is not clear, but it is obvious that the soft templates played an important role in the structural development of PPy nanomaterials. However, it is difficult to control the micelle formation during microemulsion polymerization. In general, polymerization process is kinetically and thermodynamically unstable because of Ostwald ripening, the growth by collision between monomer droplets and monomer consumption during polymerization.[89, 90] It is noteworthy that precise control of the micelle is essential to produce monodisperse and nano-sized conducting polymer

nanomaterials.

1.1.2.2. Hard template method

Hard template method has been used for the 1-D nanostructures such as nanotubes, nanorods and nanofibers of conducting polymers. The commonly used templates are AAO membrane, and track-etched PC membrane, whose pore size ranges from 10 nm to 100 μm. Hard template methods for synthesizing conducting polymer nanomaterials have been extensively reviewed in recent years.[91-94] In general, the polymerization of a conducting monomer has been performed at nanochannel as a nanoreactor and hard templates are removed after polymerization in order to fabricate 1-D conducting polymer nanomaterials. When the pore is filled with appropriate material, it generates a self-assembled nanofiber. The membranes are commercially available in fixed sizes with specific pore diameters, and also prepared in the laboratory using electrochemical means. Desired pore length and diameter can be controlled by synthetic parameters. Martin et al. have used hard template method for preparing polymer nanomaterials.[95-99] Especially, nanotubes and nanofibers composed of conducting polymers were fabricated within the pores of nanoporous membranes. They synthesized the nanotubes with hard templates using chemical oxidation and electrochemical

polymerization. During the polymerization process, the conducting polymer preferentially nucleates and grows on the pore walls of membranes. Resultant polymer tubular structures are tuned by polymerization time. Whereas short polymerization time provides the thin wall of conducting polymer nanotube, long polymerization time produced thick walls. In addition, PPy nanotubes and nanofibers were selectively fabricated depending on the polymerization time. Several researchers also focused on hard template method in order to synthesize various conducting polymer nanomaterials.[100-105] Most template methods can be accomplished by simply immersing the hard template into a monomer/oxidant solution. Recently, Jang et al. produced PPy nanotube and carbon nanotube (CNT) using vapor deposition polymerization (VDP) mediated AAO membrane method.[106]

1.1.3. Vapor deposition polymerization (VDP)

The enhanced stability and tunable surface properties derived from the selective polymer coating of inorganic colloids have expedited the development of a variety of methods to fabricate inorganic-polymer core–shell nanostructures.[107-111] To date, the preparation of polymer-coated inorganic nanoparticles has largely depended upon the solution-based approaches, which include emulsion or dispersion polymerization and adsorption of polymers onto the inorganic particles.[112, 113] However, these methods have often been limited by the large particle–particle aggregations, the formation of the isolated polymer particles from the inorganic colloids, or the requirement for the complicated multistep procedure.

Vapor deposition of inorganic thin films has been extensively applied to the field of semiconductor and coating industries. The deposition process can be classified into physical vapor deposition (PVD) and chemical vapor deposition (CVD). The difference between PVD and CVD is the appearance of chemical reaction during deposition process. In case of CVD, it is the process of chemically reacting a volatile compound of material to be deposited, with other gases, to produce a nonvolatile solid that deposits on a suitably places substrate.

In the case of the formation of thin polymer film, polymerization process is chemical change. Polymer thin film can be obtained by simple deposition, in

which the polymer from the gas phase directly is deposited onto a substrate or vapor deposition polymerization (VDP), in which the first thing is deposition of monomer, pre-polymer and oligomer onto surface, and then polymerization is occurred on the surface by thermal, chemical, photochemical, and other process. VDP can produce uniform, no defect films, so VDP is superior to simple deposition of polymer. And VDP can use monomer as deposition materials, VDP method has more advantages than general CVD method.

VDP approach offers polymer thin film on the desired surface (e.g. the surface of colloidal inorganic particle, film, and other various morphology). And the control of the film thickness and ultra thin film are obtained by VDP method.[114, 115] In the VDP approach, monomer is first absorbed on to the surface to control thickness of monomer in reversible state. Amount of the injected monomer is parameter of polymer film thickness. It can control the thickness of final polymer film in nano-sized and mirco-sized. VDP approach is no solvent process. Since solvent can produce undesirable pinhole defects and cloudiness, desirable quality of film is obtained by VDP approach. Moreover, because solvent is harmful material and waste in environmental concerns, it has many advantages in environmental and healthful concerns. Therefore, it is desirable to develop a simple and reliable method to fabricate inorganic colloid-polymer nanoparticles with the well-defined core–shell

morphology. Vapor deposition techniques can provide the creation of a smoother and more uniform polymer layer by the consecutive polymerization of vaporized monomer under a vacuum onto the desired surface. Especially, conducting polymers can be grown on a nanofiber surface by controlling critical kinetic factors (temperature and pressure) during VDP, leading to the formation of multidimensional polymer nanostructures.

1.1.4. Sensor applications using conducting polymer nanomaterials

Conducting polymers are emerging onto the market with expectations of expansion in the next few years. Of organic materials, only conducting polymers have electrical and optical properties which are similar to those of inorganic semiconductors or sometimes metals. Thus, conducting polymers have been widely used to fabricate versatile chemical and biological sensors. Conducting polymers themselves are very sensitive to their surrounding environments, which makes them suitable for various sensor transducers. In particular, oxidation level of conducting polymers is readily affected by chemical and electrochemical doping/dedoping mechanisms, resulting in a sensitive and rapid response to specific analytes.[9] Most conducting polymer sensors rely on electrochemical detection techniques using amperometric, potentiometric, and conductometric methods. Figure 3 illustrates an electrochemical sensing system based on a conducting-polymer transducer.
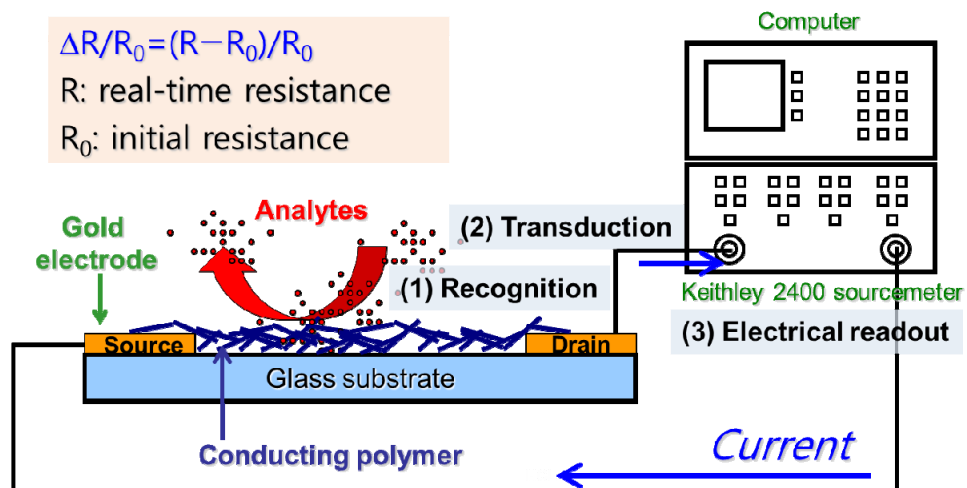
Figure 3. Schematic illustration of an electrochemical sensor consisting of a conducting polymer film, electrodes, and substrate. The electronic components are needed to monitor current flowing through the conducting polymer. The conducting polymer plays the role of transducer. The overall sensing process involves 1) analyte recognition, 2) signal transduction, and 3) electrical readout.[9]

The electrochemical sensor recognizes the phenomenon that the charge transport properties of conducting polymers are changed when exposed to some analytes, and the change can be correlated quantitatively to the concentration of the analytes.[116, 117] The response mechanisms of conducting polymers comprise oxidation/reduction, swelling, conformational changes, charge transfer/screening, and so forth. From the viewpoint of sensor applications, the most distinguishing properties of conducting polymers are as follows: i) conducting polymers can be readily prepared by electrochemical and chemical polymerization; ii) they are highly sensitive to a broad range of analytes at ambient temperature; iii) an amplified response is expected from their inherent transport properties (e.g., electrical conductivity and rate of energy migration); iv) the polymer structure is conveniently modified or functionalized to display selective responses toward specific analytes; v) the sensitivity is readily tunable by adjusting the synthetic variables such as incorporated counter ions and polymerization temperature; vi) a sensor array can be fabricated through electrochemical deposition or solution casting, which allows miniaturization and mass production of sensor devices. These features make it highly attractive to use conducting polymers for sensor applications. [18, 118-125] However, the sensitivity and selectivity of conducting polymer-based sensors still leave room for improvement. More specifically, there are

19

several important factors which need to be improved for further success of conducting polymer-based sensors; sensitivity, selectivity, surface area, environmental stability and surface properties.[126-133] Therefore, Conducting polymer materials of nanometer sizes have emerged as promising candidates for high-performance transducer applications with unique properties depending on the size and shape.[50, 134-146] In terms of sensor applications, moreover, they have beneficial advantages such as high surface area and small dimensions.[147, 148] The enlarged surface area enhances the interactions between the materials and analytes, which leads to high sensitivity, and the small dimensions facilitate adsorption/desorption kinetics for analytes in the materials, which allows a rapid response time and high signal reproducibility even at room temperature.[149-158] In addition, they can present increased signal intensity through variation of charge transport behavior in the bulk of the materials, not only in the surface region.

1.2. Objectives and Outline of the Study

1.2.1. Objectives

In the preceding section, the importance of conducting polymer nanomaterials was introduced from the viewpoint of academic research and practical sensor applications. The aim of this dissertation is to describe the fabrication of conducting polymer nanomaterials by vapor deposition polymerization (VDP) method. Furthermore, their applicable fields are also explored, including various sensors.

1.2.2. Outline

This dissertation involves the following subtopics:

I. Ultrasensitive chemical nerve agent sensing using multidimensional Poly(3,4-ethylenedioxythiophene) (PEDOT) nanotubes

  1. Fabrication of multidimensional nanostructures with PEDOT on the electrospun template by vapor deposition polymerization

  2. Control of surface morphology under different synthetic conditions

  3. Chemical nerve agent sensor using multidimensional PEDOT nanotubes functionalized with hydroxyl group

II. High-performance FET-type dopamine biosensor using multidimensional carboxylated PEDOT (CPEDOT) conjugated with dopamine receptor

nanoplatform

1. Fabrication of multidimensional nanostructure based on the CPEDOT

2. Construction of dopamine sensor based on dopamine receptor-conjugated multidimensional CPEDOT nanobiohybrids

3. Real-time responses of dopamine sensor

III. Fabrication of Ag NPs/CPEDOT nanohybrids for H_2O_2 sensor

1. Preparation of Ag NPs /CPEDOT nanohybrids using AAO template *via* one-pot synthesis

2. Sensing behaviors of Ag NPs /CPEDOT NTs with various $AgNO_3$ concentrations for H_2O_2 detection

IV. Highly sensitive and selective chemiresistive sensor based on multidimensional polypyrrole (MPPy) nanotubes

1. Fabrication of the MPPy nanotubes

2. Real-time responses of chemiresistive sensor based on MPPy nanotubes for volatile organic compounds (VOCs) and toxic gases detection

3. The selectivity test for the several representative VOCs and toxic gases frequently present in human breath

V. Hydrogen gas sensor based on ultra-thin carboxylated polypyrrole (CPPy) layer-coated CNT nanohybrids

1. Fabrication of ultra-thin skin coating with carboxylated polypyrrole

(CPPy) on the CNT and modification with Pd NPs

2. High performance H_2 sensor based on the Pd NPs/CPPy/CNT

2. EXPERIMENTAL DETAILS

2.1. Poly(3,4-ethylenedioxythiophene) (PEDOT)

2.1.1. Fabrication of Multidimensional Nanostructures based on Hydroxylated PEDOT Nanotube (HPNT)

2.1.1.1. Preparation of Poly(methyl methacrylate) (PMMA) nanofibers as template by electrospinning process

Poly(methyl methacrylate) (PMMA) has polar groups that can interact with metal cations and is also soluble in various organic solvents. Thus, PMMA (1 g, Mw = 350,000, Aldrich) was dissolved in dimethyl formamide (DMF) at 70−80 °C, and PMMA nanofibers were electrospun from the PMMA/DMF solution. In the electrospinning process, the solution was injected through a stainless steel needle (22 gauge) that was connected to a high-voltage dc power supply (Nano NC 60 kV/2 mA). The solution was continuously fed through the nozzle connected with syringe pump (Kd scientific) at a rate of 12 μm min^{-1}. High voltage (15 kV) was applied between the needle and the grounded collector (the distance was 15 cm). As a result, PMMA nanofibers were continuously ejected from the nozzle and accumulated on a cellulose substrate. The thickness of the nanofiber network film was controlled by adjusting the accumulation time. To gain highly aligned nanofiber arrays, magnetic field-assisted electrospinning technique was employed, where two magnets (50

000−80000 G) were placed in parallel on the collector. They were connected to the ground terminal of the power supply.

2.1.1.2. Growth of multidimensional nanostructures based on HPNT on the template by Vapor Deposition Polymerization (VDP) method

The resulting PMMA nanofibers were immersed into ferric chloride (FeCl$_3$, Aldrich)/methanol solution, as an initiator (40mL). After drying under vacuum, the nanofibers were placed in the pressure-controllable reactor. Then, the liquid monomer (EDOT or EDOT/hydroxymethyl EDOT ([EDOT]/[HEDOT] = 3.6/1) mixture, Aldrich) was injected.

2.1.1.3. Design of surface morphology under controlled synthetic conditions

It was performed at a controlled reactor pressure and temperature, which resulted in the multidimensional formation of HPEDOT-coated PMMA nanofibers with nanonodules (NNs, 90 °C and 760 Torr) and nanorods (NRs, 60 °C and 760 Torr) surfaces after 4 h. The nanofiber with smooth layer (SL, 90 °C and 1 Torr) surface was also prepared. Furthermore, the population of the NN and NR substructures increased with increasing initiator concentration (2−10 wt % of FeCl$_3$/methanol solution).

2.1.1.4. Removal PMMA nanofibers template

The hydroxylated PEDOT nanotubular structures were obtained by dissolving the PMMA core with DMF solution. The final products were washed by suction filtration of water and methanol to remove residual reagents.

2.1.1.5. Characterization of multidimensional nanostructures based on the hydroxylated PEDOT

Fabricated multidimensional nanostructures based on the Poly(3,4-ethylenedioxythiophene) were characterized by transmission electron microscope (TEM) obtained from a JEOL JEM−200CX. It was imaged with a high−resolution transmission electron microscopy (HR−TEM) from a JEOL JEM−3010. The surface morphology of the sample was observed using a field−emission scanning electron microscope (FE−SEM, JEOL JSM−6700F) and X−ray Photoelectron Spectra (XPS) were recorded on a LabRAM HR (Sci−Thch instrument Co. Ltd) with 1064 nm laser excitation and an AXIS−His (KRATOS), respectively.

2.1.1.6. Instruments for the sensor

The electrical measurements of sensing devices based on the PEDOT nanotubes with various morphology were conducted with a Keithley 2400-

sourcemeter and a Wonatech WBCS 3000 potentiostat. Various analytes were introduced by mass flow controllers (MFC, SEC 4400 form KNH, Dwyer Instrument, Inc.). The efficiently home-made sensor device contained with conductive wires was mounted in a testing chamber with gas inlet/outlet lines connected with MFC and an electrical feed-through. The resistance change was monitored in real-time at an applied current of 10^{-6} A. The instruments were connected via a GPIB interface to a computer and controlled through Labview software. The sensitivity was calculated by measuring the normalized electrical resistance change $\Delta R/R_0 = (R - R_0)/R_0$, where R_0 and R are the measured real-time resistance and initial resistive value, respectively. In addition, the response time was defined as the time required for the conductance to reach 90 % of the equilibrium value after a test gas was injected, and recovery time was the time necessary for a sensor to attain a conductance 10 % above its original value in air.

2.1.2. Fabrication of Dopamine Receptor-Conjugated Multidimensional Carboxylated PEDOT (MCPEDOT) Nanobiohybrids

2.1.2.1. Preparation of multidimensional nanostructure based on the CPEDOT

Electrospun PMMA NFs as template were prepared by methods in 2.1.1.1.

27

part. The resulting PMMA NFs were immersed into ferric chloride/methanol solution (40 mL). After drying under vacuum, the NFs were placed in the glass container. Then, the mixture of 3,4-ethylenedioxythiophene (EDOT) monomer (Aldrich) and carboxylated EDOT (CEDOT) monomer (Aldrich) was also placed in the glass container at a controlled temperature (60 ℃), which resulted in the formation of multidimensional CPEDOT-coated PMMA NFs. The multidimensonal CPEDOT nanotubular (MCPEDOT NTs) structures were obtained by dissolving the PMMA core with DMF solution. The final products were washed by suction filtration of water and methanol to remove residual reagents. The four-probe conductivities of the nanostructures were 2×10^0 to 6×10^1 S cm^{-1}.

2.1.2.2. Fabrication of flexible MCPEDOT NT electrodes

To transfer the MCPEDOT NTs on the electrode-deposited flexible substrate, the MCPEDOT/PMMA NFs was dipped into the DMF solution. Also, the core, PMMA NFs, was dissolved in the DMF solution. Finally, flexible MCPEDOT NT electrodes were constructed after several washing process.

2.1.2.3. Formation of dopamine receptor-conjugated MCPEDOT nanobiohybrids

MCPEDOT NTs were conjugated with dopamine receptors for the liquid-ion-gated Field Effect Transistor (FET)-type dopamine sensor platform. Coupling reaction was then carried out by exposing the modified substrate to a mixed solution of dopamine receptor and 1 wt % aqueous 4-(4,6-Dimethoxy-1,3,5-triazin-2-yl)-4-methyl-morpholinium chloride (DMT-MM, 10 μL) over 12 h to attach the dopamine receptor on the surface of the MCPEDOT NTs. The substrate was then rinsed with distilled water and dried in a stream of nitrogen gas.

2.1.3. Fabrication of Multidimensional Ag NPs/CPEDOT nanohybrids

2.1.3.1. Materials

The anodic aluminum oxide (AAO) membrane with an average pore diameter of *ca*. 100 nm and thickness of 60 μm was purchased from Whatman. Co. 3,4-ethylenedioxythiophene carboxylic acid and $AgNO_3$, were purchased from Sigma-Aldrich, Co. (USA) and used as received without further purification.

2.1.3.2. Preparation of multidimensional Ag NPs /CPEDOT nanohybrids *via* one-pot synthesis

Ag cations were adsorbed onto an AAO membrane by immersing the membrane with various AgNO$_3$ concentration for 5 min and then drying it in a vacuum oven for 3 h. In order to eliminate residual Fe/Ag cations and prevent the possible interconnecting or closing of the nanotubular edges, disposable sorbents were used. The Ag cations-adsorbed AAO template and EDOT-carboxylic acid were placed into a reactor which was evacuated at 10^{-2} Torr for 20 min. Subsequently, VDP had been performed at 150 ^{o}C for 1 h. The AAO membrane was removed by treatment with HCl solution at room temperature for 5 h. Finally, the dark blue product was obtained and washed with ethanol to remove residual monomers and initiators.

2.2. Polypyrrole (PPy)

2.2.1. Multidimensional Polypyrrole Nanotubes (MPPy NTs)

2.2.1.1. Materials

Pyrrole (98%), FeCl$_3$, and poly(vinyl alcohol) (PVA; Mw 9000~10,000) were purchased from Aldrich. Poly(dimethylsiloxane) (PDMS) substrate was provided from DOW CORNING Co. (product: SYLGARD 184 SILICONE ELASTOMER KIT).

2.2.1.2. Preparation of the electrospun nanofiber as template

6 wt% PVA solution was prepared at 80 ℃ and PVA nanofibers with an average diameter of 70 nm were electrospun from the PVA solution (Nano NC 120 kV / 1.5 mA). The distance between syringe needle to a cellulose substrate (collector) was *ca.* 10 cm.

2.2.1.3. Growth of Polypyrrole on the template by VDP

The resulting PVA nanofibers were immersed into 5 wt% ferric chloride /ethanol solution, as an initiator (40 mL). After drying under vacuum for 5 h, the nanofiber were placed in the pressure-controllable reactor. Subsequently, the liquid monomer (pyrrole) was injected at a controlled temperature and pressure, which resulted in the multidimensional formation of polypyrrole coated PVA nanofibers with nanonodules (NDs, 60 ^{o}C and 760 torr for 10 min) and nanowires (NWs, 40 ^{o}C and 760 torr for 10 min) surfaces. The nanofiber with smooth layer (SM, 60 ^{o}C and 1 torr for 10 min) surface was also prepared as control experimental data. Finally, the MPPy NT structures with NDs and NWs surfaces were obtained by dissolving the PVA core with distilled water.

2.2.1.4. Characterization of MPPy NTs

All electrical measurements were conducted with a Keithley 2612A source meter and probe-station (MS TECH, MODEL 4000). The MPNS device was

mounted in a test chamber on the probe-station and the probes were contacted on the microelectrodes. The test chamber were connected with gas inlet/outlet lines connected with MFC and an electrical feed-through. The resistance change was monitored in real-time at an applied current of 10^{-6} A. The instruments were connected via a GPIB interface to a computer and controlled through Labview software.

2.2.2. Fabrication of Multidimensional CPPy/CNT Nanohybrids Decorated with Pd NPs (Pd/CPPy/CNT)

2.2.2.1. Materials

The CNTs were supplied from Prof. S.-H. Yoon. 1-Pyrenecarboxylic acid (PCA), $FeCl_3$, $PdCl_2$, pyrrole monomer, and pyrrole-3-carboxylicacid (P3CA) were purchased from Aldrich).

2.2.2.2. Ultrathin skin coating with carboxylated polypyrrole (CPPy) on the CNT

Pristine CNTs were pretreated with 1-Pyrenecarboxylic acid (PCA) in a water/ethanol mixture solution for 24 h. The surface-modified CNTs were obtained by centrifugal precipitation and dried in a vacuum oven at 25 °C.Next, 0.2 g of PCA-modified CNTs and 0.02 g of $FeCl_3$, as an oxidant initiator, were

placed into the reactor, which was then evacuated to *ca.* 10^{-1} Torr at 25 °C. Under the vacuum conditions, a mixture (0.05 mL) of pyrrole monomer and pyrrole-3-carboxylic acid (P3CA) was injected into the reactor and completely vaporized at 80 °C.

2.2.2.3. Modification of CPPy/CNT surface with Pd NPs

A sonochemical reduction method was introduced to attach Pd NPs on the smooth CPPy–CNT surface. When propan-2-ol was added into the Pd^{2+} solution, the rate of reduction was enhanced.

2.2.2.4. Formation of Pd/CPPy/CNT with different Pd NPs contents as adjusting amounts of functionalized monomer

Three types of ultrathin CPPy skins were constructed to control the amount of Pd NPs (the Pd NPs–CPPy–CNTnanohybrids : PCCN); the P3CA to pyrrole molar ratios 1 : 15 (PCCN1), 1 : 30 (PCCN2), and 1 : 60 (PCCN3). The vaporized monomer was physically adsorbed on the surface of the carboxylic group-modified CNTs, and then the polymerization process was carried out for 24 h.

33

3. RESULTS AND DISCUSSION

3.1. Ultrasensitive Chemical Nerve Agent Sensing Using Multidimensional Poly(3,4-ethylenedioxythiophene) (PEDOT) Nanotubes.

3.1.1. Fabrication of multidimensional nanostructures with PEDOT on the electrospun template by vapor deposition polymerization (VDP).

We created a new synthetic process that allows tailoring the surface morphology of 1D conducting polymer nanomaterials. Novel nanonodule (NN) and nanorod (NR) substructures were grown on the surface of electrospun polymer nanofiber substrate by controlling pressure and temperature. The kinetic model developed showed that slower polymerization kinetics were favorable to the growth of the unique substructures on the nanofiber surface. Several other potentially critical variables remain, which can affect the formation of the surface nanostructures, such as the reactivity of monomer and the interfacial tensions of monomer and substrate. Thus, there is an ongoing effort to develop a more generalized kinetic model.

Figure 4 shows that PMMA nanofibers as template were accumulated on the collector by electrospinning, in which PMMA solution was supplied to the syringe tip at 5 μm min^{-1} and an electric field of 15 kV was applied between

the tip and the grounded collector (distance, 15 cm). Figure 5 shows the synthetic procedure for multidimensional nanofibers and nanotubes under three representative vapor deposition polymerization (VDP) conditions. Polymer nanofibers were fabricated by electrospinning,[166-169] and then conducting polymer was introduced onto the nanofiber surface through VDP.[170-172] During this process, the electrospun nanofibers serve as both template and substrate for the growth or assembly of nanobuilding blocks (from oligomer to polymer). More specifically, PMMA nanofibers were accumulated on electrically conductive collectors by electrospinning (Figure 6a). The nanofibers were immersed in ferric chloride solution, leading to the adsorption of ferric ions on the PMMA nanofiber surface (Figure 6b). Because ferric ions are a potent Lewis acid, they form a chelate complex with lone electron pairs on the PMMA chains by coordination bonding. Subsequently, liquid monomers were vaporized at controlled pressures, and their chemical polymerization proceeded on the nanofiber surface with the adsorbed ferric ions, which resulted in the formation of a polymer sheath on the PMMA nanofiber. The core nanofiber was then removed by solvent etching, yielding a nanotubular structure. Conducting polymers such as PEDOT generally have strong interchain interaction, and PMMA dissolves well in DMF. Thus, the core nanofiber was readily etched without structural deformation of PEDOT shell.

Electron microscopic analyses revealed that PEDOT layers with an average thickness of 20 nm were coated onto the PMMA nanofibers with an average diameter of 60 nm and the nanotubular structures were obtained successfully with no deformation after the etching process. Surprisingly, as shown in Figure 6e−h, the resulting nanotubes exposed unique surface substructures, such as nanoscale rods (NR, Figure 6e,f) and nodules (NN, Figure 6g,h), in addition to the smooth layer (SL, Figure 6c,d). Thus, key synthetic variables were further examined to determine how such morphologies were formed.
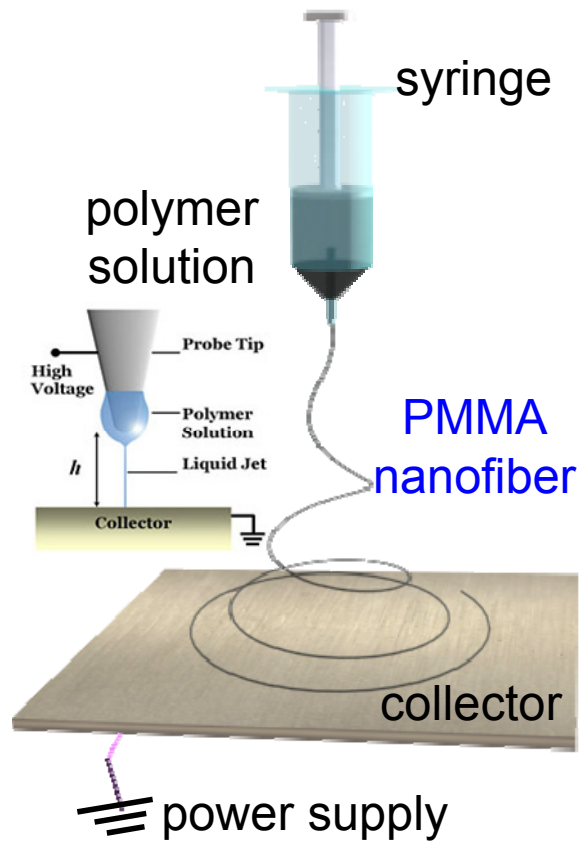
Figure 4. PMMA nanofibers were accumulated on the collector by electrospinning, in which PMMA solution was supplied to the syringe tip at 5 μm min^{-1} and an electric field of 15 kV was applied between the tip and the grounded collector (distance, 15 cm).
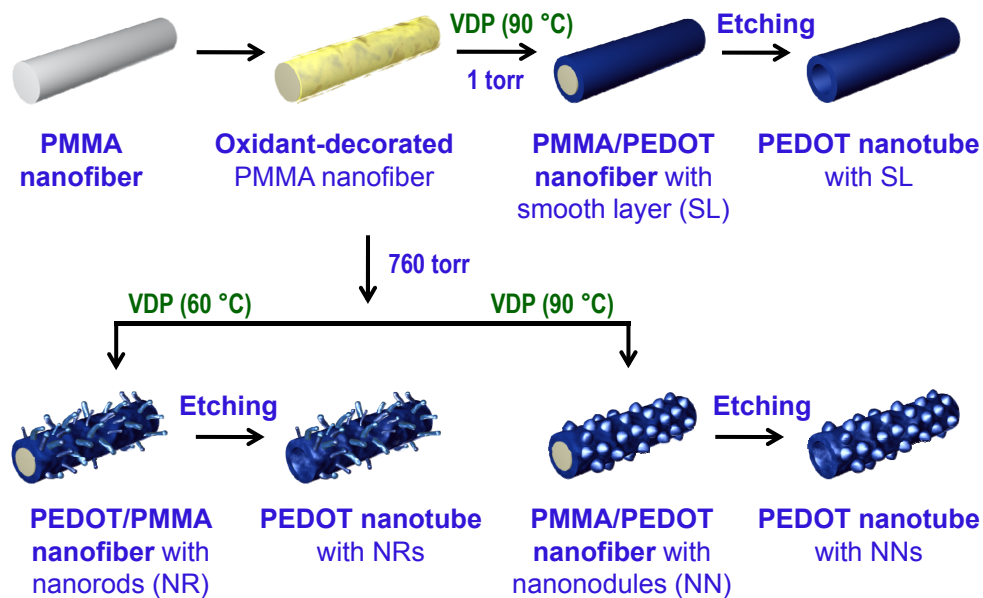
Figure 5. Schematic illustration of the synthetic routes to multidimensional PEDOT nanostructures. The PMMA nanofibers function as template as well as substrate for the growth of PEDOT under different synthetic conditions (temperature and pressure).
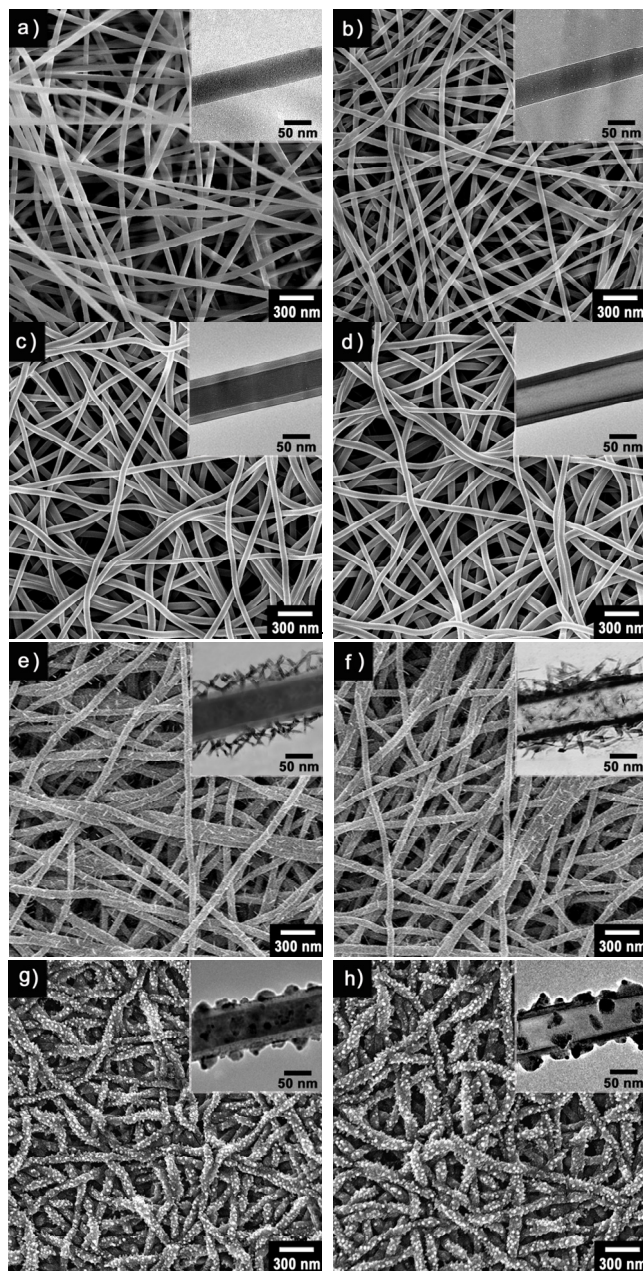
Figure 6. The morphologies of the resulting nanomaterials were characterized by FE-SEM and TEM (right top inset images): PMMA nanofibers (a) before and (b) after ferric ion adsorption; PMMA/PEDOT nanofibers with SL surface

(c) before and (d) after core etching; PMMA/PEDOT nanofibers with NR surface (e) before and (f) after core etching; PMMA/PEDOT nanofibers with NN surface (g) before and (h) after core etching. The SEM and TEM images show the unique surface substructures. Additionally, the TEM images reveal the hollow interior of the nanotubular structures.

The successful fabrication of the pristine PMMA, PMMA/PEDOT was confirmed by FT-IR spectroscopy (Figure 7). The bands at 1730 cm^{-1} and 2995 cm^{-1} are designated to the C=O stretch and CH$_3$ (or CH$_2$) stretch of PMMA nanofibers, respectively.[173] In the case of PMMA/PEDOT nanofibers, the peaks at 942 cm^{-1}, 1083 cm^{-1}, and 1384 cm^{-1} are assigned to symmetric C=C, C-S and C-O stretching vibration of PEDOT and the peaks at the C=O and CH$_3$ stretch bonds of PMMA are also observed at 1730 cm^{-1} and 2995 cm^{-1} peaks.
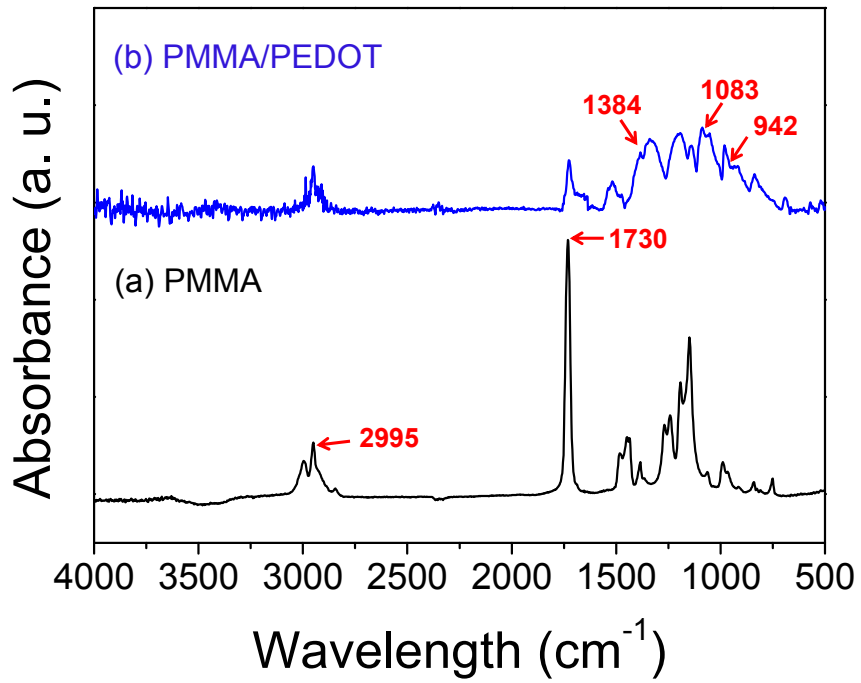
Figure 7. FT-IR spectra of (a) PMMA and (b) PMMA/PEDOT nanofibers.

3.1.2. Kinetically investigation of multidimensional PEDOT nanostructures.

Generally, the deposition of polymers in forming thin films is guided by a nucleation−growth mechanism. Specifically, the deposited nuclei grow on a substrate during polymerization until they become a polymer layer. During this process, kinetic and thermodynamic factors determine the morphology of the polymer layer deposited. Judging from our findings, oligomeric chain fragments consisting of EDOT rings are generated in the initial stage, the subsequent growth of which is highly dependent on synthetic conditions and substrate curvature. Because of the high curvature of the nanofiber, it is difficult to form a smooth polymer layer that completely covers the nanofiber surface via continuous chain growth. Thus, spontaneous assembling of EDOT oligomers could result in vertical growth rather than lateral growth on the nanofiber surface even though the interfacial tension between the EDOT oligomer and the PMMA is low. Under the same conditions, a control experiment was carried out using a flat PMMA film to demonstrate the effect of substrate curvature on the growth process of the polymer (Figures 8 and 9). Although the polymer layer deposited on the flat surface was somewhat rugged, no remarkable features were observed, confirming the dependence of the chain growth on substrate curvature. On the other hand, the formation of the smooth layer on the nanofiber substrate was achieved under synthetic conditions that

provided faster kinetics. The deposition of monomer vapor is enhanced by lowering the pressure and raising the temperature inside the reactor, which, in turn, leads to a rapid polymerization rate on the nanofiber surface. Such kinetic conditions are considered to create a local microenvironment capable of overcoming the geometric effect of the substrate.

	Pristine PMMA	PMMA / FeCl$_3$	PMMA / PEDOT	
760 torr				VDP at 90 ℃
1 torr				VDP at 90 ℃
				VDP at 60 ℃
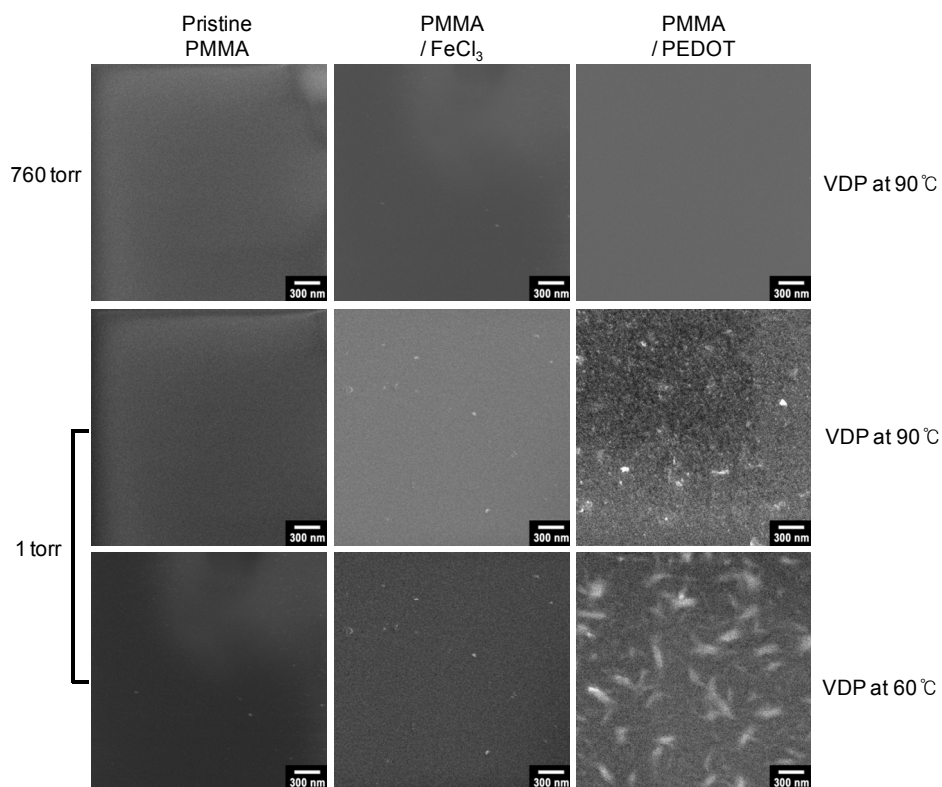
Figure 8. SEM images of the control samples deposited on PMMA film. Effect of substrate curvature on the growth of the polymer (I).

VDP condition

760 torr, 90°C

PEDOT

PMMA

Si wafer

1 µm

1 torr, 90°C

PEDOT

PMMA

Si wafer

1 µm

1 torr, 60°C

PEDOT

PMMA

Si wafer

1 µm
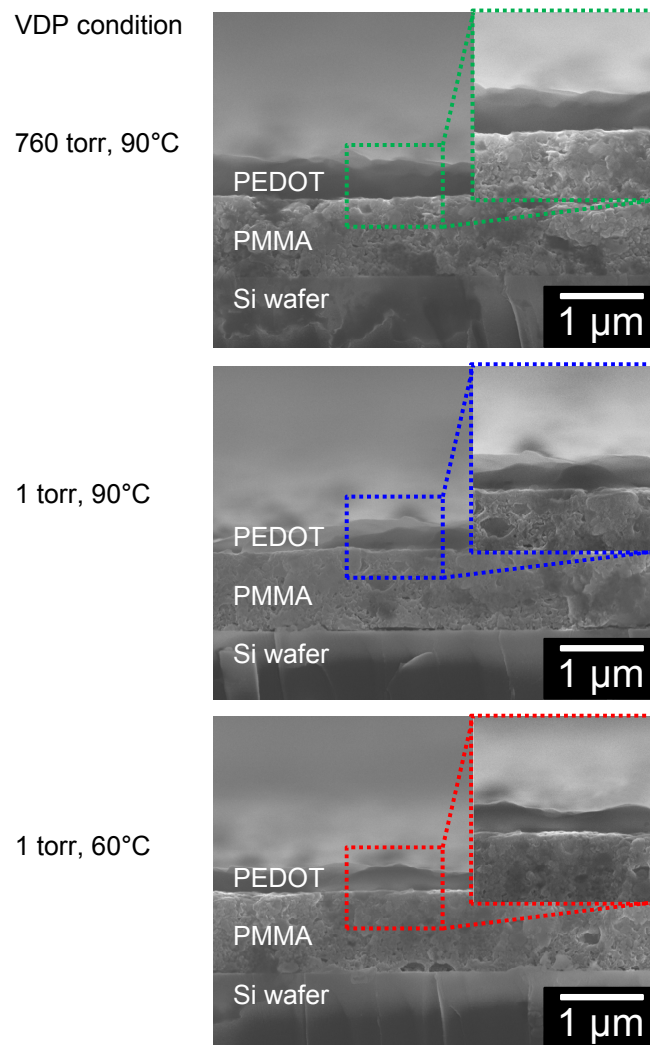
Figure 9. Effect of substrate curvature on the growth of the polymer (II). Cross-sectional SEM images of the control samples deposited on PMMA/silicon wafer.

In fact, there are only a few reports in the literature on the kinetics of chemical polymerization of conducting polymers, mostly due to their insolubility in common solvents. Moreover, it is difficult to experimentally observe kinetic behavior during the VDP process that is carried out in a closed chamber with a controlled internal pressure. In this work, therefore, real-time measuring of the current flowing through the nanofiber substrate was attempted to monitor polymer formation during VDP, and a simple kinetic model was developed to estimate the polymerization rate therefrom. In the VDP process, monomer from the gas phase condenses on the substrate and is oxidized by the redox initiator, the adsorbed ferric ions. EDOT polymerization is believed to occur through monomer oxidation and the creation of radical cations, followed by a coupling reaction. The coupling reaction cyclically proceeds with the oxidation reaction, yielding a polymer when EDOT rings are close enough to react. Monomer disappears via the oxidation reaction, followed by the coupling reaction; the polymerization reaction continues as long as monomer and initiator are available. The rate of oxidation or coupling reaction is the sum of numerous individual oxidation and coupling steps.[174] However, if the rates of oxidation (R_1) and coupling (R_2) reactions are independent of the length of the chain, then the rate of monomer depletion, which is synonymous with the rate of polymerization, can be written in the generic form:

$$\frac{-d[M]}{dt} = R_1 + R_2 = k_1[M][I] + k_2[M*]^2 \qquad \text{(Eq. 1)}$$

where I, M, and M * represent the redox initiator, the monomer, and the oxidized monomer, respectively. Considering that the monomer is stoichiometrically oxidized by the initiator of the polymerization, the integration of the above equation yields:

The above equation was made with the following assumptions

(i) Side reactions are negligible and thus the concentrations of the monomer and the initiator are stoichiometric.

(ii) An average of two electrons per monomer is withdrawn to yield the final polymer.

(iii) The reactivity of the initiator is the same irrespective of the size of the molecule.

(iv) The reactivity of a radical cation is independent of the length of the chain to which it is generated.

The total radical cation concentration is approximately constant through the main part of the polymerization because the rate at which radical cations are formed by initiation is approximately the same as the rate at which they are consumed by propagation. Accordingly, the steady-state approximation can be

made that the rate of change of the concentration of radical cations rapidly becomes and remains zero during the course of the polymerization. Therefore,

$$\frac{d[M*]}{dt} = k_1[M][I] - k_2[M*]^2 = 0 \qquad \text{(Eq. 2)}$$

Namely,

$$k_1[M][I] = k_2[M*]^2 \qquad \text{(Eq. 3)}$$

Consequently, the Eq. 2 is written as

$$\frac{-d[M]}{dt} = 2k_1[M][I] \qquad \text{(Eq. 4)}$$

Prior to solving the kinetic equation, the second assumption is derived from the following reaction stoichiometry:

$$n\ \text{EDOT} + 2n\ \text{FeCl}_3 \rightarrow (\text{EDOT})_n + 2n\ \text{FeCl}_4^- \qquad \text{(Eq. 5)}$$

where one mole of monomer is consumed by two moles of initiator. Based on mass balance calculations, the following equations are obtained:

$$[I]_0 - [I] = 2([M]_0 - [M]) \qquad \text{(Eq. 6)}$$

$$[I] = [I]_0 - 2([M]_0 - [M]) \qquad \text{(Eq. 7)}$$

where $[I]_0$ is the initial initiator concentration. Substituting the above equation into Eq. 4 gives

$$\frac{-d[M]}{dt} = 2k_1[M]\{[I]_0 - 2([M]_0 - [M])\} \qquad \text{(Eq. 8)}$$

Extracting [M] from Eq. 8 yields

$$\frac{d[M]}{4k_1[M]\{[M] - [M]_0 + 0.5[I]_0\}} = -dt \qquad \text{(Eq. 9)}$$

Letting

$$\alpha' = [M]_0 - 0.5[I]_0 \qquad \text{(Eq. 10)}$$

and substituting α into Eq. 9 gives

$$\frac{d[M]}{[M]([M] - \alpha')} = -4k_1 dt \qquad \text{(Eq. 11)}$$

The term on the left-hand side can be separated into two independent terms:

$$\left\{\frac{-1}{\alpha'[M]} + \frac{1}{\alpha'([M] - \alpha')}\right\} d[M] = -4k_1 dt \qquad \text{(Eq. 12)}$$

Integrating both sides with initial conditions, at t = 0, [I] = [I]_0 and [M] = [M]_0, the above equation becomes

$$\frac{1}{\alpha'}\log\frac{[M]_0}{[M]} + \frac{1}{\alpha'}\log\frac{[M] - \alpha'}{[M]_0 - \alpha'} = -4k_1 t \qquad \text{(Eq. 13)}$$

Rearranging

$$\log\frac{[M]_0([M] - \alpha')}{[M]([M]_0 - \alpha')} = -4\alpha' k_1 t \qquad \text{(Eq. 14)}$$

and Letting

$$\beta = \frac{[M]_0 - \alpha'}{[M]_0} = \frac{0.5[I]_0}{[M]_0} \qquad \alpha = \frac{\alpha'}{[M]_0}$$

50

yields finally the following equation

$$\frac{[M(t)]}{[M]_0} = \frac{\alpha}{1 - \beta e^{-4\alpha k_1 t}}$$

(Eq. 15)

Where

$$\alpha = \frac{[M]_0 - 0.5[I]_0}{[M]_0} \qquad \qquad \beta = \frac{0.5[I]_0}{[M]_0}$$

The terms α and β are constants, and thus, it is possible to estimate the concentration of the monomer as a function of time.

Figure 10a shows the real-time current changes in the nanofiber substrates during polymerization. The y-axis showing the change in current was normalized between [0,1] and the curve was fitted (lines) for the experimental data (symbols). A VDP chamber with an electrical feed-through was designed and used for the above measurements. There was no current flow until late in the middle period of the VDP, as expected, and the current began to flow at significantly higher conversions. The polymerization reaction starts with the injection of the monomer and the degree of polymerization increases slowly with time. Therefore, the change in current can be correlated with the rate of polymerization. The time at which more than 90% of the monomer was consumed was determined from the curve and the rate constant can be calculated from Eq. 2. The rate constants were 0.9×10^{-4}, 1.1×10^{-5}, and 5.7×10^{-6} $M^{-1}s^{-1}$ for the surface substructure SL, NN, and NR, respectively. Figure 10b displays the conversion profile for the polymerization of each substructure, calculated as a function of time. The molar concentration ratios of initiator to monomer, [I]/[M], were 2.2, 6.7, and 10.0 for the substructure SL, NN, and NR, respectively. Additionally, the time at which the change in resistance was saturated in the curves in part as the polymerization time required for 90% conversion. These predictions support the hypothesis that the morphology of the polymer deposited on a nanofiber strongly depends on the reaction kinetics.

Besides parameters such as temperature and pressure, the effects of initiator and monomer concentration were also examined. At the corresponding ranges, the calculated rate constants appeared to decrease with increasing molar concentration ratio of initiator to monomer (Figure 10c).
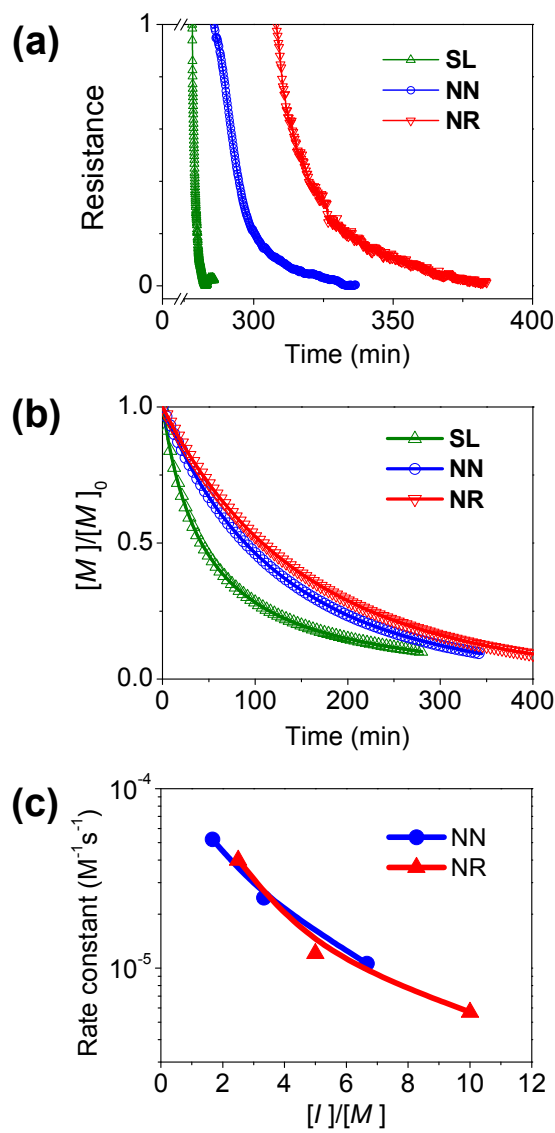
Figure 10. (a) Real-time changes in the resistance of nanofiber network films during VDP for PEDOT coating, (b) Calculated conversion curves for generating unique PEDOT surface substructures (c) Rate constants calculated for different [I]/[M].

3.1.3. Control of surface morphology under different synthetic conditions.

The faster rate constants at lower concentration ratios are unfavorable to the formation of the unique surface substructures. Figure 11 shows the electron microscopic images of PEDOT/PMMA nanofibers prepared with the different concentration ratios of initiator to monomer. With decreasing concentration ratios, the population of unique substructures decreased considerably and their morphology also became somewhat different. Although some of the surface substructures survived, this change was probably due to inhomogeneous deposition of the initiator on the nanofibers surface.
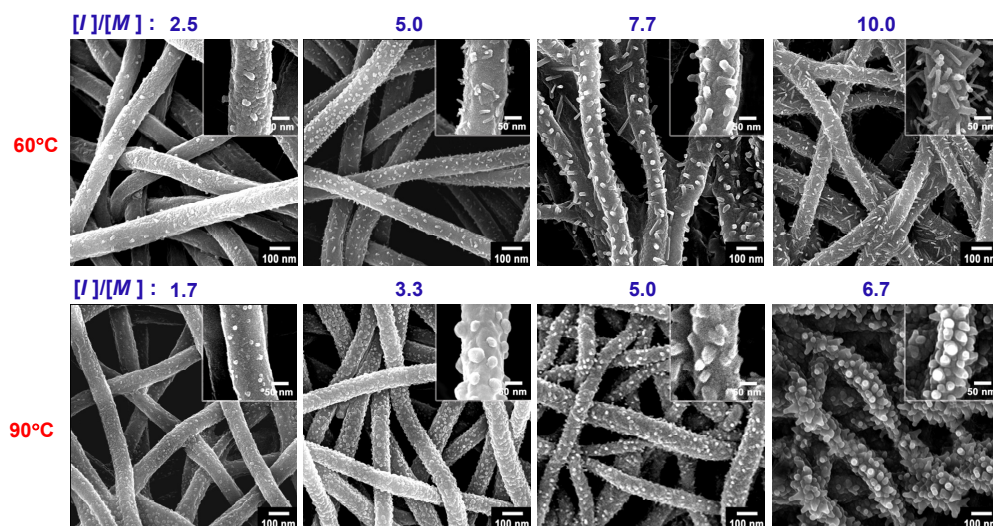
Figure 11. Effect of polymerization kinetics on the surface morphology of multidimensional PEDOT nanostructures. FE-SEM images of PMMA/PEDOT nanofibers obtained with different [I]/[M] and temperatures (insets: high-magnification images): the temperature increased from top line (60 °C) to bottom line (90 °C), and the [I]/[M] increased from the left to the right.

3.1.4. Functionalization of multidimensional nanotubes with hydroxyl group in PEDOT for chemical nerve agent sensor.

The nanotubes were inherently functionalized by introducing hydroxylated EDOT (HEDOT) as a comonomer during the polymerization ([EDOT]/[HEDOT] = 3.6/1) (Figure 12). The role of the hydroxyl group is to act as a reactive unit toward organophosphates of the nerve agents. The successful fabrication of the pristine PMMA/PEDOT, PMMA/HPEDOT nanofibers, and HPNT was confirmed by FT-IR spectroscopy (Figure 12). The bands at 1730 and 2995 cm^{-1} are designated to the C=O stretch and CH_3 (or CH_2) stretch of PMMA nanofibers, respectively. In the case of PMMA/PEDOT nanofibers, the peaks at 942, 1083, and 1384 cm^{-1} are assigned to symmetric C=C, C-S and C-O stretching vibration of PEDOT and the peaks at the C=O and CH_3 stretch bonds of PMMA are also observed at 1730 and 2995 cm^{-1} peaks. In addition, the broad band at 3400 cm^{-1} indicates the –OH of HPEDOT. In the HPNT, after removing the PMMA, there are no peaks at 1730 and 2995 cm^{-1}. These results mean that the PMMA nanofibers are successfully removed and the hydroxyl groups as reactive unit toward organophosphates exist.
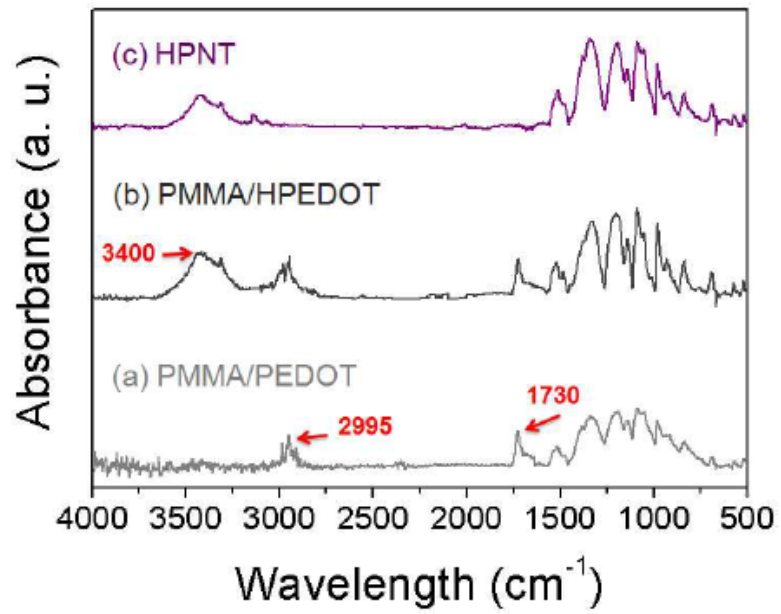
Figure 12. FT-IR spectra of (a) PMMA/PEDOT, (b) PMMA/HPEDOT nanofibers, and (c) HPNT

3.1.5. Chemical nerve agent sensor using multidimensional hydroxylated PEDOT nanotubes (HPNTs).

The fabricated multidimensional hydroxylated PEDOT nanotubes (HPNTs) on the sensor substrate rapidly detected DMMP gas at room temperature. The nanostructures above the surface of conducting polymer can have a high surface area and excellent charge-transport properties by virtue of their unique morphology and anisotropic geometry. Precise control over the morphology of nanostructures is of great importance for realizing a variety of future technologies. These advantages are expected to induce a synergetic effect that enhances device performance, particularly in sensors. Thus, the multidimensional nanostructures were adopted to fabricate high-performance flexible gas sensors for detecting chemical nerve agents. The Brunauer −Emmett−Teller (BET) surface areas of the nanotubes increased in the following order: SL (31 m^2 g^{-1}) < NN (48 m^2 g^{-1}) < NR (62 m^2 g^{-1}).

To investigate the electrical property, the current−voltage ($I-V$) curves of the HPNTs on the sensor substrate were measured. All HPNTs displayed ohmic behavior in their $I-V$ characteristics, informing that the HPNTs made reliable electrical contact on the sensor substrate. The dI/dV values increased slightly, in the order SL < NN < NR, due primarily to internanotube contact resistance (Figure 13). The most significant factor may be the charge-transport property

of a HPNT depending on the morphology of the surface.
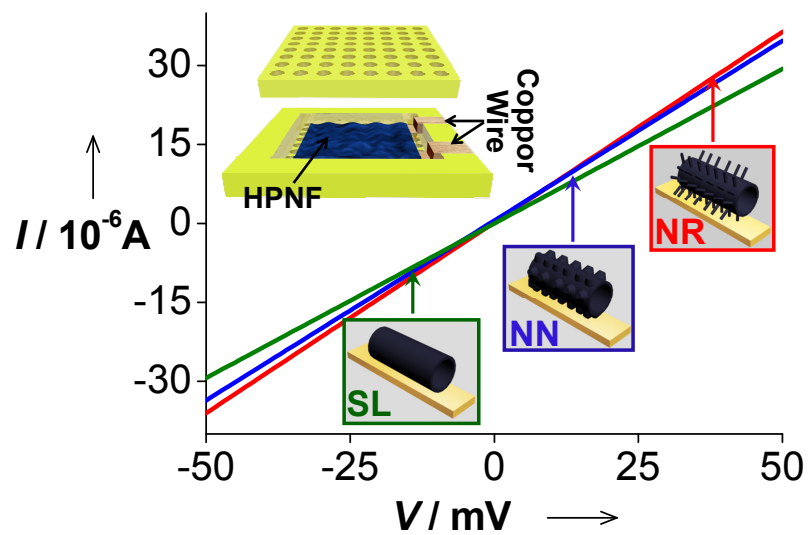
Figure 13. Schematic illustration of the custom-made sensor substrate used (left top inset) and *I−V* characteristics of HPNTs integrated in the sensor substrate (scan rate, 1 mV s^{-1}).

Figure 14 shows sensor system based on the simple change in resistance or in current in response to the binding of analytes. The change in resistance was recorded in real time upon cyclic exposure to DMMP and N_2 stream. Exposing HPNTs to DMMP elicited a precipitous rise in resistance (Figure 14). After the DMMP vapor was replaced by a N_2 flow, the resistance recovered to the original level. The NN-HPNTs and NR-HPNTs showed better responses to DMMP than did SLHPNTs (area, 10×10 mm; thickness, *ca*. 25 μm). Notably, NR-HPNTs had the lowest detection limit of 10 ppt (signal-to noise ratio: 3.2), which is 2−3 orders of magnitude more sensitive than previously reported DMMP sensors. The sensitivity was calculated by measuring the normalized electrical resistance change $\Delta R/R_0 = (R - R_0)/ R_0$, where R_0 and R are the measured real-time resistance and initial resistive value, respectively. The HPNTs had rapid response times (less than 1 s) as well as recovery times (3−25 s). The response time was defined as the time required for the conductance to reach 90% of the equilibrium value after a test gas was injected, and recovery time was the time necessary for a sensor to attain a conductance 10% above its original value in air. Additionally, they demonstrated excellent reproducibility and reversibility in responses (Figure 15 and 16). Importantly, the signal magnitude of the sensors could be correlated with the shape of the nanomaterials. Upon cyclic exposure to analyte vapors of a fixed concentration,

the sensors gave consistently larger response in the following order: SL< NN< NR. The calibration curves also demonstrated the shape-dependent response of the nanomaterials. The change in resistance at which the signal responses were saturated is plotted over a concentration range of 10 ppt to 50 ppb in Figure 16. The signal intensity increased in the order SL < NN < NR, which is consistent with the tendency in surface area. The oxidation level of PEDOT was extrinsically affected by hydrogen bonding rather than dielectric properties. DMMP is a strong electron donor, when HPNT was exposed to DMMP vapors The phosphoryl group provides great strength in hydrogen-bond basicity, and thus DMMP acts as a strong hydrogen-bond base that accepts protons from the HPEDOT. Because PEDOT is a p-type semiconductor, this phenomenon is accompanied by a decrease in PEDOT conductivity. As a control, pristine PEDOT nanotubes with no functionalized hydroxyl groups did not show remarkable responses on exposure to DMMP vapors (Figure 17).
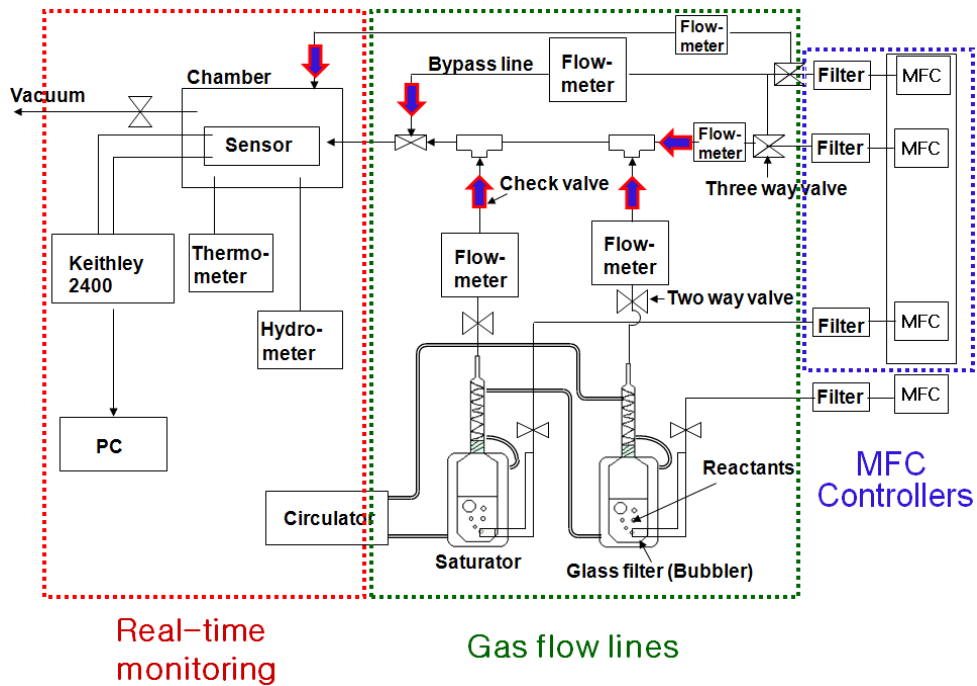
Figure 14. Diagram of gas sensor system.
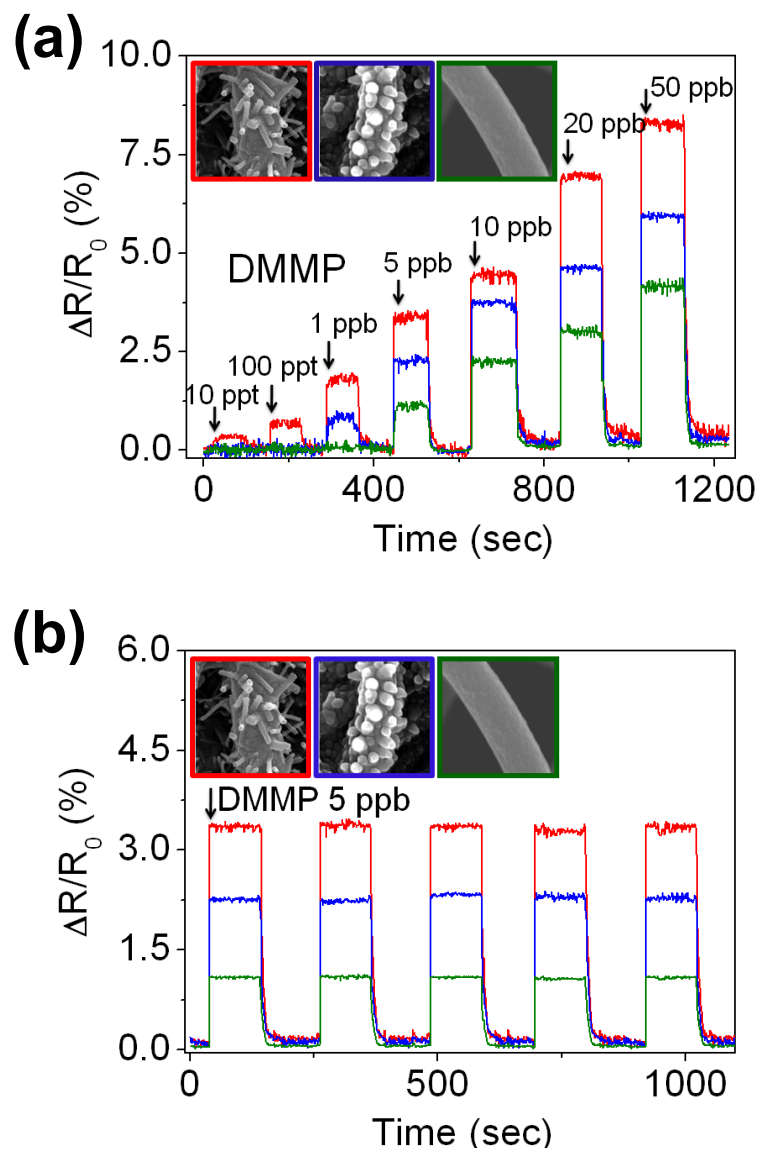
Figure 15. Real-time responses of HPNTs upon (a) cyclic exposure to DMMP (10 ppt to 50 ppb) and N2 streams (b) periodic exposure to 5 ppb DMMP.
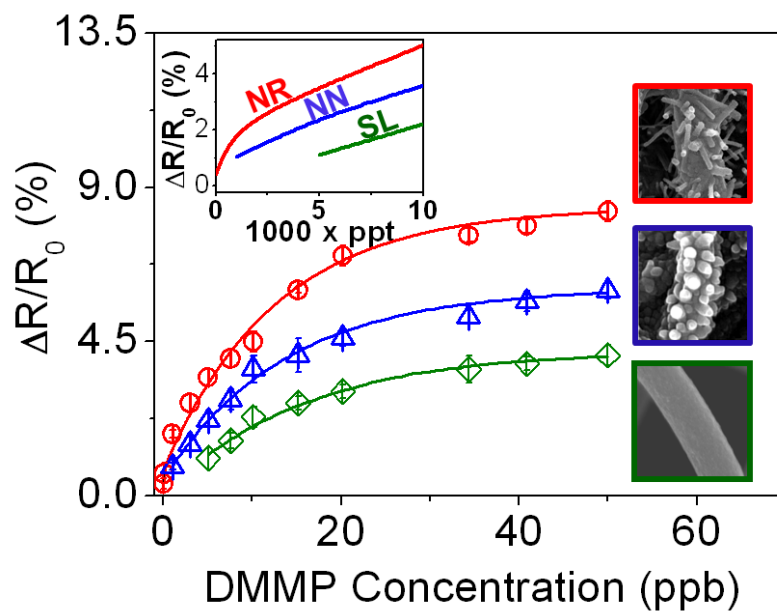
Figure 16. Changes in response intensity of HPNTs as a function of DMMP vapor concentration: the response intensity was determined as the $\Delta R/R_0$ (%) measured when the saturated value was reached after exposure to DMMP.
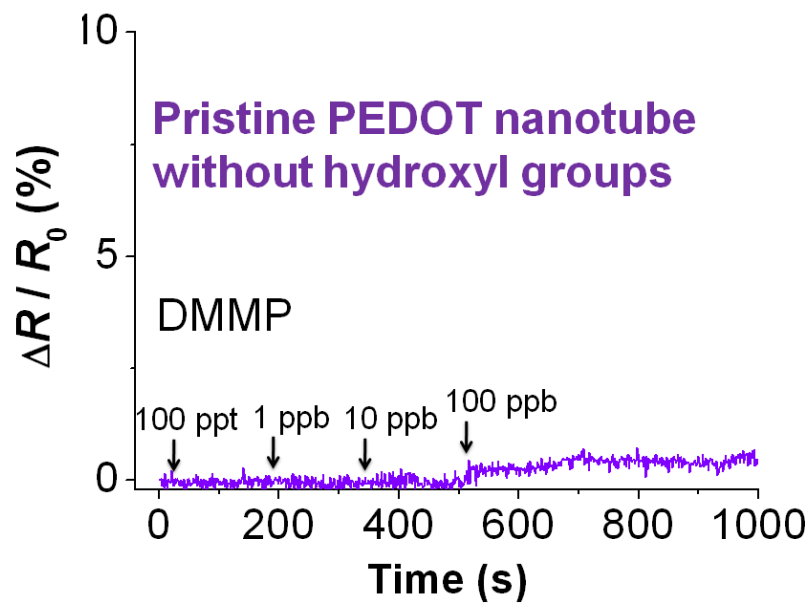
Figure 17. Real-time response of pristine PEDOT nanotubes without hydroxyl groups to DMMP gas: the signal-to-noise ratio at 100 ppb was much low as 0.13.

The response of the HPNTs was further examined upon consecutive exposure to different concentrations of DMMP vapor (Figure 18). Compared with the case of the cyclic DMMP/N_2 exposure, the response intensity was similar at low concentrations. However, the response intensity appeared to decrease at higher concentrations of more than 5 ppb, as seen in Figure 19. A portion of the reaction sites of the HPNTs would remain bound with DMMP under the consecutive exposure, leading to the reduction in response intensity. Thus, the HPNTs need to be recovered to their initial state for the quantitative analysis of target DMMP vapor. Figure 20 shows the effect of the nanotube surface substructure on the electrical response. The response intensity increased with increasing population of the substructures, reconfirming that precise control of the morphology of the transducer allows modulation of sensor performance. The response intensity was determined as the $\Delta R/R_0$ measured when the saturated value was reached after exposure to DMMP.
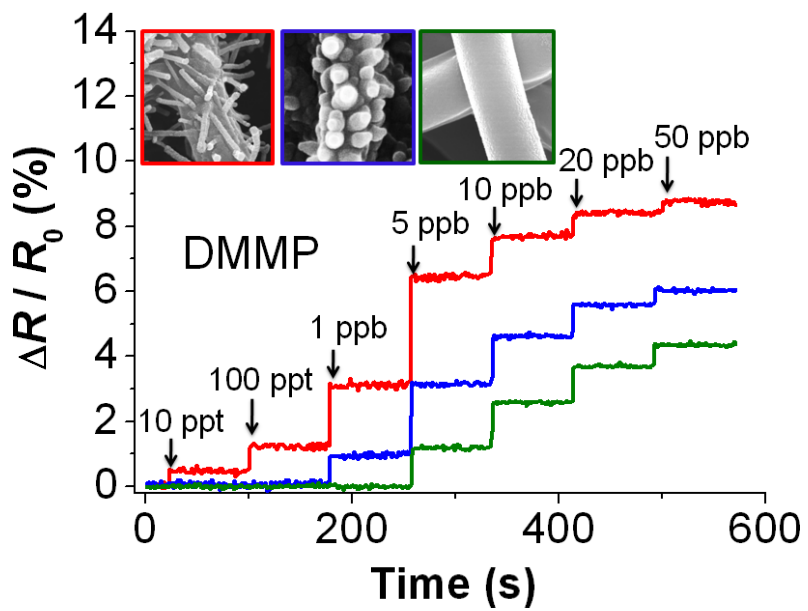
Figure 18. Real-time responses of HPNTs upon consecutive exposure to DMMP (10 ppt to 50 ppb).
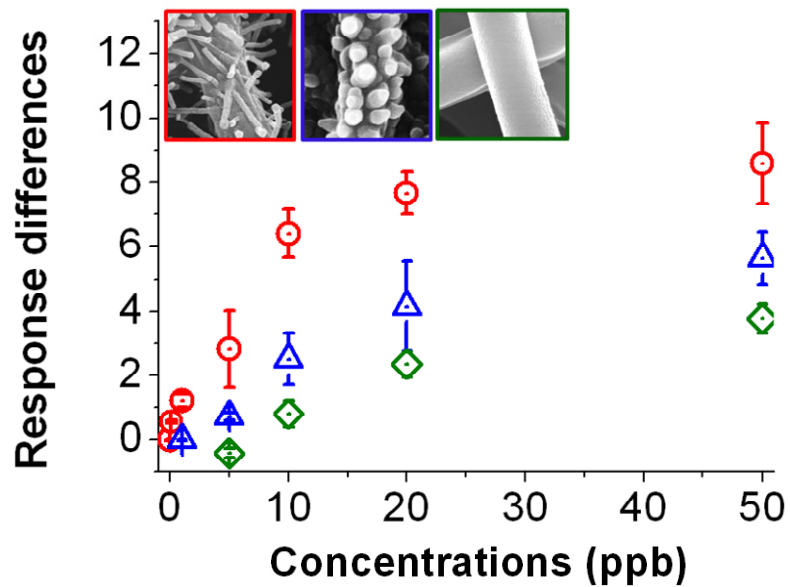
Figure 19. Response differences between continuous addition and cycle DMMP/N2. The response difference was calculated by the difference between the response intensities obtained from cyclic DMMP/ N_2 exposure and consecutive DMMP exposure.
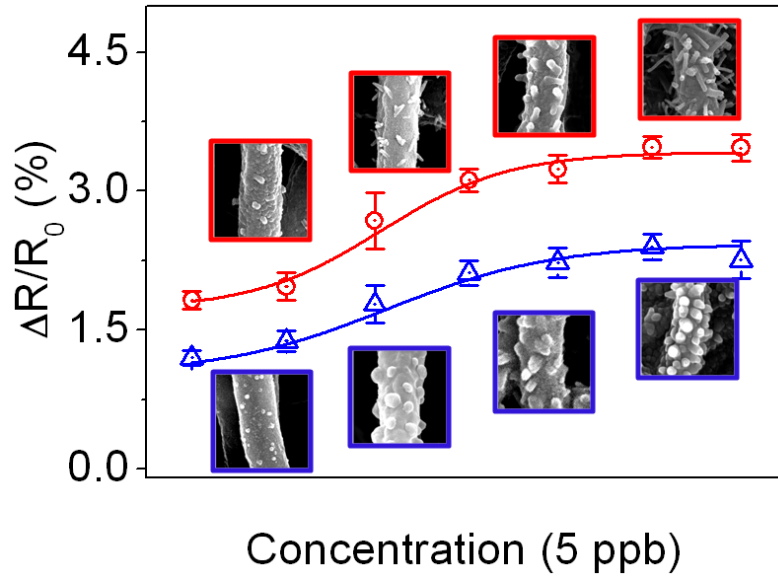
Figure 20. Real-time responses of HPNTs on periodic exposure to 5 ppb DMMP.

3.1.6. Selectivity test of multidimensional HPNTs toward similar organophosphorus compounds.

The responses of HPNTs toward similar organophosphorus compounds were also explored to evaluate their selectivity. Figure 21 summarizes the responses of HPNTs on exposure to trimethyl phosphate (TMP), methyl dichlorophosphate (MDCP), and trichlorophosphate (TCP), used as nerve gas simulants. The ability of a phosphoryl group to form a hydrogen bond depends on the chemical environment of the compound to which it is attached. Those compounds also contain methoxy groups that can act as weak hydrogen-bond acceptors. The hydrogen-bond strength increased in the order TCP < MDCP (QH = 1.64) < sarin (QH = 2.26) ≈ DMMP (QH = 2.28) < TMP (QH = 2.79) (the absolute value (QH) value is the difference between the negatively charged atoms and the positively charged atoms calculated with Hu¨ckel charges), which leads to different response intensities with the same tendency (Figure 21). The HPNTs was further tested against 15 volatile organic compounds, selected as possibly interfering with the response, and its response was compared to responses from other sensing materials. Principal components analysis was performed on the detection data that were collected from two HPEDOT (NN and NR) nanotubes, pristine PEDOT nanotubes, and polypyrrole nanotubes. The first three principal component scores, accounting

for a total 99.9% of the total data variance, are plotted in Figure 22. Unique signatures of the analytes were observed, denoted by their segregation into separate regions of the plot, allowing identification of individual analytes by their responses. In particular, DMMP had clearly differentiable components, which validated the selective recognition ability of HPNTs.

The intermolecular interaction between hydroxylated PEDOT (HPEDOT) nanotubes and analytes was estimated by MM2 model in Chem3D Pro. (Table 2.) The graphics in the right column display molecular configurations obtained using an energy-minimization method at 300 K. Strongly positive charged atoms appear red while strongly negative atoms appear blue. Lesser positively and negatively charged atoms also appear somewhere within the color range, depending on the value. The white dotted line indicates hydrogen bond between the corresponding atoms. Hückel charges are calculated for the atoms that can make hydrogen bonds. The absolute value (QH) of the difference between the negatively charged atoms and the positively charged atoms is estimated, which gives good indication of the hydrogen bond strength.
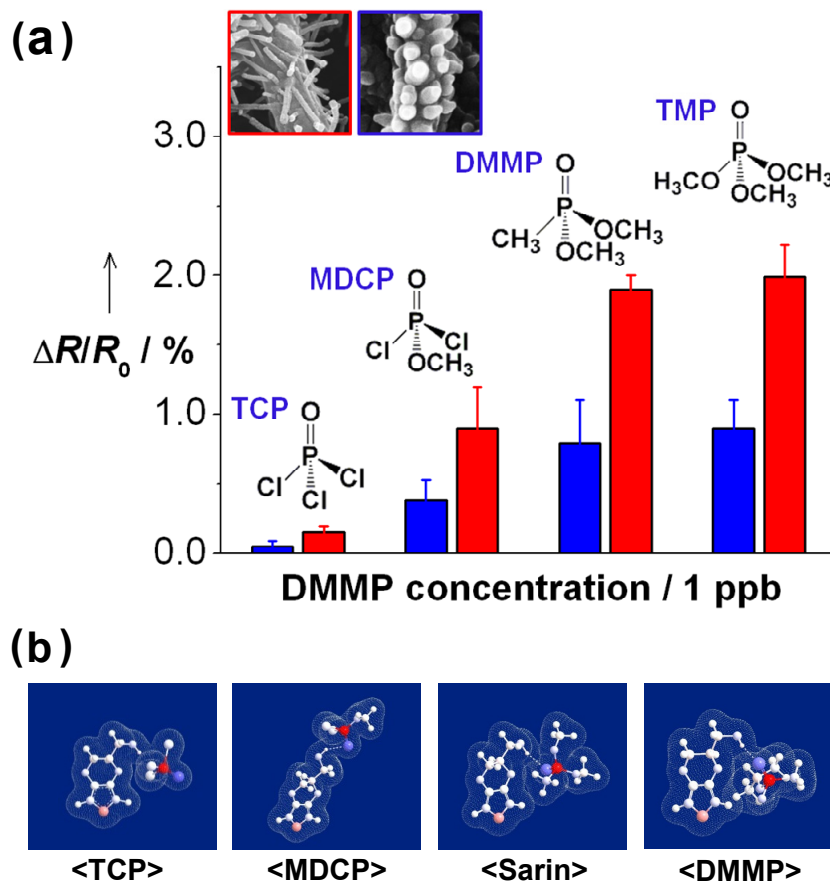
Figure 21. Sensing performance of chemical nerve agent sensor based on HPNTs. (a) Histogram showing the response of HPNTs toward similar organophosphorus compounds at 1 ppb (TCP, MDCP, DMMP, TMP). (b) 3D graphics showing the formation of hydrogen bonds between nerve agent stimulant molecules and HEDOT.
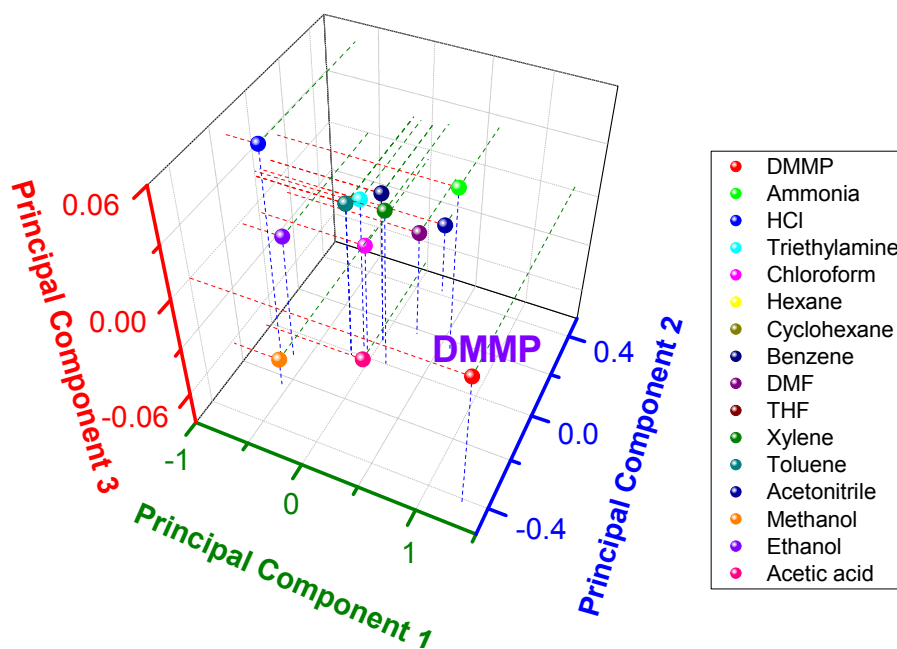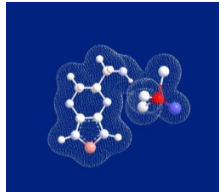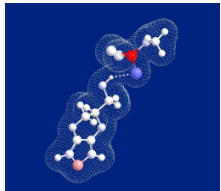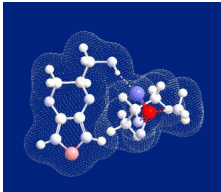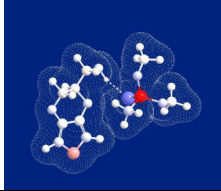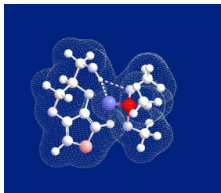
Figure 22. Principal components analysis plot using response intensity inputs from four CP nanomaterials (NN-HPNT, NR-HPNT, pristine PEDOT nanotubes, and PPy nanotubes) to the 16 analytes (including DMMP): each analyte concentration was fixed at around 4 ppm.

Table 2. Summary of the characteristics of nerve gas simulants (TCP, MDCP, DMMP and TMP) and Sarin with respect to the formation of hydrogen bonds.

Name	Molecular formula		3D graphic
TCP	Cl_3OP	No hydrogen bond is estimated between –OH and –P=O, as shown in the right graphic. It was reported in the literature that TCP has a weak hydrogen bond. TCP has three Cl atoms and thus it probably prefers to H-Cl dipole-dipole interaction.	
MDCP	$ClCH_3O_2P$	As exhibited in the right graphic, the formation of a hydrogen bond is made between –OH and –P=O. The methoxy group is also possible to make a weak hydrogen bond. The Q_H is calculated to be 1.64.	
Sarin	$C_4H_{10}FO_2P$	Besides –P=O, Sarin has F and O atoms that can contribute the formation of hydrogen bonds. The Q_H is calculated to be 2.26, which is almost similar with that of DMMP.	
DMMP	$C_3H_9O_3P$	DMMP has additional two methoxy groups. The Q_H is calculated to be 2.28.	
TMP	$C_3H_9O_4P$	TMP has three methoxy groups that can make extra hydrogen bonds. The right graphic displays two hydrogen bonds simultaneously formed between PEDOT-OH and TMP. The Q_H is calculated to be 2.79.	

3.1.7. Alignment of multidimensional nanostructures with HPNTs.

To optimize conditions, the sensing capability of the HPNTs was systematically investigated. Several crucial factors were further considered to optimize sensor performance, such as conductive pathway and effective surface area. First, the nanofiber template was axially aligned via the electrospinning process under a magnetic field to produce highly oriented nanotubes (Figure 23 and 24). This enhanced orientation of CP nanotubes reduced conformational defects in the molecular structures and thus allowed efficient electronic delocalization.. The aligned HPNTs had better charge-transport properties (Figure 25). Figure 26a shows the responses of aligned and nonaligned SL-HPNTs to 5 ppb DMMP. Moreover, their responses were also about 30% larger than those of nonaligned HPNTs over a wide range of concentrations (Figure 26).
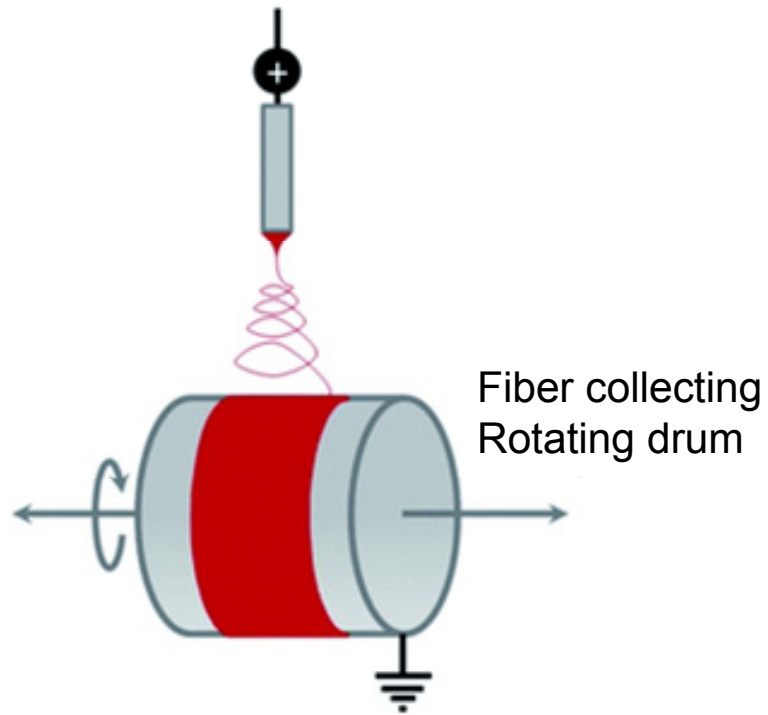
Figure 23. The schematic diagram of the electrospinning process under a magnetic field to produce highly oriented nanotubes.
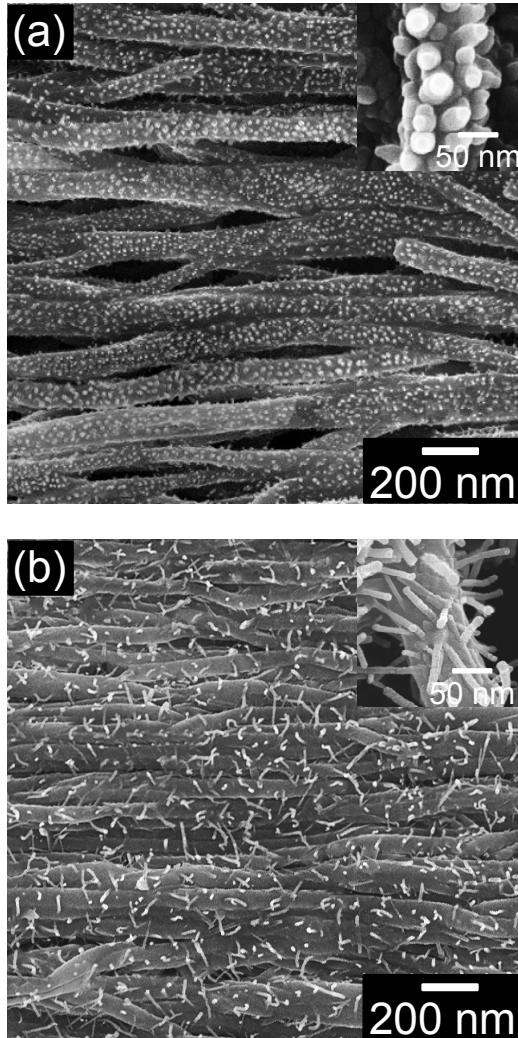
Figure 24. The SEM images of aligned (a) NN and (b) NR-HPNTs.
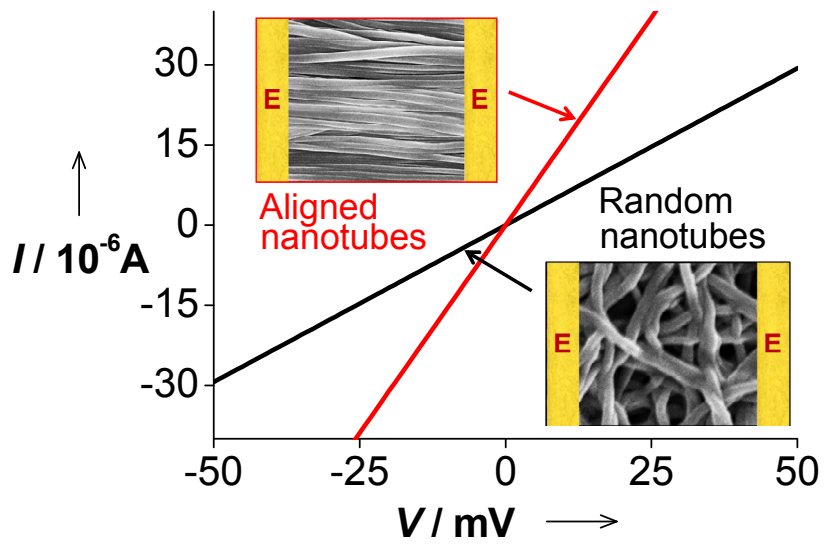
Figure 25. *I−V* curves of nonaligned and aligned SL-HPNTs (the insets indicate SEM images of (upper left) aligned and (under right) nonaligned SL-HPNTs, scan rate was 1mV s^{-1})
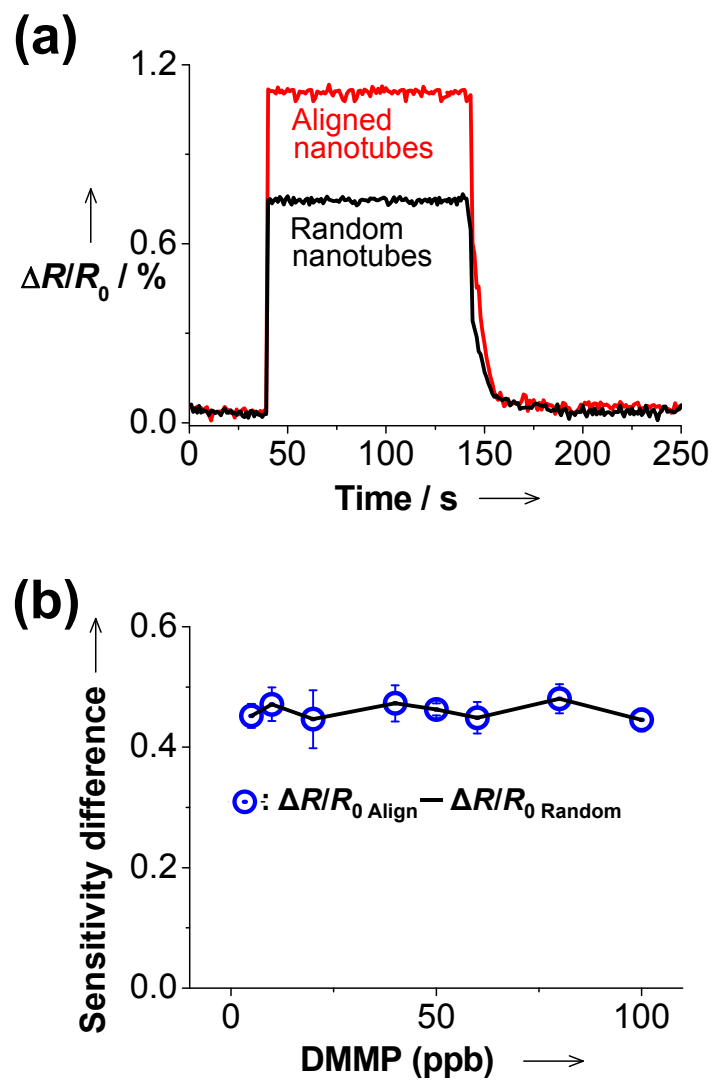
Figure 26. (a) Comparison of response intensity from nonaligned and aligned SL-HPNTs at 5 ppb DMMP (b) The difference in response intensity between nonaligned and aligned HPNTs was plotted for 5−100 ppb DMMP.

3.1.8. Flexiblity test on the PET film.

CPs are excellent candidate materials for developing flexible, wearable, or even implantable sensors because they have chemical, thermal, and mechanical properties that are similar to common plastic substrates.[175-181] The HPNT deposited on a cellulose substrate was transferred to a plastic substrate, poly(ethylene terephthalate) (PET) film, via the dry-transfer method (Figure 27). To assess the mechanical flexibility of the aligned HPNT sensor on the PET substrate, the dependence of the HPNT resistance on the bend radius was examined (Figure 28a). The resistances perpendicular (Rx) and parallel (Ry) to the bending direction, x and y, were measured. (inset: Photo of the apparatus showing the direction of measuring resistance). The resistance varied little up to a bend radius of 17 mm and was completely restored to the original level after unbending even for a bend radius as high as 3 mm. The change in resistance affected the response intensity of the sensor. As shown in Figure 28b, the response intensity decreased by a maximum of 5% at a bend radius range of 3 mm, indicating an almost folded state. The insets show the consequent changes in shape of the HPNT at each bend radius. However, there was only a small decrease (less than 2%) in response intensity under a moderate bend radius, in the range of 10−20 mm.
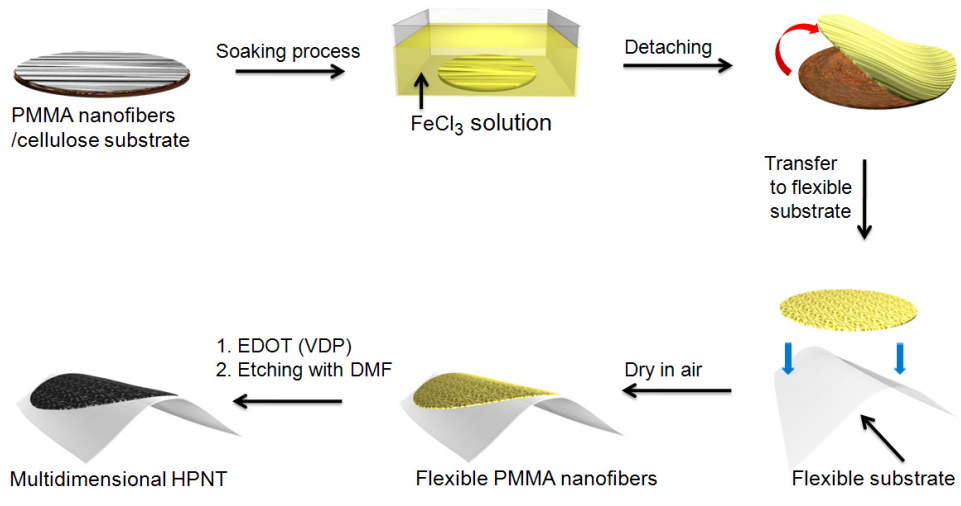
Figure 27. Dry-transfer method of multidimensional HPNT on flexible substrate.
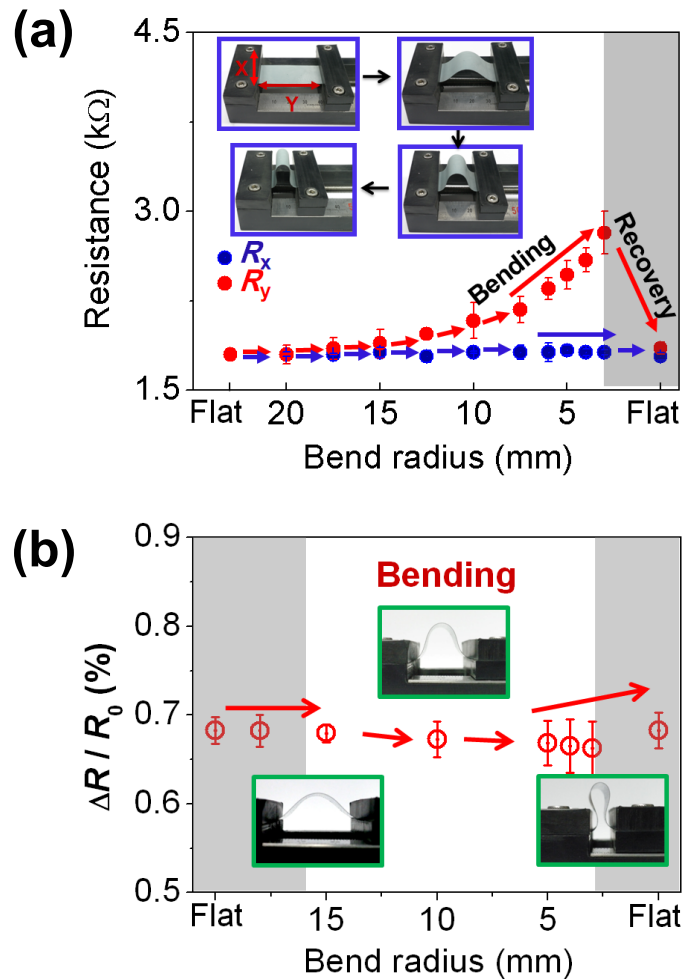
Figure 28. Flexible HPNT sensors. (a) Variation in resistance of NR-HPNT deposited on a 80 μm thick PET substrate for different bend radii, which were adjusted by changing distances between holding stages (see the inset): (b) Variation in the intensity of the response of NR-HPNT deposited on the PET substrate for different bend radii (at 100 ppt DMMP).

To further demonstrate the flexibility of the HPNT sensors, a wearable measuring system was built by assembling a HPNT sensor substrate on gloves (Figure 29). Conductive silver epoxy was used to achieve stable electrical contact between the HPNT and connecting wires, and the HPNT sensor substrate was secured on gloves with aid of a polydimethylsiloxane (PDMS) rubber glue. Figure 30a shows the typical change in response intensity after repeated bending/ relaxing. The response decreased by less than 5% after 100 bending cycles. Thus, the HPNT sensor has excellent mechanical bendability and durability, opening the possibility of fabricating reliable flexible wearable sensors after further optimization. Figure 30b shows the HPNT sensor positioned on a subject's hand. The bending of finger caused a deformative effect comparable to a bend radius of 10 mm. A fatigue test was conducted for the flexible sensor device.
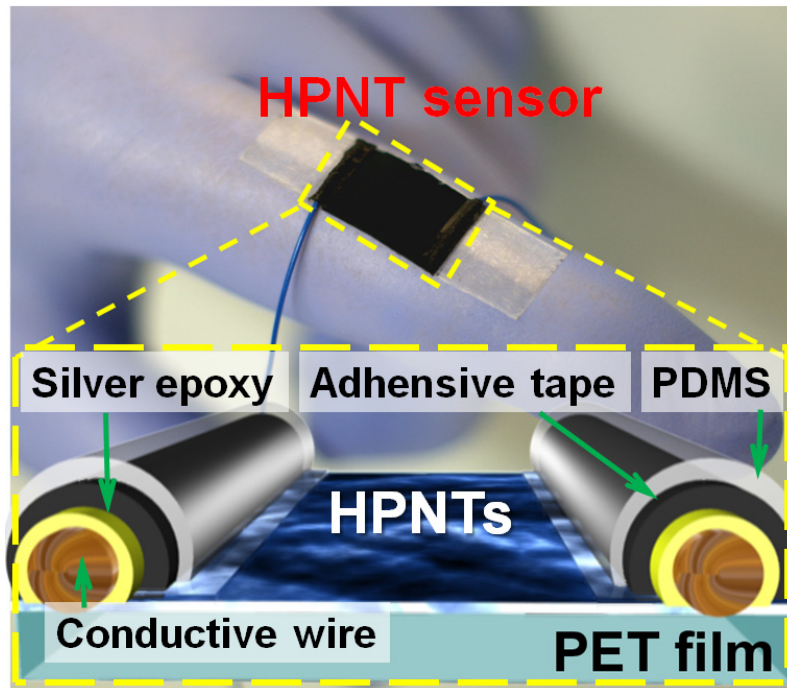
Figure 29. Photograph (the top) and schematic illustration (the bottom) of flexible HPNT sensor in wearable system.
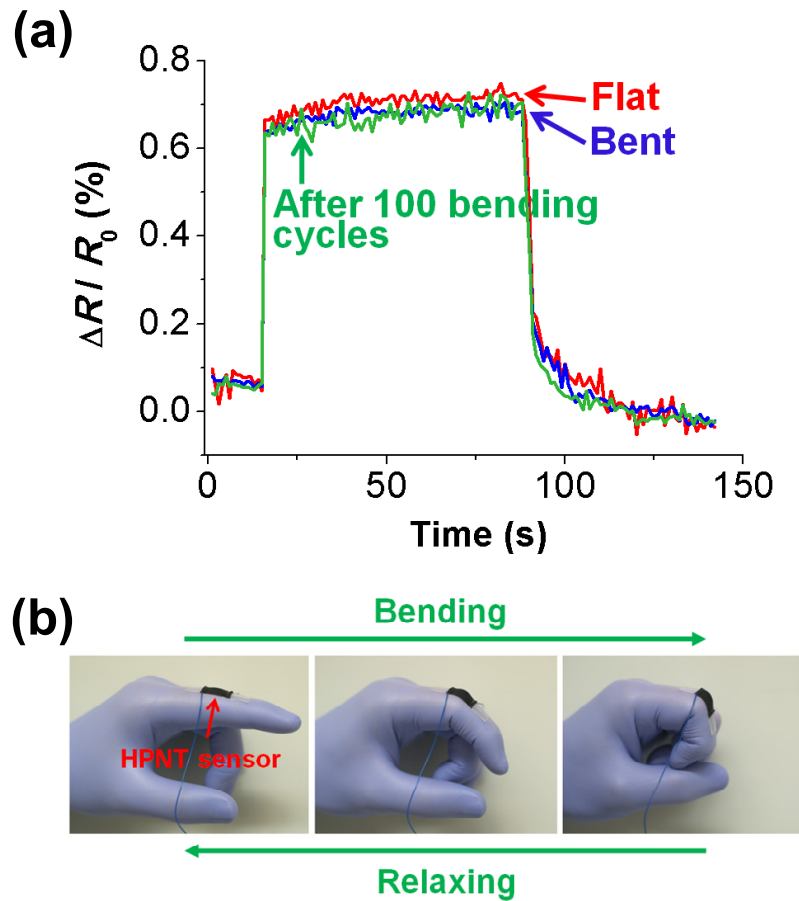
Figure 30. (a) Sensing behaviors of the flexible HPNT sensor when measured in a flat state (red) and in a curved state (blue). The fatigue test (green) was carried out by bending and relaxing the sensor for 100 times and measuring it on a flat state. The concentration of DMMP was 100 ppt. The real-time responses were measured by the data based on the parallel resistances (Ry direction). (b) Representative photographs showing finger motions during fatigue test.

87

3.2. High-Performance Field-Effect-Transistor (FET) - Type Dopamine Biosensor Using Multidimensional Carboxylated Poly(3,4-ethylenedioxythiophene) (CPEDOT) Conjugated With Dopamine Receptor Nanoplatform.

3.2.1. Fabrication of multidimensional nanostructure based on the carboxylated PEDOT (CPEDOT) with dopamine receptor.

Previously, we have synthesized multidimensional nanostructures with PEDOT as transistor of chemi-sensor applications (3.1. part). Continuously, multidimensional carboxylated poly(3,4-ethylenedioxythiophene) (MCPEDOT) nanotubes with nanorods (NRs) were fabricated by using vapor deposition polymerization and transferred on the flexible substrate. Specifically, Subsequently, it was functionalized with carboxyl groups by using the mixture of the carboxylated EDOT monomer and EDOT monomer. Moreover, the glass container was stored under controlled temperature and pressure, resulting that the MCPEDOT NFs were fabricated through the chemical polymerization on the surface of the PMMA NFs. Figure 31 illustrated the method of fabrication for MCPEDOT NFs and the scanning electron microscopy (SEM) of both PMMA template and MCPEDOT NFs with PMMA template. It showed that the diameter of PMMA was *ca.* 60 nm and the shell-thickness increased after formation of MCPEDOT on the PMMA template (*ca.* 20 nm). Moreover, the

color of the membrane was changed after vapor deposition polymerization
(VDP).
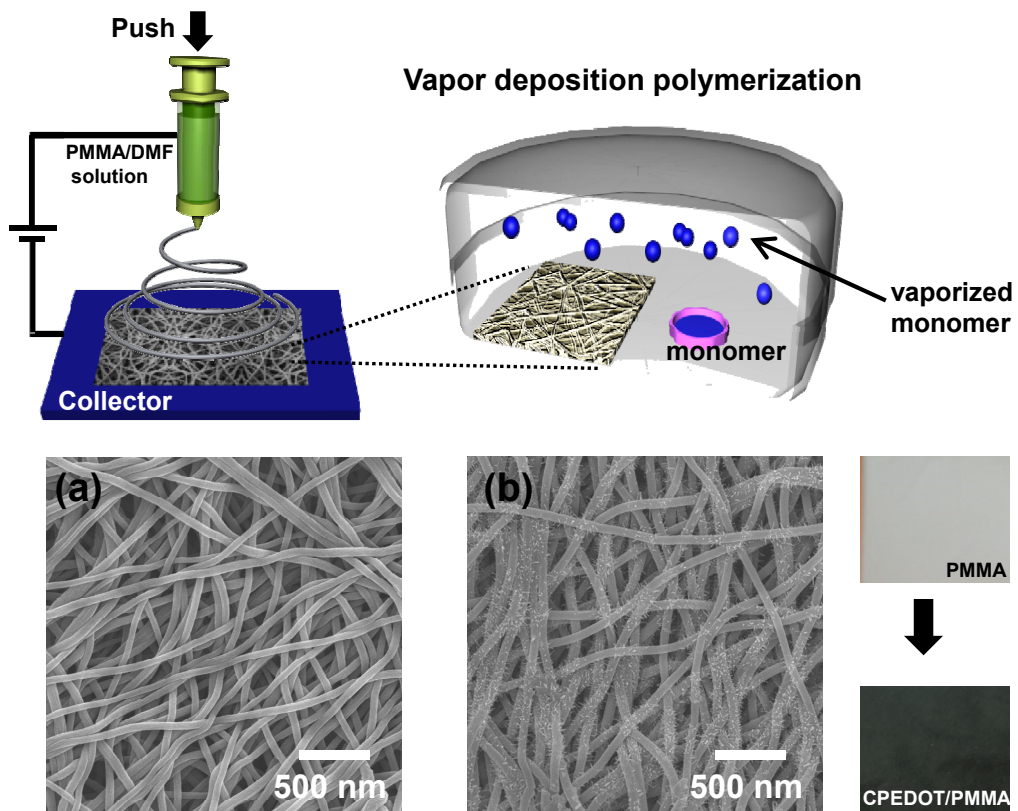
Figure 31. Schematic illustration of fabrication of MCPEDOT NFs by electrospinning and vapor deposition polymerization and FE-SEM images of (a) PMMA template and (b) MCPEDOT NFs with PMMA template.

3.2.2. Construction of dopamine sensor based on dopamine receptor-conjugated multidimensional CPEDOT nanobiohybrids.

The MCPEDOT NTs were constructed by etching PMMA NFs in core part with DMF solvent (Figure 27). Finally, the MPEDOT NTs on the flexible substrate were successfully constructed for the FET-type biosensing geometry. Surprisingly, as shown in Figure 32a, the nanorods was grown on the surface of the CPEDOT NTs, leading to the enhanced surface areas compared to conventional 1D nanostructures. The dopamine receptor (DR) was also observed on the surface of the MCPEDOT NTs by chemical attachment between –COOH group of MCPEDOT NTs and –NH$_2$ group of the dopamine receptors with a condensation reagent . Figurue 32 displays typical field-emission scanning electron microscopy (FE-SEM) images of FET sensor platform of MCPEDOT NTs (a) without and (b) with DR.. From FE-SEM analysis, the surface of MCPEDOT NTs had rougher after the introduction of the DR. This immobilization of DR provides attractive benefits such as physical stability in the liquid-phase and efficient electron pathway toward FET-transistor. Moreover, the Fourier transfer infrared (FTIR) spectroscopy was used to confirm the chemical binding of DR on the MCPEDOT NTs. The absorption peaks for DR, CPEDOT NTs, and DR-CPEDOT NTs was displayed with clear peak differences (Figure 33). Generally, the amide I (at 1630 cm^{-1})

and II (at 1520 cm^{-1}) bands result from combination with protein molecules. The amide, methyl, and methylene groups binding vibrations and the alkyl, carbonyl, and amine group stretching vibrations of DR were found at 1200 and 3200 cm^{-1}. The FTIR spectrum of MCPEDOT NTs had a broad -OH band at 3200 cm^{-1}, a broad NH band at 3300 cm^{-1}, a sharp –C=O band at 1700 cm^{-1}, and strong –C-N bands at 1473 and 1180–1360 cm^{-1}. There were no significant absorption peaks corresponding to the amide I and II bands. Interestingly, the FTIR spectrum of the DR attached-MCPEDOT NTs had amide I and II bands, which indicated successful attachment of DR to the surface of MCPEDOT NTs. The amount of DR on the surface of the MCPEDOT was estimated using the bicinchoninic acid (BCA) in protein assay. The amount of the DR immobilized on the surface of the MCPEDOT was *ca.* 0.023 mg, leading to a more efficient interaction toward specific biomarkers.
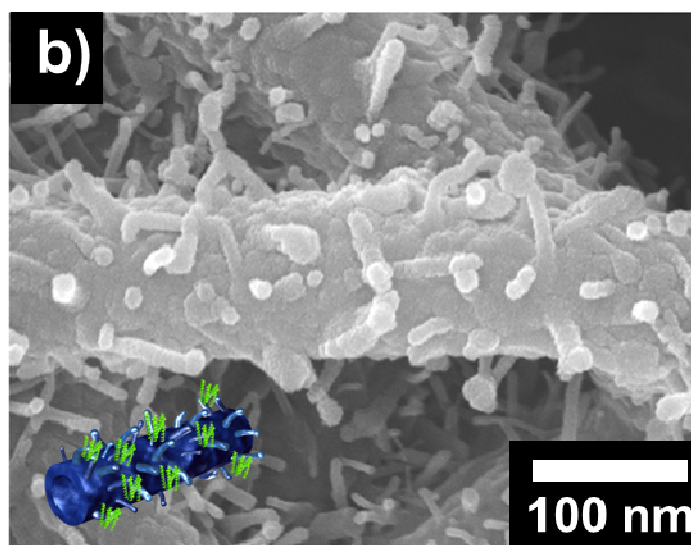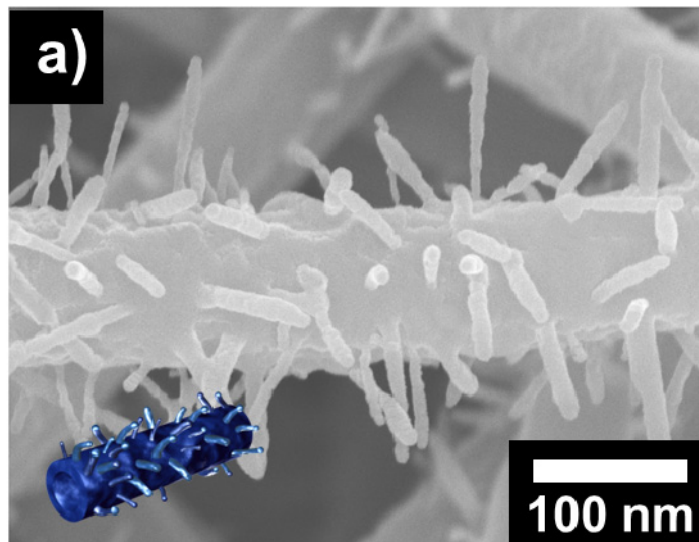
Figure 32. Typical FE-SEM images of FET sensor platform of MCPEDOT NTs (a) without and (b) with DR.
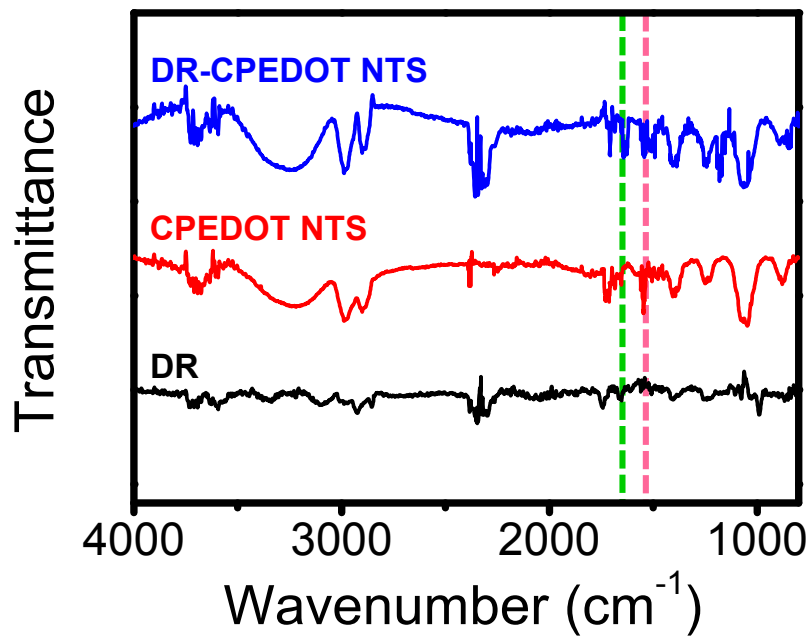
Figure 33. FT-IR spectra of Dopamine receptor (DR), CPEDOT NTs, and DR-CPEDOT NTs. The amide I and II bands are displayed by the green (at 1630 cm^{-1}) and pink (at 1520 cm^{-1}) background colors.

3.2.3. Characterization of FET-type dopamine sensor.

To confirm the electrical properties of the DR-MCPEDOT NT sensing geometry, we obtained the current-voltage (*I-V*) curves for DR-MCPEDOT NTs. Figure 34 displays the *I-V* characteristics of the electrode surface-adsorbed CPEDOT, before and after DR immobilization. The *I-V* changes of the MCPEDOT NT substrate were continuously maintained with linear curves over a voltage range from -0.5 V to 0.5 V, demonstrating stable ohmic behavior of the nanomaterials on the electrodes.

To utilize DR-MCPEDOT NTs as the signal transducing component of the biosensor, a liquid-ion gated FET system was constructed by the surrounding PBS (pH 7.4) as the electrolyte. Generally, in biosensors, the analytes exist in a liquid state and require optimal environmental conditions. High-performance biosensors require stable transducers with excellent electrical properties that can induce significant binding events between the transducer and sensing elements in the liquid state. Therefore, a liquid-ion gated FET system was introduced in this study. Liquid-ion gating allows for a significant contact area for on the wide-range areas of the DR-MCPEDOT NTs via a controllable gate electrode in the electrolyte and operates as a signal amplifier to enhance the sensing performance of sensitively resistive sensors. Figure 35 shows the out-put characteristics of the FET-type DR-MCPEDOT NT biosensor at room

temperature. The drain-to-source current (I_{ds}) negatively increased with negatively increasing gate voltage; this was induced by an increment in the oxidation level of the CP chains, indicating clearly p-type behavior (hole-transporting). The binding events between the DA molecules and DR-MCPEDOT NTs bridged on source and drain of electrodes can be monitored by measuring the current output under controlled gating voltages.
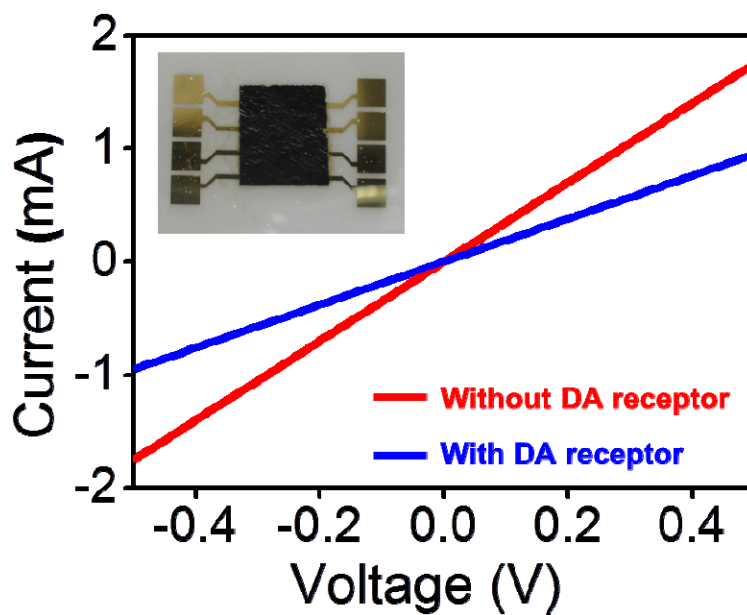
Figure 34. Current-voltage (*I-V*) curves of MCPEDOT NTs on the flexible electrode before (red line) and after (blue line) the introduction of the DR (V_{ds} scan rate = 10 mV s^{-1}).
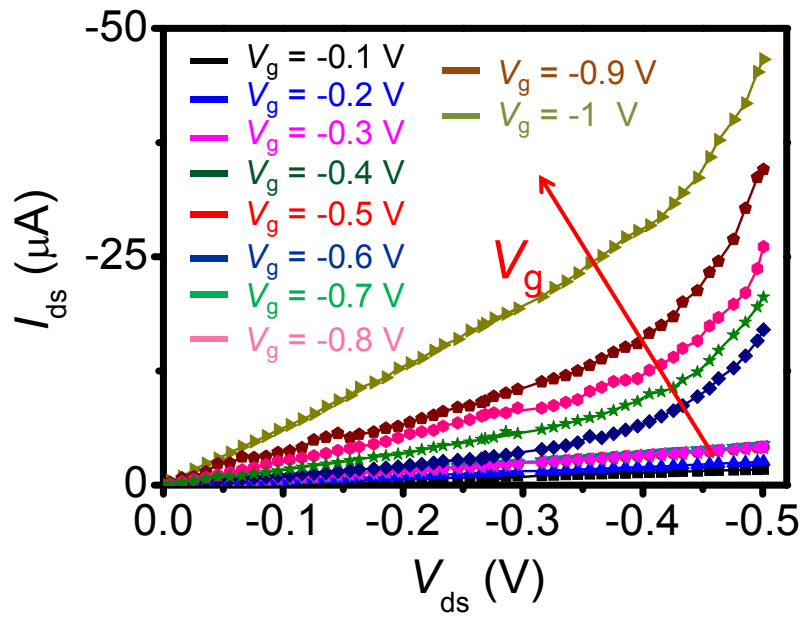
Figure 35. Output curves of the FET-type DR-MCPEDOT NT (V_g was from -0.1 to -1 V in a step of -0.1 V and V_{ds} scan rate was -5 mV s^{-1}).

3.2.4. Real-time responses of dopamine sensor.

The FET-type DA biosensor produced rapid real-time responses with high sensitivity and selectivity. To evaluate the sensing characteristics of the DR-MCPEDOT NTs-based FET-type DA biosensors surrounded with PBS, the field-induced Ids was measured as a function of DA concentration for V_{ds} = - 50 mV, under a low operating voltage (V_g = - 50 mV). The principal function of the DA receptor is to bind with the molecules and induces the electrical changes by the rearrangement of the DR on the MCPEDOT NTs substrate. The interaction of DA toward the DR can affected the charge carrier density on the surface of the MCPEDOT NTs, indirectly. Figure 36 displays the real-time response of the FET-type DA biosensor, after the introduction of various concentrations of DA. The FET-type biosensor based on DR-MCPEDOT NTs exhibited a concentration-dependent decrement in I_{ds} upon exposure to DA molecules. It can be explained by the accumulation of the charge carriers (holes) due to the rearrangement of the DR. The specific binding of DR/DA promotes the charge change, resulting in the generation of negative point charges in the liquid-ion gate dielectric near the MCPEDOT NT surface. Therefore, the positively charged carriers in the CPEDOT NTs channel increased, leading to the increasing current changes. From this sensing mechanism, no significant signal was obtained from the pristine MCPEDOT

99

NTs without DR as a control experiment. Unprecedentedly MDL of the FET-type DA biosensors using DR-MCPEDOT NTs was *ca.* 0.1 fM, which is approximately 3~4 orders of magnitude lower than that of various conventional CP-based DA biosensors. In all of the measurements, the FET-type DA biosensors exhibited a rapid response time of less than 1 s, because receptor signaling in sensory transduction is relatively fast on the order of milliseconds. Figure 37 shows the highly selective responses of the FET-type DA biosensor toward molecules containing similar structures. No significant changes in I_{ds} were observed upon the addition of non-target neurotransmitters and precursor, including serotonin, epinephrine, tyrosine, phenethylamine, and norepinephrine; however, a change in I_{ds} was clearly evident with the addition of DA, for concentrations as low as 0.1 fM. Thus, a high-performance DA biosensor can be created by DR-MCPEDOT NTs.
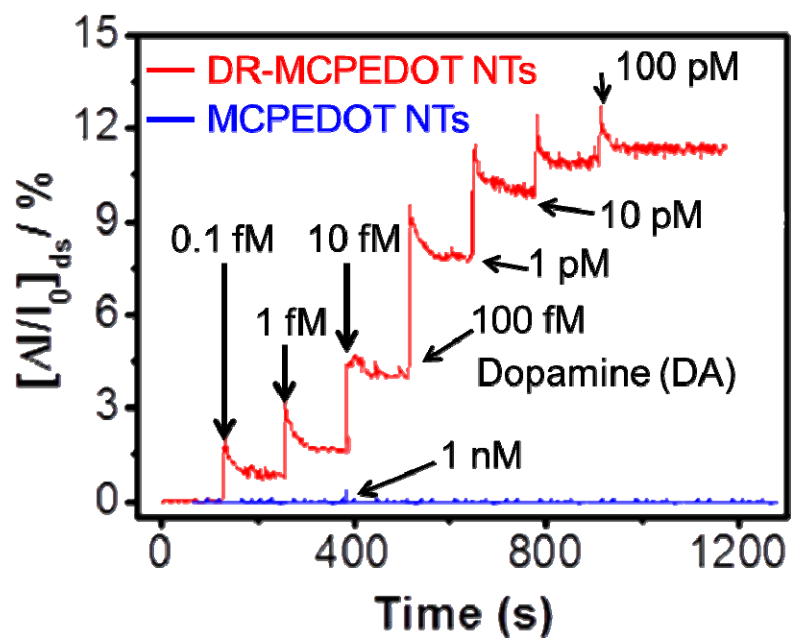
Figure 36. Real-time responses with normalized current changes ($\Delta I/I_0$) of MCPEDOT NTs toward various DA concentrations; Red line means signal with DR-MCPEDOT NTs; Blue line means signal with MCPEDOT NTs.
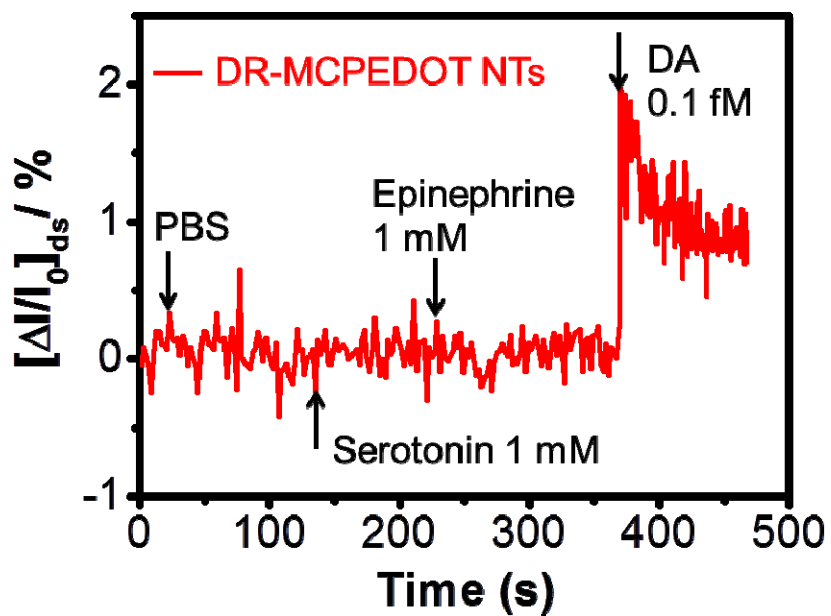
Figure 37. Selective responses of the DA biosensor using MCPEDOT NTs toward non-target neurotransmitters (PBS, 1 mM Serotonin, and 1 mM Epinephrine) and dopamine (10 pM DA).

3.3. Fabrication of Multidimensional Ag NPs/CPEDOT Nanohybrids for H$_2$O$_2$ sensor.

3.3.1. Preparation of multidimensional Ag NPs/CPEDOT NTs nanohybrids using AAO template *via* one-pot synthesis.

Figure 38 describes the overall synthetic procedure of Ag NPs/CPEDOT NTs. First, Fe/Ag cations were adsorbed on the AAO template through dipping AAO into the solution from 30 % (wt/wt) Fe(NO$_3$)$_3$ with various AgNO$_3$ concentrations. When Fe/Ag cations are fully adsorbed, the AAO membrane with EDOT-carboxylic acid was placed into the custom-made apparatus for VDP. Vaporized EDOT-carboxylic acid monomers were chemically polymerized by Fe cations adsorbed on an AAO template at 150 ^{o}C and 10^{-2} Torr. Then, the Ag NPs introduced into the surface of polymer NTs after formation of CPEDOT NTs. In this stage, it is known that Ag cations can be reduced to Ag NPs by PEDOT [182-186]. Thus, CPEDOT NTs and Ag NPs were simultaneously formed during polymerization procedure without any further treatments such as a reducing agents or UV irradiations.
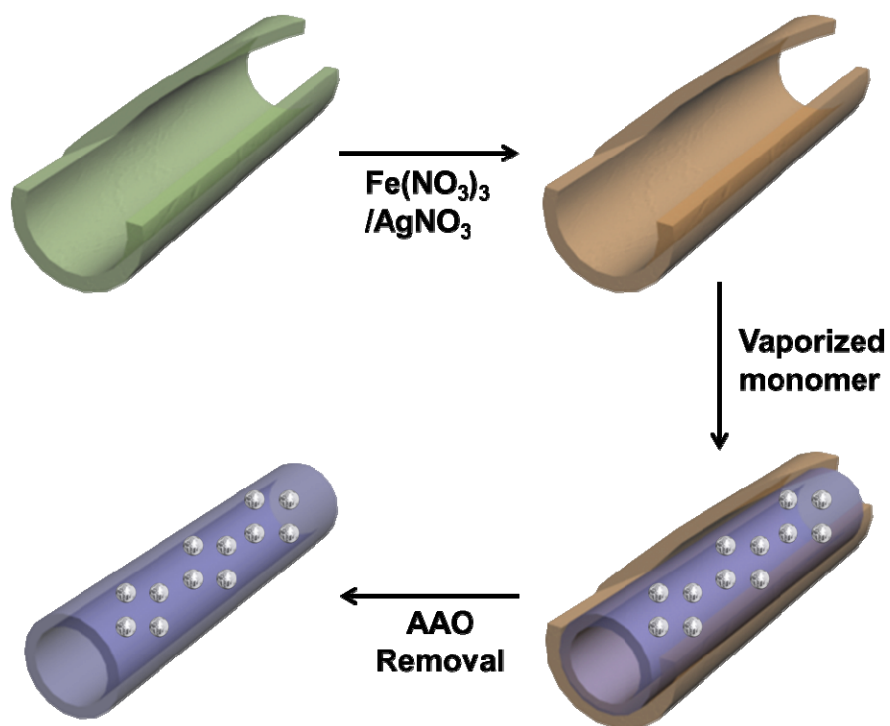
Figure 38. Overall procedure of Ag NPs/CPEDOT NTs.

3.3.2. Characterization of Ag NPs/CPEDOT NTs.

Figure 39 displays TEM images of pristine CPEDOT NTs and Ag NPs/CPEDOT NTs. The diameters and wall thicknesses of CPEDOT NTs were ca. 100 nm and 20 nm, respectively. These NTs also have well-defined hollow structures, tailored morphology and smooth inner/outer surface. The dark spots indicate Ag NPs with *ca*. 5 nm in average diameters, where decorated on the surface of CPEDOT NTs. Figure 39b, c exhibited TEM images of Ag NPs/CPEDOT NTs prepared with 5, 30 % (wt/wt) $AgNO_3$ concentration. The population of Ag NPs gradually increased with increasing $AgNO_3$ concentration because more Ag cations could be reduced to Ag NPs by PEDOT. Judging from these observation, the pristine CPEDOT NTs and Ag NPs/CPEDOT NTs were successfully prepared by VDP mediated hard template method via one-pot synthesis.
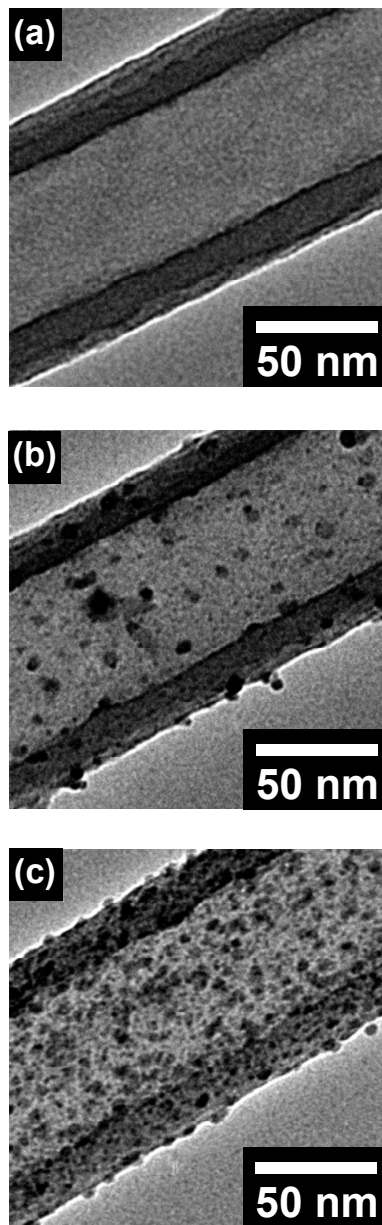
Figure 39. The transmission electron microscope (TEM) images of (a) pristine CPEDOT NT and Ag NPs/CPEDOT NTs with (b) 5 and (c) 30 % (wt/wt) AgNO$_3$ concentrations.

The biosensor applications based on conducting polymers have been restricted to the gas phase analytes due to the lack of adhesion to the electrode [187]. To overcome this barrier, CPEDOT NTs were employed to immobilize conducting polymer transducer on the electrode. Compared to the peaks of pristine PEDOT NTs, the sharp O peaks indicated that the presence of carbonyl groups in the CPEDOT NTs in Figure 40. In the first stage, the surface of the electrode was functionalized by primary amino group using (3-aminopropyl) trimethoxysilane (APS) and the NTs were fixed onto the electrode through coupling reaction between the amino group of APS and the carboxyl group of CPEDOT NTs. Therefore, Ag NPs/CPEDOT NTs can secure the substrate stability against environmental perturbation for these reasons. The formation of silver atoms from $AgNO_3$ was confirmed by X-ray photoelectron spectroscopy (XPS) in Figure 41. The Ag 3d region of the XPS spectrum is illustrated in Figure 41a. Two peaks at 368 and 374 eV could be ascribed to Ag 3d5/2 and Ag 3d3/2, respectively. These values of peaks were in agreement with metallic Ag, further identifying the formation of metallic Ag [188, 189]. Based on these results, pristine CPEDOT NTs and Ag NPs/CPEDOT NTs were successfully fabricated. In order to further confirm the successful fabrication of Ag NPs/CPEDOT NTs, the powder X-ray diffraction (XRD) pattern was carried out, as shown in Figure 42. The characteristic of amorphous CPEDOT peak

was revealed at a 2θ value of approximately 25°.[190] The sharp diffraction peaks at 2θ values of 38.2°, 44.4°, 64.5°, 77.3°, and 81.5° corresponded to Bragg's reflections from the (111), (200), (220), (311) and (222) planes of Ag NPs, respectively, and these data had good agreement with previous report [191].
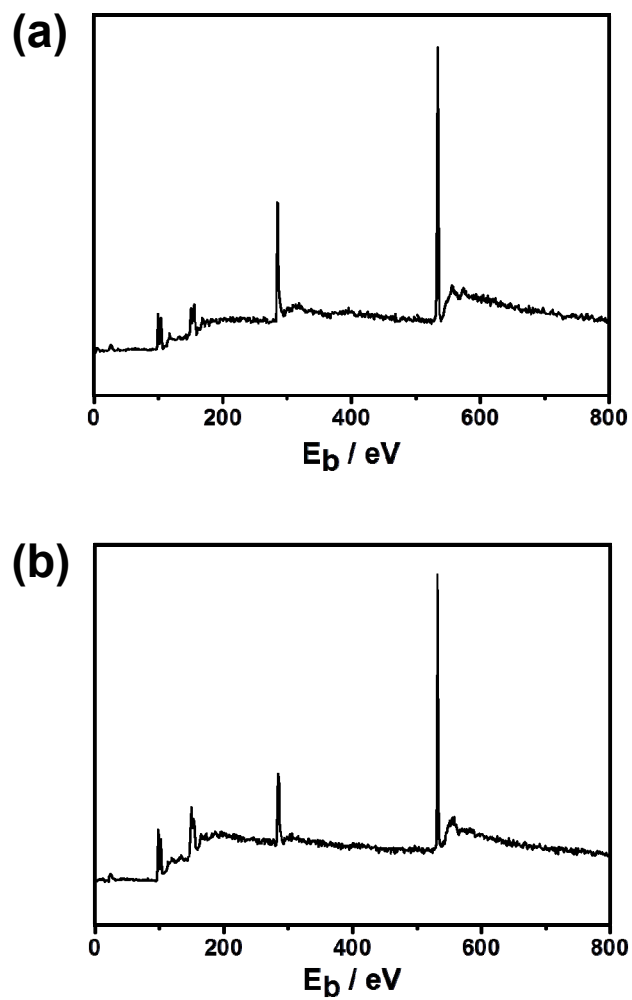
Figure 40. XPS spectra of (a) pristine PEDOT and (b) pristine CPEDOT NTs.
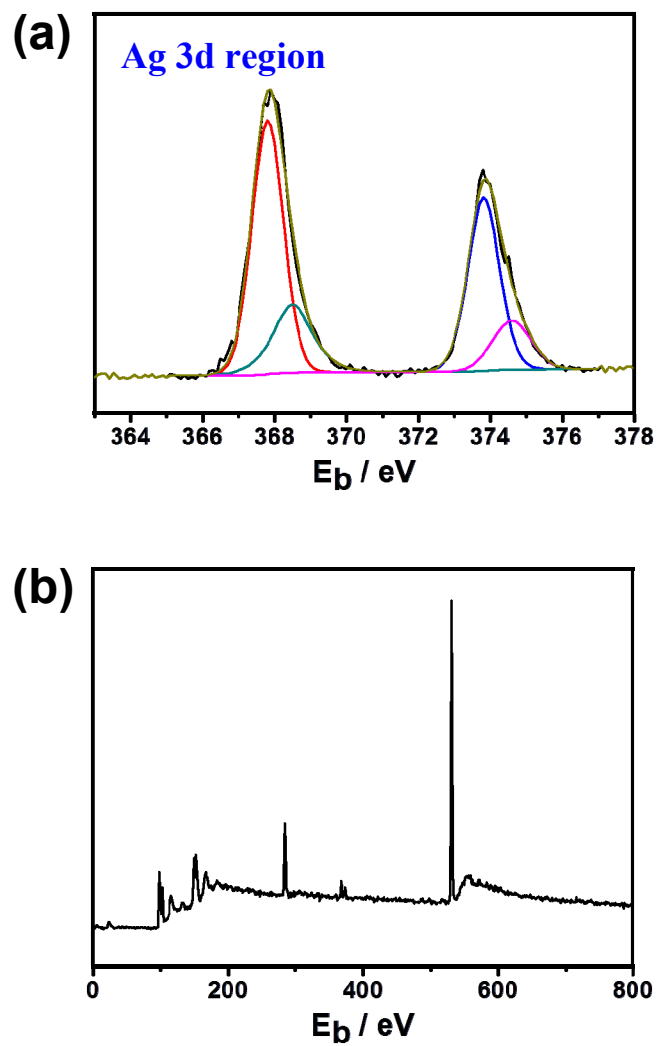
Figure 41. XPS spectra of Ag NPs/CPEDOT NTs prepared with 30% (wt/wt) .
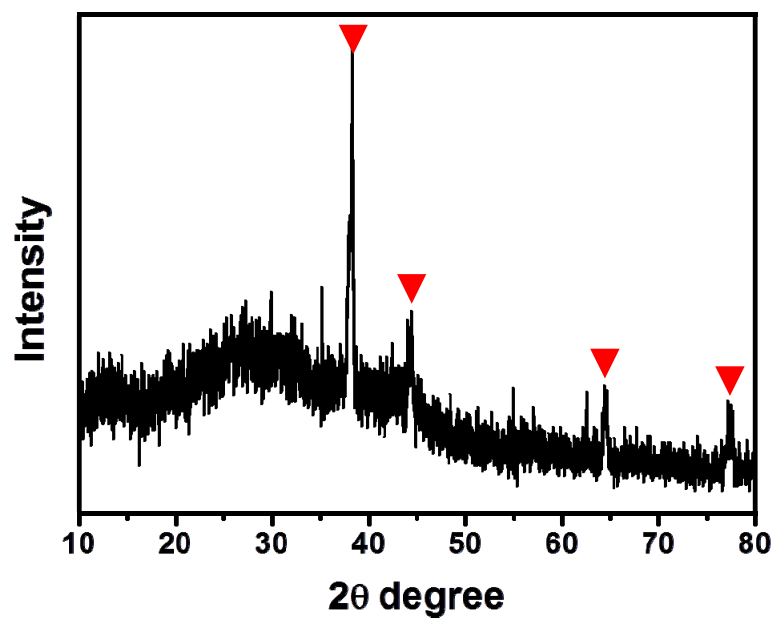
Figure 42. XRD spectrum of Ag NPs/CPEDOT NTs with 30 % (wt/wt) AgNO$_3$ concentration.

The enhanced oxidation level of CPEDOT NT was confirmed by UV-vis spectroscopy in Figure 43. Chemically p-type doping lead to a multistage oxidation reaction of polymer chains, resulting in an improved conductivity of charge carriers including bipolarons or polarons. As seen in Figure 43, the spectra of Ag NPs/CPEDOT NTs with 5, 30 % (wt/wt) clearly indicated the difference of oxidized state between two products. A strong absorption at 600 nm, proved that most of polymer structure is arrived at a bipolaronic state. This specific strong absorption indicated that the formation of a sufficient number of charge carriers [192], which are main reason for improved conductivity of Ag NPs/CPEDOT NTs. Additionally, a strong absorption band was observed in NIR region originating from the presence of the metallic state [193, 194]. It is noteworthy that the adsorption band of Ag NPs/CPEDOT NTs with 30 % (wt/wt) is higher than that of Ag NPs/CPEDOT NTs with 5 % (wt/wt). It is conjectured that the oxidation level of Ag NPs/CPEDOT NTs is highly dependent on the concentration of silver ions because PEDOT can be reduced by silver ions. However, the oxidation level does not remarkably increase despite the population increase of silver ions. This phenomenon means a sufficient number of silver ions were already provided above 30 % (wt/wt) of AgNO$_3$ concentration for CPEDOT. Accordingly, a little increase of oxidation level for Ag NPs/CPEDOT NTs is occurred above 30 % (wt/wt). Therefore, the

optimized concentration of $AgNO_3$ can be determined at 30 % (wt/wt) in our system.

Table 3 demonstrated the conductivities of pristine CPEDOT NTs and Ag NPs/CPEDOT NTs with controlled $AgNO_3$ concentrations by a Keithley 2400 sourcemeter. As shown in Table 3, the conductivities of pristine CPEDOT and Ag NPs/CPEDOT NTs with 5, 30, 40 % (wt/wt) were 2.37×10^{-1}, 5.2×10^{-1}, 1.71×10^{0}, and 1.56×10^{0} S cm^{-1}, respectively. As increasing the population of silver NPs, the conductivities of Ag NPs/CPEDOT NTs increased up to 30 % (wt/wt) of $AgNO_3$. In addition, the surface areas of the pristine CPEDOT NTs and Ag NPs/CPEDOT NTs were measured by Micrometritics ASAP 2000 at 77 K. As shown in Table 3, the surface areas of pristine CPEDOT NTs and Ag NPs/CPEDOT NTs with 5, 30, 40 % (wt/wt) were 35.9, 38.4, 79.7, and 63.1 m^{2}g^{-1}, respectively. The surface areas of each samples are proportional to the increase of silver NPs population. Based on these observations, Ag NPs played an crucial role in optimizing surface areas and the conductivities by controlling their populations. The high surface area of Ag NPs/CPEDOT NTs is mainly attributed to the formation of hybrid nanoparticles consist of Ag NPs.

Judging from these investigations, it could be concluded that Ag NPs/CPEDOT NTs were successfully constructed.
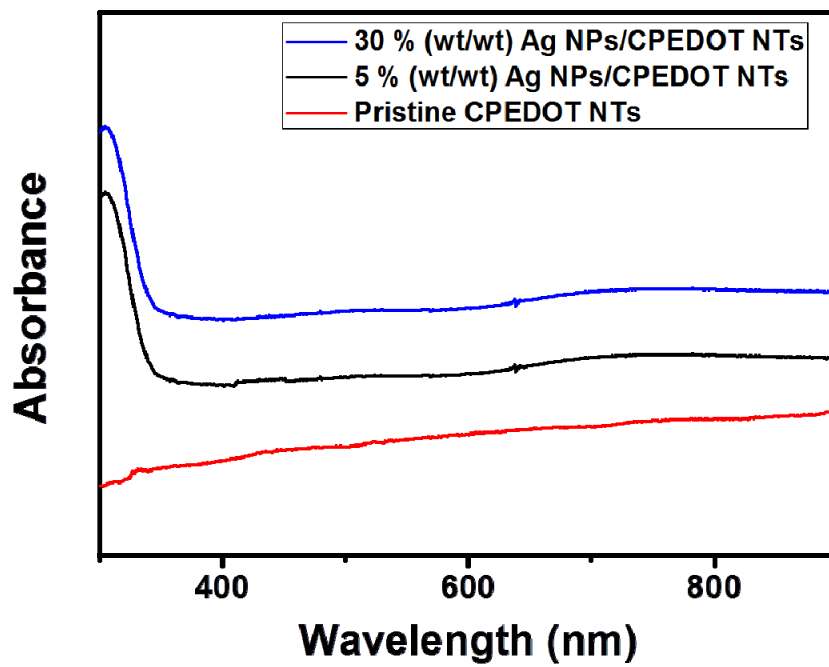
Figure 43. UV-vis spectra of pristine CPEDOT NTs and Ag NPs/CPEDOT NTs prepared with 5 and 30% (wt/wt).

Table 3. The Brunauer-Emmett-Teller (BET) surface areas and conductivities of pristine CPEDOT NTs and Ag NPs/CPEDOT NTs as increasing $AgNO_3$ concentration.

Samples	Surface area (m^2g^{-1})	Conductivity ($S\ cm^{-1}$)
Pristine CPEDOT NTs	35.9	2.37×10^{-1}
5 wt Ag NPs/CPEDOT NTs	38.4	5.2×10^{-1}
30 wt Ag NPs/CPEDOT NTs	79.7	1.71×10^{0}
40 wt Ag NPs/CPEDOT NTs	63.1	1.56×10^{0}

3.3.3. Sensing behaviors of Ag NPs/CPEDOT NTs with various AgNO$_3$ concentrations for H$_2$O$_2$ detection.

The accurate and reliable detection of H$_2$O$_2$ has attracted much attention in nowadays. Additionally, recent researches exhibited that Ag NPs have catalytic activity for H$_2$O$_2$ [195, 196]. Figure 44 exhibited the CVs of Ag NPs/CPEDOT NTs based FET sensor with various concentration of detecting anlaytes. A liquid-ion gate FET geometry was constructed using a phosphate-buffered solution (0.1 M, pH 7.4). It has an advantage in making intimate contacted with the NTs, compared to conventional back gating. As shown in Figure 44, the oxidation and reduction potentials of the Ag NPs/CPEDOT NTs were observed. Figure 45 shows a typical amperometric response of the Ag NPs/CPEDOT NTs based FET sensor on successive injection of various H$_2$O$_2$ concentrations into the stirring PBS (0.1 M, pH 7.4) at an applied potential of -50 mV. The sensor can achieve the maximum steady-state current with a detection limit of 0.87 μM, which was lower than Ag microsphere based biosensor [197]. The relative standard deviation (RSD) for H$_2$O$_2$ sensing was less than 5% for six measurements for the same electrode. It is confirmed that the fast response may be originated from the contribution of Ag NPs onto CPEDOT NTs as surface enhancers and thin walls of CPEDOT NTs. Additionally, this electrochemical sensor also showed good stability for the detection of H$_2$O$_2$.
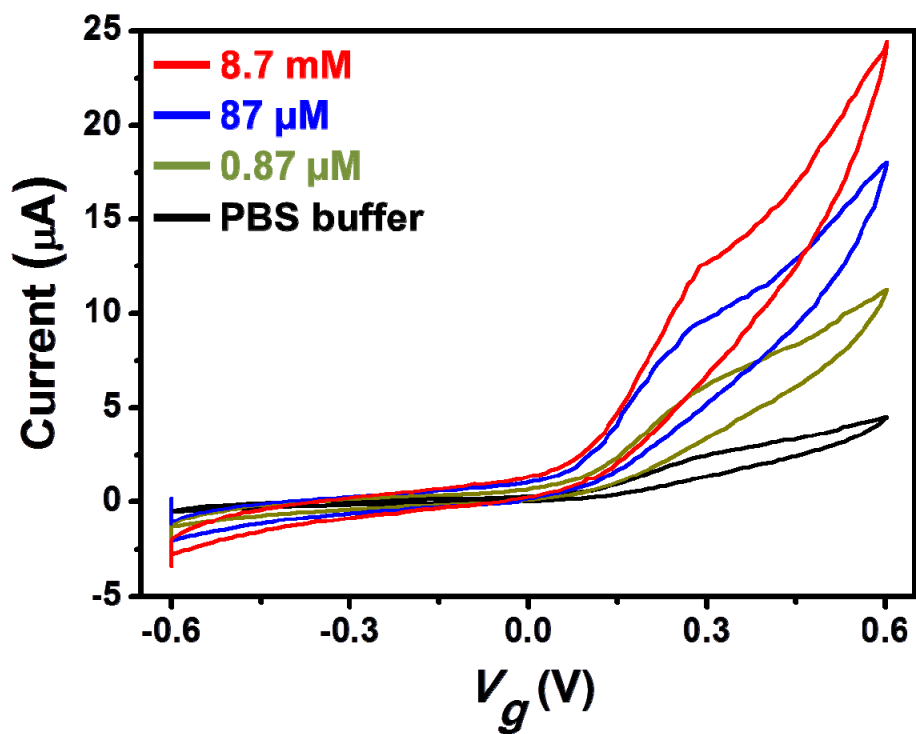
Figure 44. The CVs of Ag NPs/CPEDOT NTs based FET sensor on successive injection of various H_2O_2 concentrations into the stirring 0.1 M PBS (pH 7.4). Applied potential: -50 mV. Inset: plot of H_2O_2 current versus its concentration.
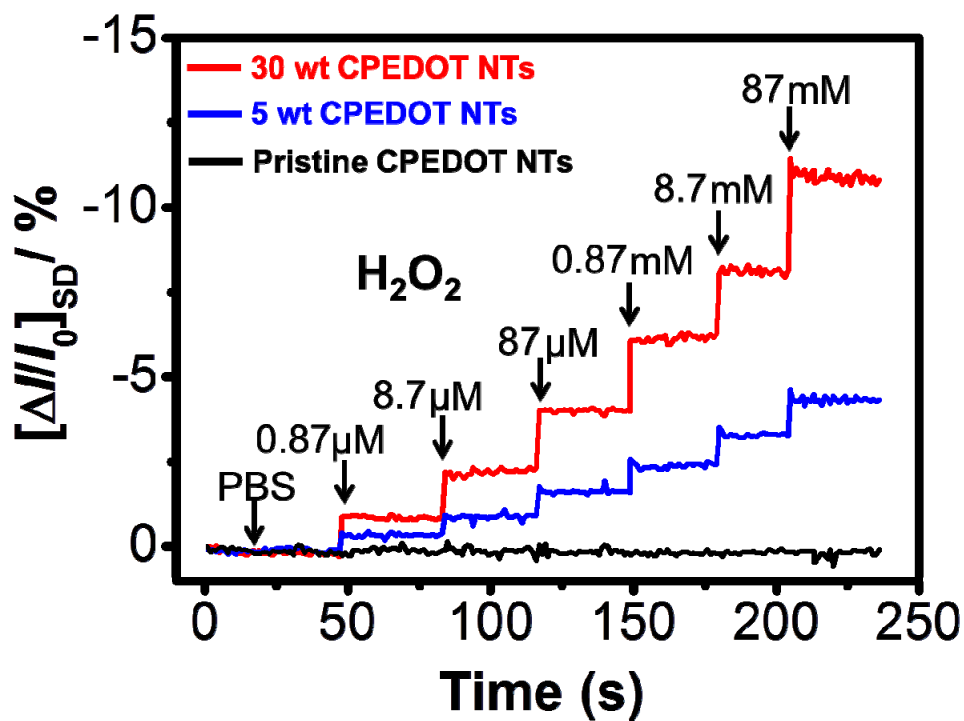
Figure 45. Amperometric response of Ag NPs/CPEDOT NTs based FET sensor on successive injection of various H_2O_2 concentrations into the stirring 0.1 M PBS (pH 7.4). Applied potential: -50 mV. Inset: plot of H_2O_2 current versus its concentration.

3.4. Highly Sensitive and Selective Chemiresistive Sensor based on Multidimensional Polypyrrole (MPPy) Nanotubes.

3.4.1. Fabrication of MPPy nanotubes by vapor deposition polymerization

MPPy nanotubes with nanonodules (ND) and nanowires (NWs) were fabricated for the chemiresistive sensor (Figure 46). Polypyrrole nanotubes with a smooth layer (SM) surface was also prepared as a control. One-dimensional (1D) sensing architectures provide unparalleled advantages in terms of facilitating efficient charge carrier transport induced by molecular recognition events along the long-axis direction.1-D tubular, nanostructure-based sensor devices are more sensitive and selective than nanowires or nanofibers due to their relatively larger surface area.
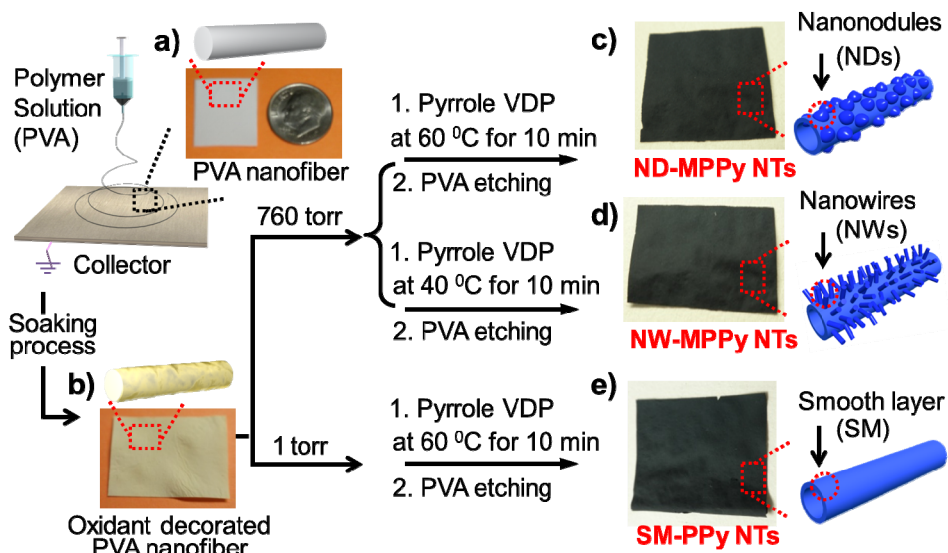
Figure 46. Synthetic protocol of MPPy NTs. (a)–(e) are photo images of the real samples. Each product shows the characterized color changes (a: polyvinyl acetate (PVA) nanofibers with white color, b: oxidant decorated PVA nanofibers with yellow, c and d: ND- and NW-MPPy NTs with black, and e: PPy NTs with black).

3.4.2. Characterization of the MPPy nanotubes.

From a materials perspective, the MPPy NTs were constructed following a coreetching process and were observed by field-emission scanning electron microscopy (FE-SEM) and high-resolution transmission electron microscopy (HR-TEM) (Figure 47). The surface morphologies of the MPPy NTs were tailored with specific structures: SM (Figure 47a), NDs (Figure 47b), and NWs (Figure 47c). Most of these structures had outer diameters of about 100 nm with thin walls approximately 15 nm thick. Stable tubular nanostructures were also identified in HR-TEM micrographs, shown in the insets of Figure 47. The Brunauer–Emmett–Teller (BET) surface area of the nanotubes increased in the following order: SM (28 $m^2\,g^{-1}$) < ND (46 $m^2\,g^{-1}$) < NW (57 $m^2\,g^{-1}$). The NW-MPPy NTs had the most extensive surface area, twice that of conventional SM.
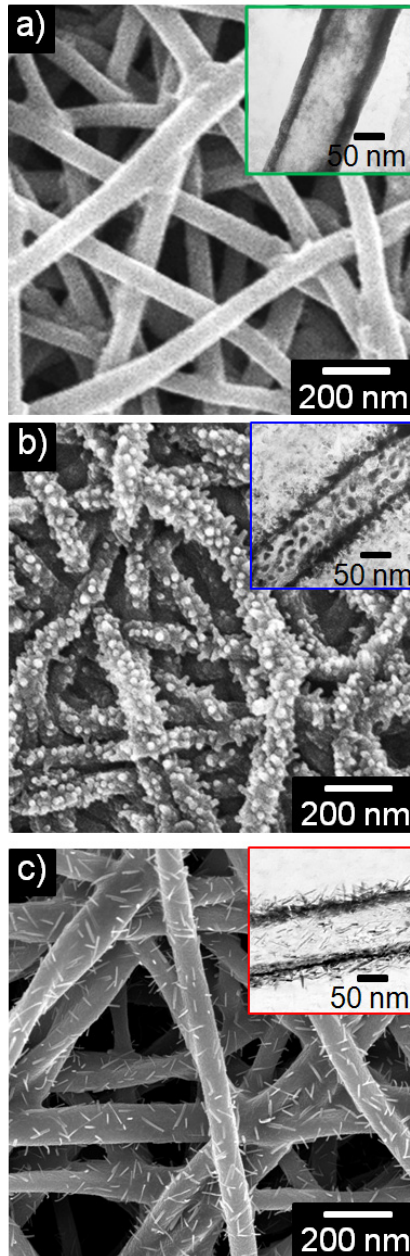
Figure 47. FE-SEM images of MPPy NTs: (a) SMs, (b) NDs and (c) NWs. The insets indicate HR-TEM images.

3.4.3. Real-time responses of chemiresistive sensor based on MPPy nanotubes for volatile organic compounds (VOCs) and toxic gases detection.

Extremely low concentrations (ppb to ppt) of metabolites and/or volatile compounds in exhaled breath can be used as diagnostic markers for diseases.[198, 199] Liver diseases can be diagnosed by elevated levels of ethane (*ca.* 800 pmol L^{-1}) and pentane in breath.[200-202] Hepatic disease, hepatic encephalopathy which is a neuropsychiatric consequence of advanced liver disease, is marked by the presence (*ca.* 238 mg%) of ammonia.[203-205] Various detection methods have been applied to exhaled breath, including gas/liquid chromatography,[206] infrared spectroscopy,[207] mass spectrometry,[208] biological and chemical methods[209] with metallic materials, to meet the expanding need for more sensitive, specific, and non-invasive tests. Although these analyses have individual advantages, their limitations generally include lack of normalization and standardization. Depending on the method, they can also be time consuming and expensive, or may operate at high temperatures. Chemiresistor-based sensors boast several potential advantages, including low power consumption, label-free detection, and highly precise resistance measurements.[210-211] Although significant achievements using several materials, such as metal oxides, semiconductors,

and hybrid nanomaterials, have been made in the development of these sensors, they have been largely limited by poor selectivity and reproducibility, high temperatures, and low sensitivity. Chemiresistive sensor based on multidimensional conducting polymer (CP) nanotubes showed highly sensitive and selective performance. Unique substructures consisting of nanowires (NWs) and nanonodules (NDs) were grown on a polypyrrole surface that had been coated onto a sacrificial nanofiber template by vapor deposition polymerization (VDP). To use MPPy NTs as chemiresistive transistors in a chemical sensor system, the designed poly(dimethylsiloxane) (PDMS) substrate of the device was patterned using typical photolithography processes, where its bottom was punched with holes to effectively retain the flow of the analytes (Figure 48).MPPy NTs were transferred onto a polydimethylsiloxane (PDMS) substrate using a dry-transfer method and the MPPy NTs were integrated into a circuit device fabricated in-house (Figure 49).
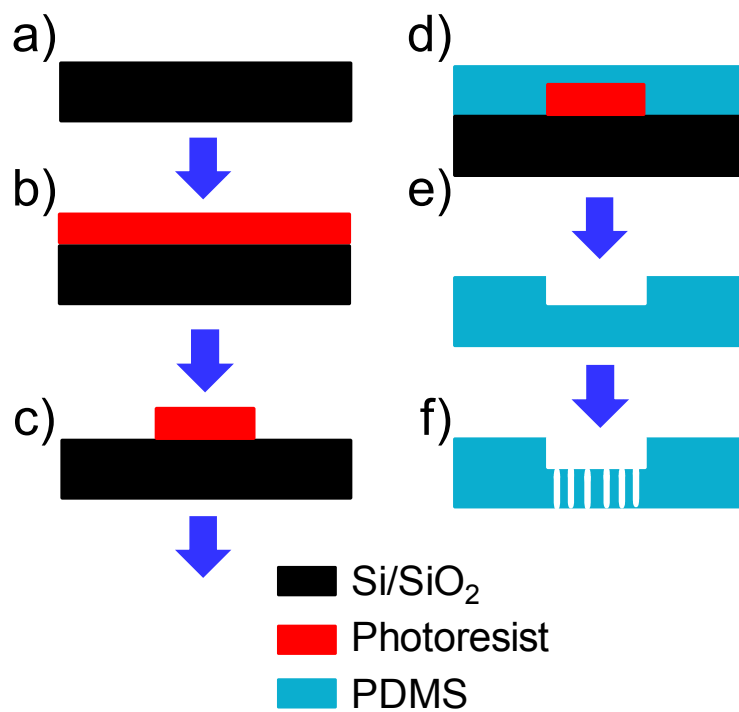
Figure 48. Schematic diagram of the fabrication of PDMS substrate. a) ~ c) Photoresist was deposited on the silicon wafer and patterned by photolithography. d) and e) The fabrication of PDMS sensing substrate. f) The holes are punched for efficient flow of the analytes.
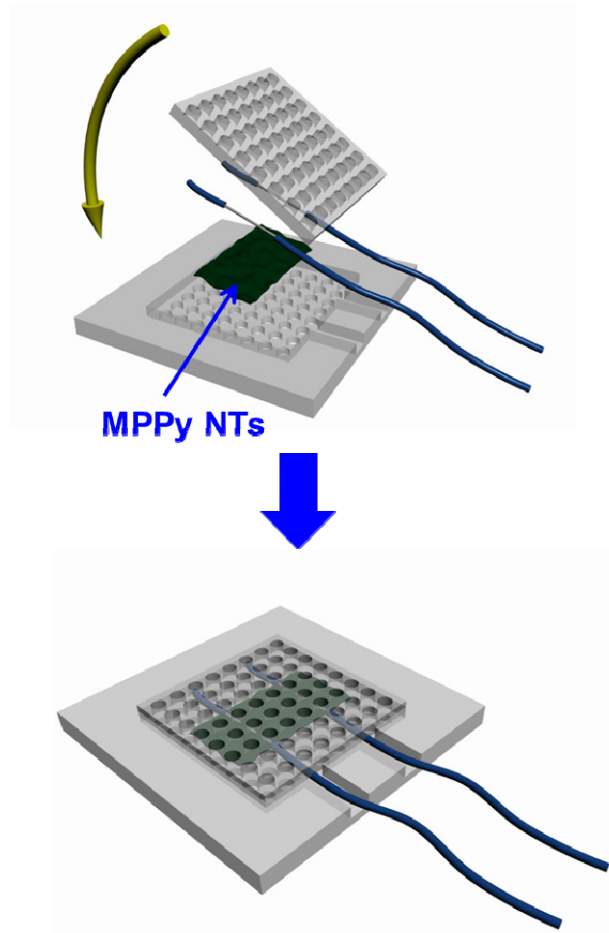
Figure 49. Schematic diagram of the fabrication of home-made circuit device.

The electrical properties of the MPPy NT-integrated chemiresistive sensors (MPNS) were determined by observing their current–voltage characteristics. Figure 50 shows the I–V curves of MPPy NTs on the sensor substrate. All of the MPPy NTs displayed ohmic behaviors in their I–V characteristics, which indicates that the MPPy NTs were in reliable electrical contact with the sensor substrate. Interestingly, the dI/dV values increased slightly in the order SM < ND < NW, due primarily to inter-nanotube contact resistance, which allows for efficient charge transport along the long axis of the MPPy NTs. Accordingly, when the MPPy NTs were assembled between the source and drain electrodes, interactions with the target analyte were indicated by changes in electrical resistance through the MPNS. The resulting multidimensional polypyrrole nanotubes (MPPy NTs) exhibited an enhanced surface-to-volume ratio with an anisotropic tubular structure that provided efficient charge carrier transport along the rotational axis of the nanotube.
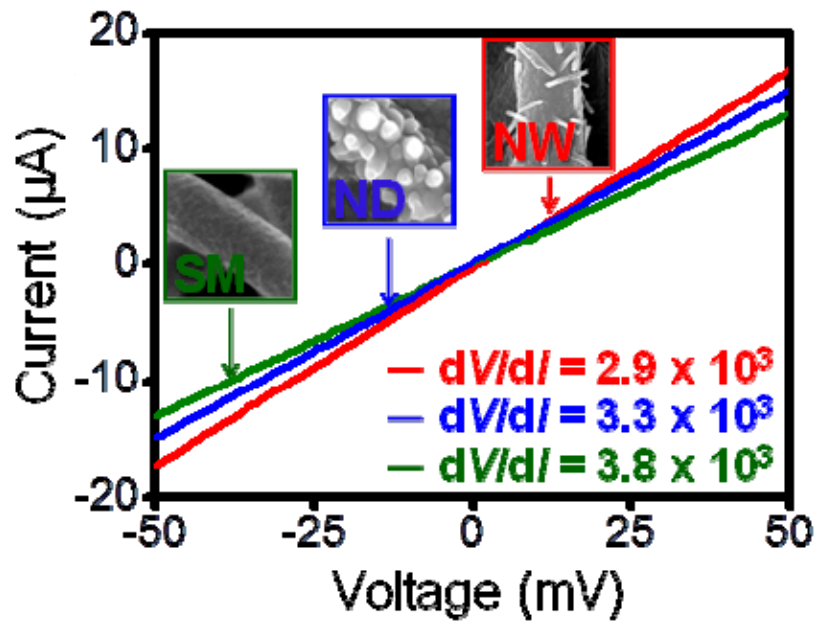
Figure 50. *I–V* characteristics of MPPy NTs integrated in the sensor bstrate (scan rate, 1 mV s^{-1}). The *dV/dI* values indicate the slope of the resistance change.

To confirm their sensing performances, the MPPy NT-integrated chemiresistive sensors (MPNS) was implemented into chemical gas sensing systems. First, since exhaled air contains high levels of water vapor, the environmental stability of the MPNSs was investigated with regard to relative humidity (RH). The electrical resistance of the MPNSs was measured on a probe station in an RH-controlled and temperature-monitored chamber (Figure 51). The significant resistance chances from MPNSs were recorded over 35 % RH. The base line in resistance value was RH dependent at room temperature (RT). The responses to RH increased with the order (NW-MPNS > ND-MPNS > SM-PNS) over ~ 35 % RH (the red area in Figure S4) and the significant response (signal-to-noise: 3.0) was observed from NW-MPNS. These results indicate that the precise measurements of the MPNSs can be produced by controlling the RH (under 35 % RH; the plum area in Figure 51) at RT.
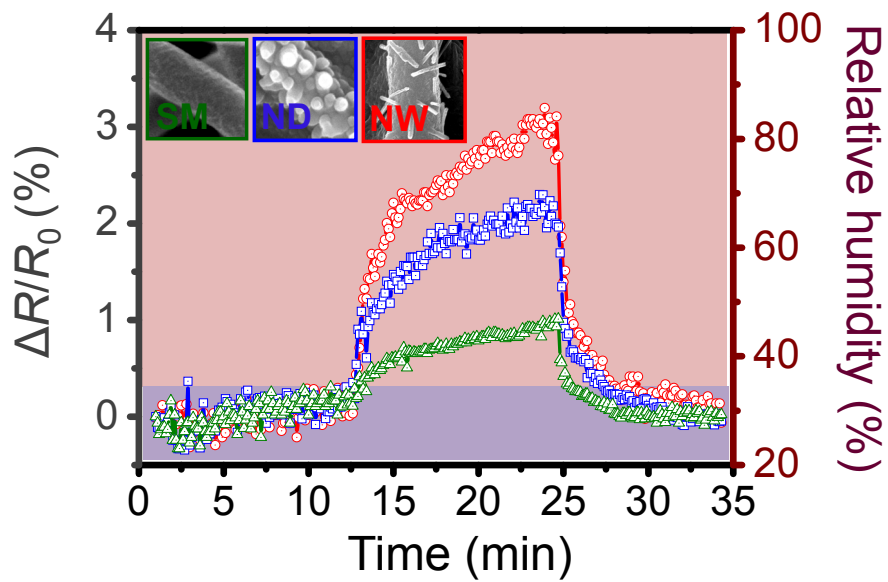
Figure 51. Real-time responses of MPNSs exposure to relative humidity (RH). The significant resistance chances from MPNSs were recorded over 35 % RH.

Under optimized conditions (30–35% RH at RT), changes in resistance were recorded in real time during alternate exposures to ammonia or ethanol vapor and pure N_2 (Figure 52). Exposure to ammonia and ethanol vapors elicited a precipitous rise in the resistance of the MPPy NTs and the signals were saturated continuously. In particular, we presented just a shorter saturation period (*ca.* 10 s) to show the overall response profile at the same cycle because the sensor showed much longer recovery time to ammonia than did ethanol When the analyte flow was replaced with N_2, the resistance recovered to the original level. The signal intensities increased in the order SM < ND < NW. NW- and ND-MPNSs were more sensitive than SM-MPNS. The lowest detection limit of *ca.* 10 ppb gaseous ammonia (signal-to-noise: 3.2) was observed with NW-MPNS. This is approximately two orders of magnitude more sensitive than previously reported NH_3 sensors.[212-217] For ethanol vapor, the NW-MPNS also showed the highest sensitivity with an MDL of *ca.* 1 ppm (signal-to-noise: 3.0). In the previous study, we demonstrated that the charge carrier density was crucial to the sensing performance of devices based on CP nanostructures. In particular, MPPy NTs exhibit a p-type semiconductor characteristic which has holes as charge carriers. The responses from MPNSs can also change the charge carrier density in the MPPy NT backbone. Specifically, the introduction of electron-donating molecules (NH_3) into MPPy

131

NTs reduces the charge carrier density (holes density), resulting in the increment of the electrical resistance. In contrast, analytes which possess electron-withdrawing groups, such as ethanol, methanol, and acetic acid, create new holes in the MPPy NT structure, leading to the opposite result. These charge transfer behaviors allow the MPPy NTs to act as chemiresistors. Compared to conventional gas sensors, the MPNSs had rapid response (less than 1 s) and recovery times (0.01 ppm ammonia: 55–60 s, 1 ppm ethanol: 4–5 s) under various concentrations. In addition, the MPNSs demonstrated excellent reproducibility and reversibility (Figure 52b). Figure 53 shows the changes in resistance over concentration ranges of 0.01 ppm to 100 ppm of ammonia and 1 ppm to 10000 ppm of ethanol vapor.
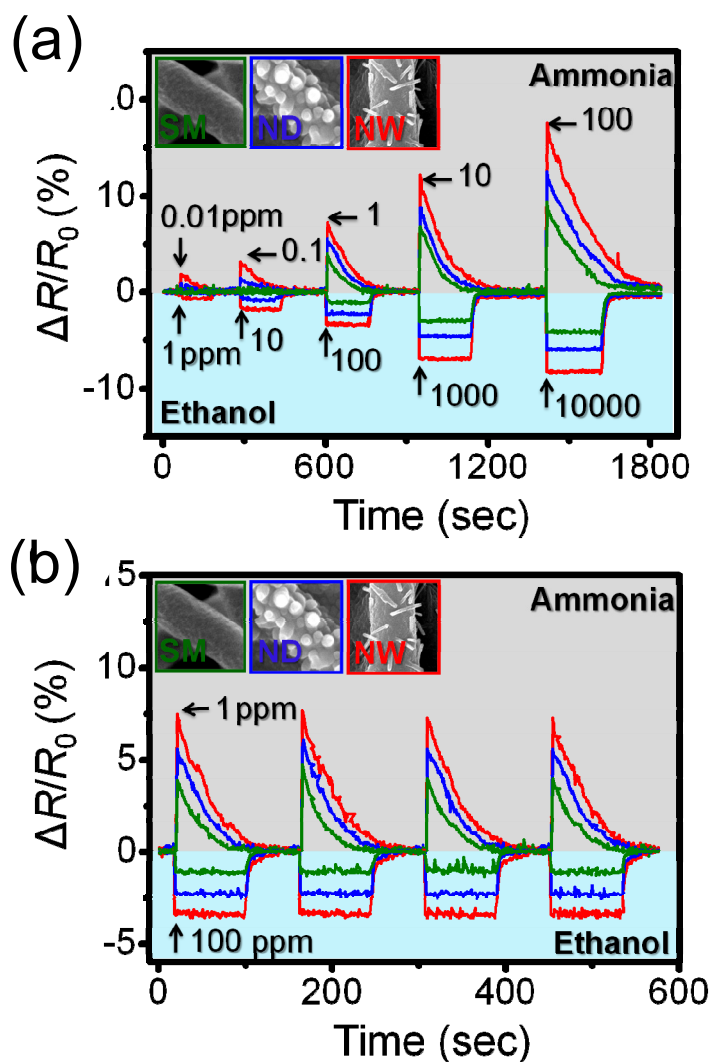
Figure 52. (a) Real-time responses of MPPy NTs upon cyclic exposure to ammonia (0.01 ppm to 100 ppm) and ethanol (1 ppm to 10 000 ppm). (b) Real-time responses of MPPy NTs on periodic exposure to 1 ppm ammonia and 100 ppm ethanol.
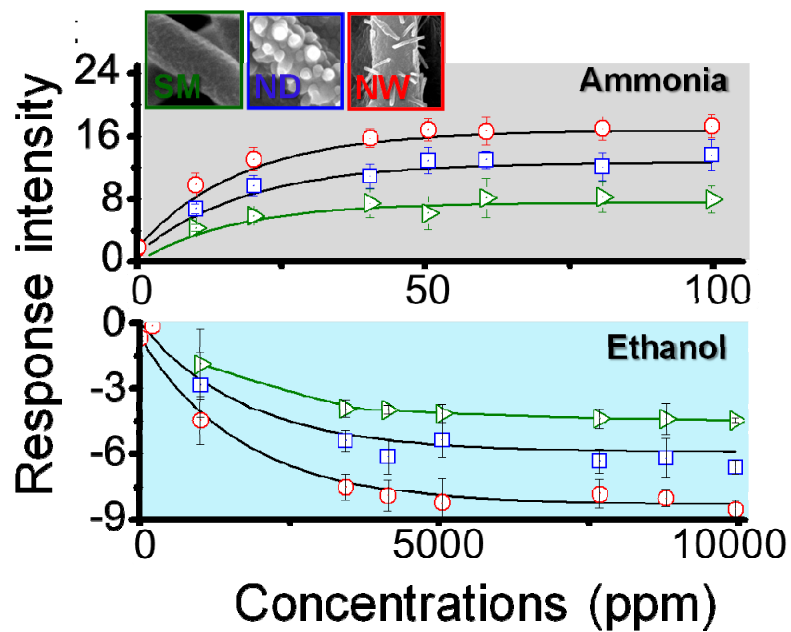
Figure 53. Changes in response intensity of MPPy NTs as a function of ammonia and ethanol vapor concentration: the response intensity was determined as the $\Delta R/Ro$ (%) measured when the saturated value was reached after exposure to gases.

3.4.4. The selectivity test for the several representative VOCs and toxic gases frequently present in human breath.

The MPNS resistance was then monitored in response to several representative volatile organic compounds (VOCs) and toxic gases frequently present in human breath.[218-220] For comparison, the responses of several other sensing materials were simultaneously evaluated. Figure 54 shows the real-time responses of selected sensing materials to 14 gases. Principal components analysis (PCA) was performed on the detection data shown in Figure 54a. Figure 54b shows the characteristic sensitivities of each sensing material for each of the analytes. The accuracy of the simulation results was satisfactory (>99%). Analytes were segregated into separate regions of the PCA plot, with sufficient resolution for the identification of individual analytes. The response of ammonia was particularly differentiable, demonstrating the selective recognition ability of MPPy NTs.
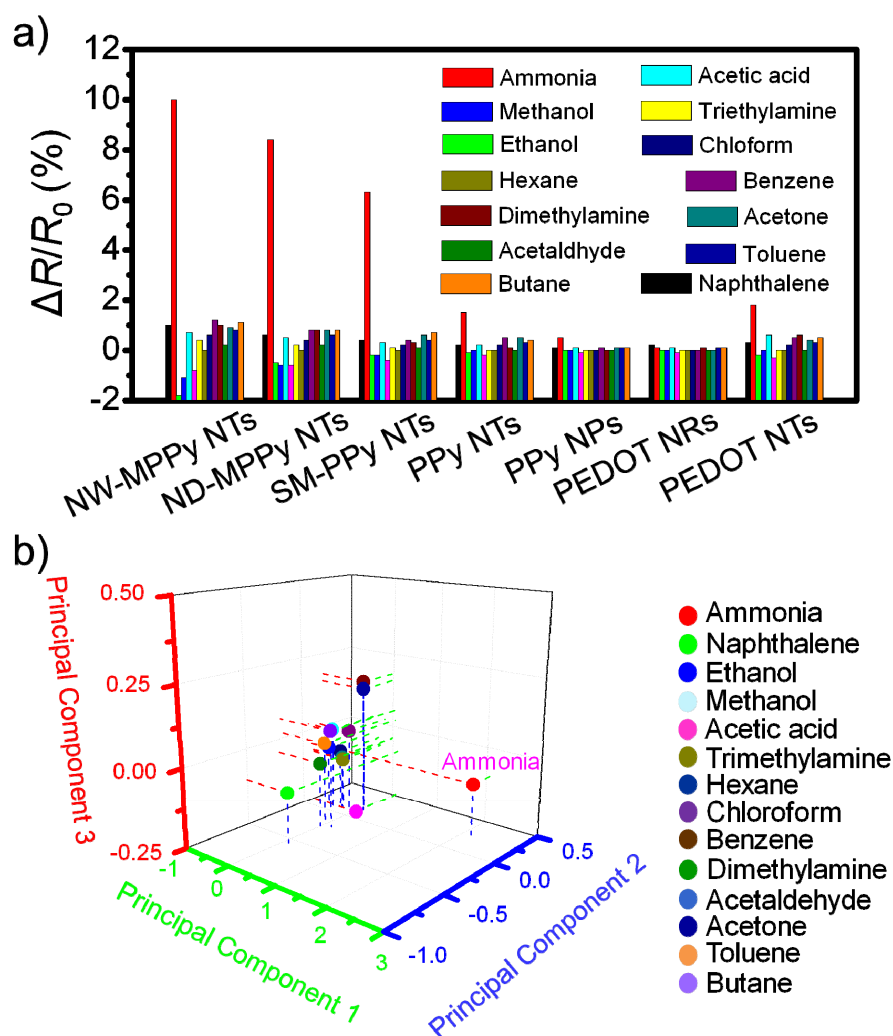
Figure 54. (a) Histogram of sensing performances and (b) principal components analysis (PCA) plot of the dataset of response intensities inputted from six conducting polymer nanomaterials (NW-MPPy NTs, ND-MPPy NTs, SM-PPy NTs, PPy NTs, PPy NPs, PEDOT NRs, and PEDOT NTs) to 14 analytes: each analyte concentration was fixed at around 10 ppm.

136

3.5. Hydrogen Gas Sensor Based On Multidimensional CPPy/CNT Nanohybrids Decorated With Pd NPs Nanohybrids.

3.5.1. Fabrication of ultra-thin skin coating with carboxylated polypyrrole (CPPy) on the CNT by VDP.

Figure 55 represents the synthesis procedure for ultrathin CPPy skin−coated CNT nanohybrids.1-pyrenecarboxylic acid (PCA) was introduced for various functionalities of the CNT surface.[221-227] The PCA attachment on the CNT surface was accomplished via physisorption which is a π−π interaction between the pyrene moiety and the CNT sidewells.[227] Based on PCA research, pristine CNTs were pretreated with PCA in a water–ethanol mixture solution for 24 h to improve the chemical affinity to organic monomer, and then washed with distilled water to remove any remaining unbound PCA. The surface−modified CNTs were obtained by centrifugal precipitation and dried in a vacuum oven at 25 ℃. Next, it was placed into the reactor with FeCl₃, as an oxidant initiator under the vacuum condition. A mixture (0.05 mL) of pyrrole monomer and pyrrole−3−carboxylic acid (P3CA) was injected into the reactor and completely vaporized at 80 ℃. The vaporized monomer was physically adsorbed on the surface of the carboxylic group−modified CNTs, and then the polymerization process was carried out for 24 h. Furthermore, the P3CA functional units were incorporated into the PPy repeating units through

the covalent linkages without any physical degradation of their major physical properties. The ultrathin CPPy skin−coated CNTs were fabricated by venting the reactor to dispose of excess monomer vapor. The final products were washed with ethanol to remove any residual reagents. As shown Figure 56a, the thickness of bare CNT was near 30 nm in diameter. In addition, CPPy was coated on the surface of CNT smoothly with the skin thickness of 5 nm .in diameter (Figure 56b).
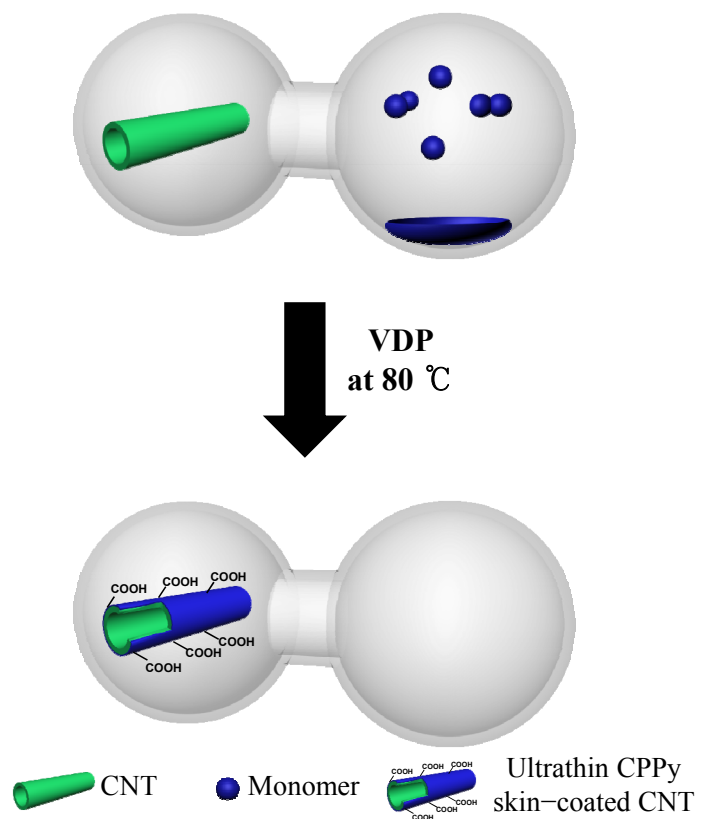
Figure 55. Schematic illustration of synthesis process for ultrathin CPPy skin-coated CNT.
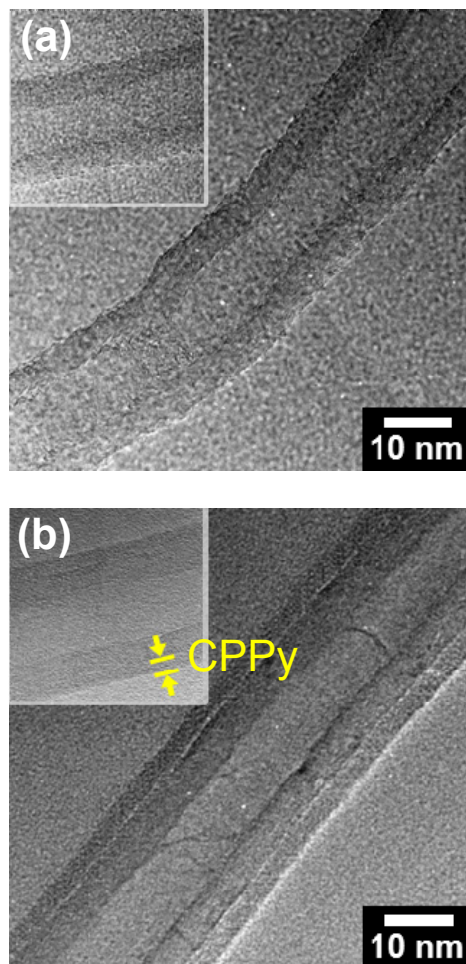
Figure 56. HR-TEM image of (a) bare CNT and (b) ultrathin CPPy skin-coated CNT.

3.5.2. Modification of CPPy/CNT surface with Pd NPs.

A sonochemical reduction method was introduced to attach Pd NPs on the smooth CPPy/CNT surface.[228-230] The carboxylic acid groups of the CPPy were subsequently utilized as the nucleation sites for metal ions. Next, the conversion of Pd(II) cations to Pd(0) was carried out using a sonochemical reduction method with water. When propan-2-ol was added into the Pd^{2+} solution, the rate of reduction was enhanced. However, the Pd NPs were still unstable, leading to precipitation within several hours. During this process, the Pd NPs were retained on the CPPy/CNT surface owing to their strong coordination. Therefore, the carboxyl groups on the CP surface can improve the stability of Pd NPs anchored by the salt reduction method. The diameter of the highly uniform Pd NPs was less than *ca.* 5 nm (Figure 57). The XRD patterns displays the characteristic peaks of Pd at 40.1, 46.7 and 68.2 ^{o} corresponding to the (111), (200), and (220) reflections (Figure 58).10 This indicates that Pd NPs had face-centered cubic lattice structures. Moreover, the Pd NPs had an interplanar spacing of 0.22 nm for the (111) plane, corresponding to Pd, while other fringes showed 0.33 nm for the CNTs.
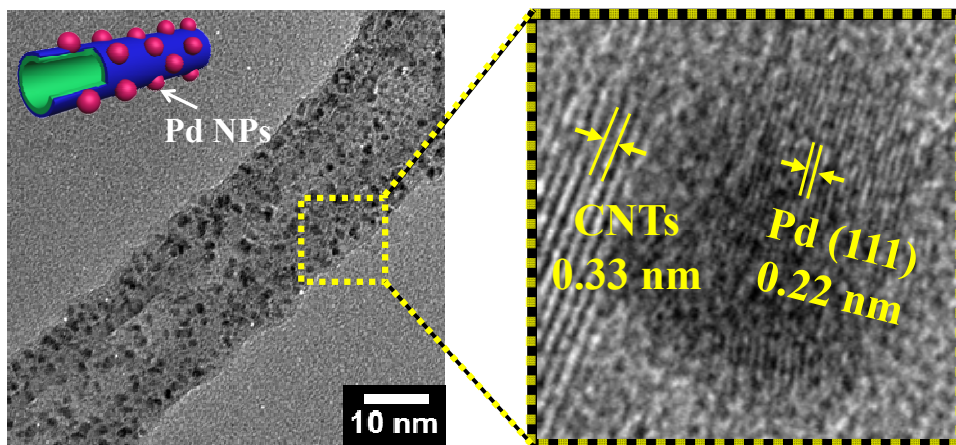
Figure 57. HR-TEM image of Pd NPs–CPPy–CNT nanohybrids (PCCNs).
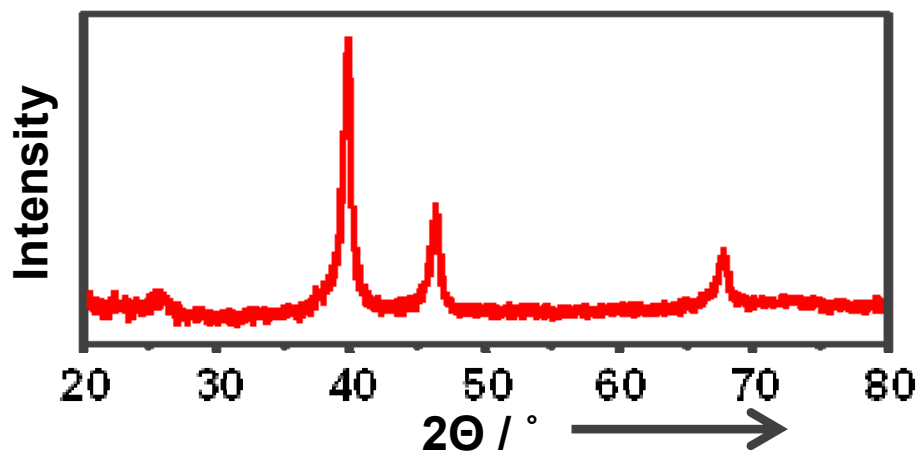
Figure 58. XRD pattern of Pd NPs–CPPy–CNT nanohybrids (PCCNs).

3.5.3. Formation of Pd/CPPy/CNT with different Pd NPs contents as adjusting amounts of functionalized monomer.

To observe the PCCNs, HR-TEM was introduced. Figure 59 shows the nanohybrids with different amounts of functionalized monomer. Three types of ultrathin CPPy skins were constructed to control the amount of Pd NPs; the P3CA to pyrrole molar ratios 1:15 (PCCN1), 1:30 (PCCN2), and 1:60 (PCCN3). The population of Pd NPs on the nanohybrids increased with the order of the increasing PCCN3 < PCCN2 < PCCN1. Excellent size-distribution of the controlled Pd NPs was also confirmed, allowing to the modulation of the hydrogen sensor performance.
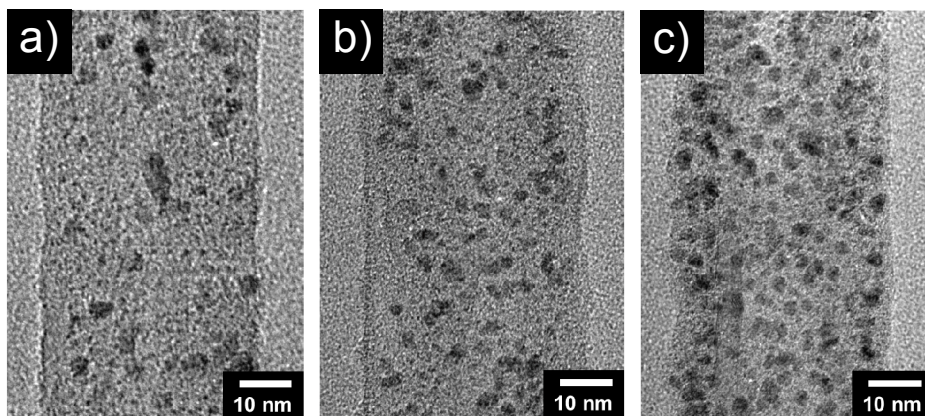
Figure 59. HR-TEM images of the PCCNs with different Pd NPs contents as adjusting amounts of functionalized monomer: a) PCCN3, b) PCCN2, and c) PCCN1.

3.5.4. Electrical Property of Pd/CPPy/CNT based on FET

Figure 60 displays the current–voltage (*I–V*) characteristics of the PCCN1 network constructed by top-contact (W/L =2; L = 50 μm channel length). The *I–V* characteristics are determined primarily by the intrinsic properties of the PCCN1 network. All prepared samples exhibited linear *I–V* curves over the voltage range of −1.0 to +1.0 V, which confirmed the ohmic behavior owing to ultrathin CPPy skin.[241] It can be concluded that the PCCN networks make reliable electrical contact. Therefore, the nanohybrid networks bridged between electrodes, leading to the high-performance chemical sensors in the FET system (Figure 60, inset). To further examine the electrical characteristics of the nanohybrids as FET transducers, Si-back gated FET geometry was constructed using a Si/SiO_2 substrate that provide efficient gate control (Figure 61, inset). Figure 61 illustrates the output curves of the FET sensor based on the PCCN1 at room temperature. The increase in conductance for the p-type FET devices comes from an decrease in negative charge density on the PCCN1 channel. Additionally, the contacts are strongly modulated by the gate when no bottom metal contact is present, allowing for lower sub-threshold swings.[232]
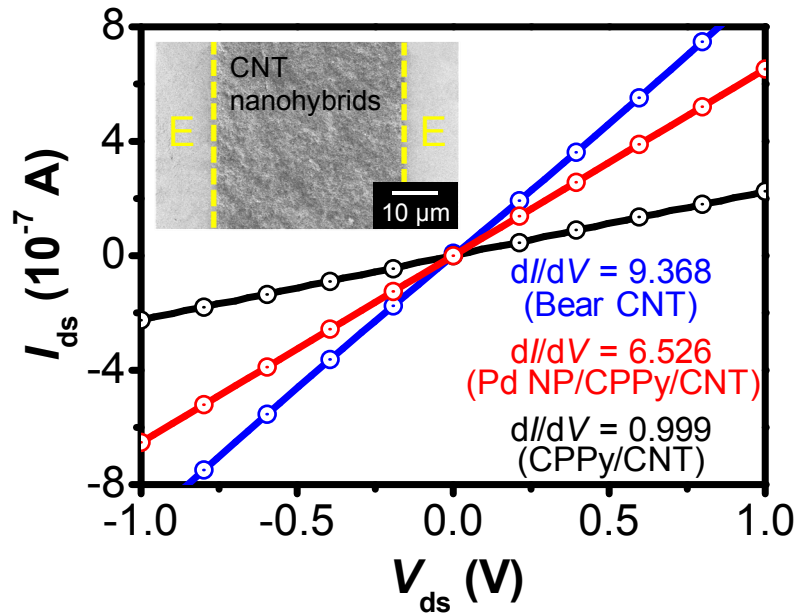
Figure 60. Current-voltage (*I-V*) curves of the PCCN1 on top of the Si/SiO$_2$ substrate. Inset indicates typical FE-SEM images of the nanohybrid on the electrodes (E: electrode).
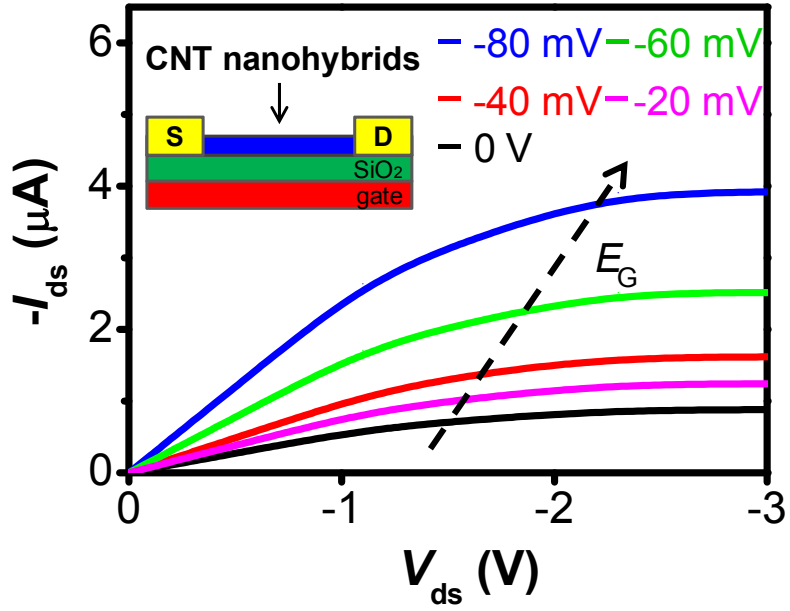
Figure 61. Output characteristics of same device for varying E_G from 0 to -80 mV in -20 mV steps (drain-source voltage sweep rate = 0.5 V^{-1}).

3.5.5. Real-time response of ultra-thin CP layer-coated CNT nanohybrids for H_2 detection.

On the basis of this FET geometry, the sensing capability of the nanohybrid sensors was systematically investigated. The current changes were monitored in real-time responses upon cyclic exposure to H_2 and N_2 streams (Figure 62). The nanohybrid network sensors exhibited very fast responses (<1 s) at room temperature, while there were no significant responses to the CPPy/CNT without Pd NPs. The current values in the FET system decreased by molecule-gating effects induced from the interaction between H_2 and Pd NPs. Moreover, PCCN1 showed the best response to H_2 when compared to that of PCCN2 and PCCN3. Importantly, PCCN1 had the lowest detection limit (1 ppm), which is more than 10-fold more sensitive than that of previous H_2 sensors using CNT/metal hybrids, because atomic hydrogen was dissolved into Pd NPs with high solubility, resulting in decreasing a work function of Pd.[233-239] This interaction generates electron transfer from Pd to CPPy/CNT, which depletes the density of the hole-carriers in the p-type PCCN transducers. Therefore, the conductance decreased upon increasing H_2 concentration.

149
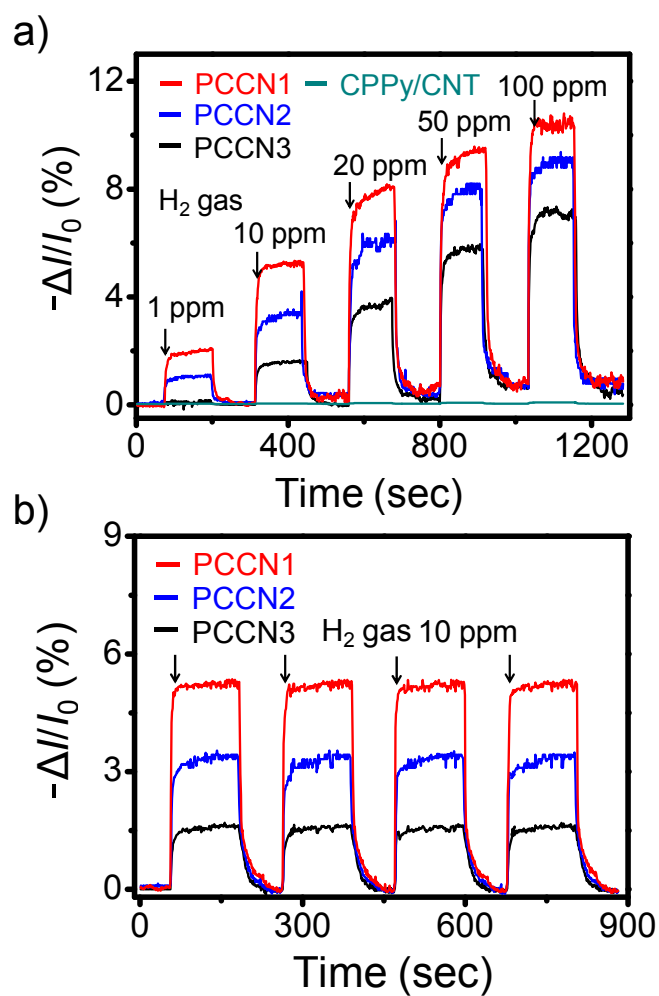
Figure 62. Sensing performance of H_2 sensors based on the nanohybrids. (a) Real-time responses of the nanohybrid sensors (a) upon cyclic exposure to H_2 (1 to 100 ppm, V_{ds} = -50 mV) and (b) on periodic exposure to 10 ppm H_2 ($\Delta I/I_0$ = $(I - I_0)/ I_0$, where I_0 is the initial current and I is the instantaneous current).

4. CONCLUSIONS

The multidimensional conducting polymer nanomaterials were introduced *via* vapor deposition polymerization method (VDP) from the viewpoint of academic research and practical chem/bio sensor applications.

1. Multidimensional conducting polymer nanostructures having nanonodules (NNs) and nanorods (NRs) were successfully fabricated by vapor deposition polymerization (VDP) method with electrospun polymer fibers as template. A new synthetic process allows tailoring the surface morphology of 1D conducting polymer nanomaterials. Novel substructures such as NNs and NRs were grown on the surface of nanofiber template by controlling critical kinetic factors (pressure and temperature) during VDP, leading to the formation of multidimensional polymer nanostructures. To monitor kinetic behavior during the VDP process, the measuring current flow in real time was attempted and a simple kinetic model was developed to estimate the polymerization rate. As a results, the kinetic model showed that the morphology of the polymer deposited on a nanosubstrate strongly depends on the reaction kinetics and slower polymerization kinetics were favorable to the growth of the unique substructures on the nanofiber surface. Moreover, the morphology of deposited polymer nanomaterials

151

was highly affected by substrate curvature as well as synthetic conditions. Because no remarkable nanostructures were generated on bulk flat substrate under the same conditions. Several other potentially critical variables remain, which can affect the formation of the surface nanostructures, such as the reactivity of monomer and the interfacial tensions of monomer and substrate. Thus, there is an ongoing effort to develop a more generalized kinetic model.

2. A The ultrasensitive detection of DMMP, which was the nerve agent stimulant as chemical weapon, was reported by using hydroxylated poly(3,4-ethylenedioxythiophene) (PEDOT) nanotubes (HPNT) with multidimensional nanostructures (NN and NR). The HPNT was successfully fabricated by VDP process at controlled conditions and core-etching process. To detect DMMP, the hydroxyl group was introduced as functional group and produced by injection of the mixed monomer (EDOT/hydroxymethyl EDOT ([EDOT]/[HEDOT] = 3.6/1)) at a controlled temperature and pressure. Tailoring the morphology of materials in the nanometer regime is vital to realizing enhanced device performance due to enhanced surface-to-volume ratio. Especially, the nanotubes are aligned parallel to each other for efficient charge carrier transport. From materials point of view, the aligned HPNT was designed

to achieve highly sensitive and selective sensor performance. Fortunately, integrating the HPNT on flexible PET sensor substrate allowed detection of nerve gas agents at concentrations as low as 10 ppt. The sensing response was reversible and also durable under mechanical deformation. Moreover, the excellent flexibility of HPNT sensor was demonstrated in the wearable system, where the sensor substrate was attached on gloves.

3. Multidimensional CPEDOT NTs decorated with Ag NPs and Fe_3O_4 NPs (Ag /Fe_3O_4 NPs/PEDOT NTs) were fabricated by VDP using AAO as template as just one-pot synthesis. The Ag /Fe_3O_4 NPs/PEDOT NTs were obtained using $Fe(NO_3)_3$ and $AgNO_3$ because PEDOT can reduce metal ions to metal NPs. The diameters of Ag NPs, Fe_3O_4 NPs and CPEDOT NTs were *ca.* 5, 20 and 100 nm, respectively. Ag/Fe_3O_4 NPs/CPEDOT NTs exhibited excellent sensing performances for the detection of H_2O_2 due to a high surface area and conductivity resulting from inorganic nanoparticles. Moreover, the enhanced detection of H_2O_2 is attributed to the thin wall of CPEDOT (*ca.* 10 nm) which can affect the fast diffusion of analytes in and out of materials. The optimized sensing performances were observed at 30 % (wt/wt) of $AgNO_3$ and $Fe(NO_3)_3$ with 4 mM NH_3 solution. It is believed that the highest surface-to-volume ratio has been achieved by Ag and Fe_3O_4 NPs without loss of conductivity. The detection limit of H_2O_2 as

low as 1 nM which was lower than our previous work and Ag/Fe_3O_4 composite based biosensors. This convenient methodology could be expanded to allow the synthesis of nanocomposite between organic and inorganic nanomaterials in applications including bio/chemical sensor, and separation.

4. The chemiresistive sensor composed of multidimensional polypyrrole nanotubes was built on patterned PDMS substrates to discriminate VOCs and toxic gases from human breath. Polypyrrole was grown on the template by VDP process at controlled condition as multidimensional PEDOT. This provides a convenient, safe, and non-invasive method of diagnosing and monitoring diseases. The MPPy NT-integrated chemiresistive sensors (MPNSs) exhibited rapid response and recovery times with highly sensitive and selective responses. The MPNS with nanowires (NWs) was especially sensitive with an MDL of *ca*. 0.01 ppm for ammonia. The sensing materials developed in this study are expected to be relatively portable and inexpensive, allowing their use in high volume applications such as pre-screening events.

5. The ultrathin conducting polymer (CP) skin-coated CNT nanohybrids were successfully fabricated using a simple VDP and sonochemical reduction method. The functionalized CP skin played an important role in the

attachment of stable and uniform Pd NPs and provided efficient charge transfer for enhanced sensing capability. The Pd NPs–CPPy–CNTnanohybrids (PCCN) based-sensors were designed in the FET system to achieve rapid and highly sensitive responses. Three types of ultrathin CPPy skins were constructed to control the amount of Pd NPs; the pyrrole-3-carboxylic acid (P3CA) to pyrrole molar ratios 1 : 15 (PCCN1), 1 : 30 (PCCN2), and 1 : 60 (PCCN3). Fortunately, the PCCN1 sensor allowed the detection of H_2 at concentrations as low as 1 ppm. Excellent reproducible and reversible responses from PCCN sensors were also demonstrated.

In summary, multidimensional conducting polymer (CP) nanomaterials with nanostructures on the template have been fabricated by vapor deposition polymerization and hard template method. These approaches were possible to control the morphology of the CP nanomaterials at controlled kinetic conditions. Accordingly, it provided high surface area and showed excellent the sensing performances. These findings may not only provide new possibilities for tailoring material properties but also offer an essential understanding of the parameters determining performance of devices based on conducting polymer nanomaterials. The multidimensional CP nanomaterials have been successfully used as versatile signal channel of transducers in sensor

platform, suggesting that these nanomaterials may be potentially very useful in many new types of applications related to electronic/optoelectronic devices, conductive nanocomposites, actuators, catalytic supports, energy storage/conversion, and drug delivery systems.

REFERENCES

[1]   S. Sun, C. B. Murray, D. Weller, L. Folks, A. Moser, *Science* **2000**, *287*, 1989.

[2]   J. Wang, M. S. Gudiksen, X. Duan, Y.Cui, C. M. Lieber, *Science* **2001**, *293*, 1455.

[3]   R. P. Ortiz, A. Facchetti, T. J. Marks, *Chem. Rev*. **2010**, *110*, 205.

[4]   A. T. Bell, *Science* **2003**, *299*, 1688.

[5]   Y. C. Cao, R. Jin, C. A. Mirkin, *Science* **2002**, *297*, 1536.

[6]   M. Bruchez, Jr., M. Moronne, P. Gin, S.Weiss, A. P. Alivisatos , *Science* **1998**, *281*, 2013.

[7]   R. J. Wojtecki, M. A. Meador, S. J. Rowan, *Nat. Mater*. **2011**, *10*, 14.

[8]   X. Gao, Y. Cui, R. M. Levenson, L.W. K. Chung, S. Nie, *Nat. Biotechnol.* **2004**, *22*, 969.

[9]   H. Yoon, J. Jang, *Adv. Funct. Mater*. **2009**, *19*, 1567.

[10]   A. Nel, T. Xia, L. Madler, N. Li, *Science* **2006**, *311*, 622.

[11]   P. Rivera Gil, G. Oberdorster, A. Elder, V. Puntes, W. J. Parak, *ACS Nano* **2010**, *4*, 5227.

[12]   S. George, S. Pokhrel, T. Xia, B. Gilbert., Z. Ji, M. Schowalter, A. Rosenauer, A. Nel, *ACS nano* **2010**, *4*, 15.

[13]   A. Petushkov, J. Intra, J. B. Graham, S.C. Larsen, A. K. Salem, *Chem. Res. Toxicol.* **2009**, *22*, 1359.

[14]   J. Jang, *Adv.Polym. Sci*. **2006**, *199*, 189.

[15]   Q. Zhao, A. Boxman, U. Chowdhry, *J. Nanopart. Res*. **2003**, *5*, 567.

[16]   M. Lazzari, *Adv. Mater*. **2003**, *15*, 1583.

[17]   C. N. R. Rao, A. K. Chetham, *J. Mater. Chem.* **2001**, *11*, 2887.

[18]   H. Yoon, S. H. Lee, O. S. Kwon H. S. Song, E. H. Oh. T. H. Park, J. Jang, *Angew, Chem. Int. Ed*. **2009**, *48*, 2755.

[19]   M. M.Ostwal, B. Qi, J. Pellegrino, A.G. Fadeev, I. D. Norris, T. T. Tsotsis, M. Sahimi, B.R. Mattes, *Ind. Eng. Chem. Res*. **2006**, *45*, 6021.

[20]   J. Jang. J. H. Oh., GD. Stucky. *Angew. Chem. Int. Ed*. **2002**, *41*, 4016.

[21]   O.S Kwon, S. J. Park, J. Jang. *Biomaterials* **2010**, *31*, 4740.

[22]   J. E. Collazos-Castro, J. L. Polo., G.R. Hernandez-Labrado, V. Padial-Canete, C. Garcia-Rama. *Biomaterials* **2010**, *31*, 9244.

[23]   A. J. Heeger, [*Handbook of Conducting Polymers*] Marcel Dekker, N. Y., Ed. by T.A Skotheim, **1986**, *1*, 4.

[24]   G. H. Gorman and R. H. Grubbs, [*Conjugated Polymers*] Kluwer Acedemic Publishers, Ed. by J. L. Bredas and R. Silbey, **1991**, 3.

[25]   K. Lota, V. Khomenko, E. Frackowiak, *J. Phys. Chem. Solids*. **2004**, *65*, 295.

[26]   S. Suematsu, U. Oura, H. Tsujimoto, H. Kanno, K. Naoi, *Electrochim, Acta*. **2000**, *45*, 3813.

[27]   H. Pielartzik, J. R. Reynolds, *Adv. Mater*. **2002**, *12*, 481.

[28]   S. Kirkchmeyer, K. Reuter, *J. Mater. Chem*. **2005**, *15*, 2077.

[29]   B. L. Groenendaal, F. Jonas, D. Freitag, H. Pielartzik, J. R. Reynold, *Adv. Mater*. **2000**, *12*, 481.

[30] Y. M. Shi, S.-C. Luo, W. J. Fang, K. K. Zhang, E. Mohamed Ali, F. Y. C. Boey, J. Y. Ying, J. L. Wang, H.-h. Yu, L. J. Li, *Org. Electron*. **2008**, *9*, 859.

[31] S.-C. Luo, H.-h. Yu, A. C. A. Wan, Y. Han, J. Y. Ying, *Small* **2008**, *4*, 2051.

[32] S.-C. Luo, E. Mohamed Ali, N. C. Tansil, H.-h. Yu, S. Gao, E. A. B. Kantchev, J. Y. Ying, *Langmuir* **2008**, *24*, 8071.

[33] A. Angeli, *Gazz. Chim. Ital.* **1916**, *46*, 279.

[34] M. G. Kanaizidis, Chemical & Engineering News, December, 36.

[35] J. C. Scott, P. Pfluger, M. T. Kruounbi, G. B. Street, *Phys. Rev. B*. **1983**, *28*, 2140.

[36] J. L. Bredas, G. B. Street, *Acc.Chem. Res*. **1985**, *18*, 309.

[37] J. L. Breda, J. C. Scott, K. Yakushi, G. B. Street, *Phys. Rev. B*. **1984,** *30*, 1023.

[38] S. Kim, W. -K. Oh. Y. S. Jeong, J.-Y. Hong, B.-R. Cho, J.-S. Hahn, J. Jang, *Biomaterials* **2011**, *32*, 2342.

[39] K. C. Krogman, J. L. Lowery, N. S. Zacharia, G. C. Rutledge, P. T. Hammond, *Nat. Mater*. **2009**, *8*, 512.

[40] W. Baaziz, S. Begin-Colin, B. P. Pichon, I. Florea, O. Ersen, O. Zafeiratos, R. Barbosa, D. Begin, C. Pham-Huu, *Chem. Mater*. **2012**, *24*, 1549.

[41] Z. Wang, A. Z. Skirtach, Y. Xie, M. Liu, H. Mo⋅ hwald, C. Gao, *Chem. Mater*. **2011**, *23*, 4741.

[42] H. Zhou, W. -P. Zhou, R. R. Adzic, S. S. Wong, *J. Phys. Chem. C.* **2009**, *113*, 5460.

[43] J. W. Lee, A. S. Hall, J. -D. Kim, T. E. Mallouk, *Chem. Mater.* **2012**, *24*, 1158.

[44] P. Lu, A. V. Walker, *ACS Nano* **2009**, *3*, 370.

[45] B. Shukla, T. Saito, S. Ohmori, M. Koshi, M. Yumura, S. Iijima, *Chem. Mater.* **2011**, *23*, 1636.

[46] J. Luo, L. Ma, T. He, C. F. Ng, S. Wang, H. Sun, H. J. Fan, *J. Phys. Chem. C.* **2012**, *116*, 11956.

[47] P. Y. Keng, M. M. Bull, I. -B. Shim, K. G. Nebesny, N. R. Armstrong, Y. Sung, K. Char, Pyun, *J. Chem. Mater.* **2011**, *23*, 1120.

[48] C. M. Cobley, J. Chen, E. C. Cho, L. V. Wang, Y. Xia, *Chem. Soc. Rev.* **2011**, *40*, 44.

[49] H. D. Tran, D. Li, R. B. Kaner, *Adv. Mater.* **2009**, *21*, 1487.

[50] H. -W. Park, T. Kim, J. Huh, M. Kang, J. E. Lee, H. Yoon, *ACS Nano* **2012**, *6*, 7624.

[51] M. Chang, T. Kim, H. -W. Park, M. Kang, E. Reichmanis, H. Yoon, *ACS Appl. Mater. Interfaces.* **2012**, *4*, 4357.

[52] J. Huang, S. Virji, B. Weiller, R. B. Kaner, *J. AM. Chem. Soc.* **2003**, *125*, 314.

[53] S. J. Choi, S. M. Park, *Adv. Mater.* **2000**, *12*, 1547

[54] Y. Yang, M. Wan, *J. Mater. Chem.* **2001**, *11*, 2022

[55] F. S. Bates, *Science* **1991**, *251*, 898

[56]   D. Zhao, J. Feng, Q. Huo, N. Melosh, G. H. Fredrickson, B. F. Chmelka, G. D. Stucky, Science **1998**, *279*, 548

[57]   J. Raez, R. Barjovanu, J. A. Massey, M. A. Winnik, I. Manners, *Angew. Chem. Int. Ed.* **2000**, *39*, 3862

[58]   P. Leclere, A. Calderone, D. Marsitzky, V. Francke, Y. Geerts, K. Mullen, J. L. Bredas, R. Lazaronic, *Adv. Mater.* **2000**, *12*, 10742

[59]   I. Mannes, *Chem. Commun.* **1999**, *857,* 8.

[60]   Z. Wei, Z. Zhang, M. Wan, *Langmuir* **2002**, *18*, 917.

[61]   H. Qui, M. Wan, *J. Polym. Sci. Part. A. Polym. Chem.* **2001**, *39*, 3485

[62]   M. S. Spector, R. R. Price, J. M. Schnur, *Adv. Mater.* **1999**, *11*, 337.

[63]   T. M. Yao, N. E. Kim, Y. Xia, G. M. Whitesides, I. A. Aksay, *Nature* **1997**, *390*, 674.

[64]   C. T. Kresge, M. E. Leonowicz, W. J. Roth, J. C. Vartuli, J. S. Beck, *Nature* **1992**, *359*, 710.

[65]   J. M. Schnur, *Science* **1993**, *262*, 1669

[66]   D. M. Antonelli, *Adv. Mater.* **1999**, *11*, 487

[67]   M. Ghadiri, J. R. Granja, L. Buehler, *Nature* **1994**, *369*, 301

[68]   P. A. Lovell PA, M. S. Al-Aasser, [*Emulsion polymerization and emulsion polymers*]Wiley, New York, **1997**, 700.

[69]   M. Antonietti, R. Basten, S. Lohmann, *Macromol. Chem. Phys.* **1995**, *196*, 441.

[70]   F. J. Schork, G. W. Poehlein, S. Wang, J. Reimers, J. Rodrigues, C. Samer, *Colloids. Surf. A.* **1999**, *153*, 39.

[71]   C. S. Chern, T. J. Chen, Y. C. Liou, *Polymer* **1998**, *39*, 3767.

[72]   K. Landfester, *Macromol. Symp.* **2000**, *150*, 171.

[73]   P. J. Blythe, E. D. Sudol, M. S. El-Aasser, *Macromol. Symp.* **2000**, *150*, 179.

[74]   J. Jang, J. Bae, *Angew. Chem. Int. Ed*. **2004**, *43*, 3803.

[75]   U. Yildiz, K. Landfester, M. Antomietti, *Macromol. Chem. Phys.* **2003**, *204*, 1966.

[76]   G. Liu, X. Yan, S. Duncan, *Macromolecules* **2002**, *35*, 9783.

[77]   C. S. Yang, D. Awschalom, G. D. Stucky, *Chem. Mater*. **2002**, *14*, 1277.

[78]   M. Kahlweit, *Angew. Chem. Int. Ed.* **1985**, *24*, 654.

[79]   B. J. Holliday, C. A. Mirkin, *Angew. Chem. Int. Ed.* **2001**, *40*, 2022.

[80]   F. M. Pavel, R. A. Mackay, *Langmuir* **2000**, *6*, 8568.

[81]   J. Jang, J. H. Oh, G. D. Stucky, *Angew. Chem. Int. Ed.* **2002**, *41*, 4016.

[82]   F. Reynolds, K. Jun, Y. Li, *Macromolecules* **2001**, *34*, 167.

[83]   J. Jang, K. Lee, *Chem. Commun*. **2002**, 1098

[84]   F. Caruso, *Adv. Mater.* **2001**, *13*, 11.

[85]   J. Jang, H. Ha, *Chem. Mater.* **2003**, *15*, 2109.

[86]   L. Zhang, M. Wan, *Adv. Funct. Mater.* **2003**, *13*, 815

[87]   X. Duan, Y. Huang, Y. Cui, J. Wang, C. M. Lieber, *Nature* **2001**, *409*, 66.

[88]   J. Jang, H. Yoon, *Chem Commun.* **2003**, 720.

[89]   K. Landfester, N. Bechthold, F. Tiarks, M. Autonietti, *Macromolecules* **1999**, *32*, 5222.

[90]   K. Landfester, *Adv. Mater.* **1999**, *13*, 765.

[91]   C. R. Martin, *Science* **1994**, *266*, 1961.

[92]   R. Gangopadhyay, Encyclo. *Nanosci. Nanotech*. **2004**, *2*, 105.

[93]   C. R. Martin. *Acc. Chem. Res*. **1995**, *28*, 61.

[94]   M. Wan, *Encyclo. Nanosci. Nanotech*. **2004**, *2*, 153.

[95]   R. Parthasarathy, C. R. Martin, *Nature* **1994**,*369*, 298

[96]   C. R. Martin, R. Parthasarathy, V. Menon, *Synth. Met.* **1993**, *55*, 1165.

[97]   J. Lei, Z. Cai, C. R. Martin, *Synth. Met.* **1992**, *46*, 53.

[98]   R. Parthasarathy, C. R. Martin, *Chem. Mater.* **1994**, *6*, 1627.

[99]   V. P. Menon, J. Lei, C. R. Martin, *Chem. Mater.* **1996**, *8*, 2382.

[100] G. Omerz-Kaifer, P. A. Reddy, C. D Gutsche, L. Echegoyen, *J. Am. Chem. Soc.* **1998**, *120*, 2486.

[101] S. M. Marinakos, L. C. Brouseau, A. Jones, D. L. Feldheim, *Chem. Mater.* **1998**, *10*, 1214

[102] J. Jang, B. Lim, J. Lee, T. Hyeon, *Chem. Commun.* **2001**, 83

[103] B. H. Hong, J. T. Lee, C. W. Lee, J. C. Kim, S. C. Bae, K. S. Kim, *J. Am. Chem. Soc*. **2001**, *12*, 10748.

[104] M. Delvaux, J. Duchet, P. Y. Stavaux, R. Legras, S. Demoustier-Champagne, *Synth. Met*. **2000**, *113*, 275.

[105] J. H. Chem, Z. P. Huang, D. Z. Wang, S. X. Yang, W. Z. Li, J. G. Wen, Z. F. Ren, *Synth. Met.,* **2002**, *125*, 289.

[106] J. Jang, J. H. Oh, *Chem. Commun.* **2004**, 882.

[107] H. R. Allcock, *Adv. Mater.* **1994**, *6*, 106

[108] R. Gangopadhyay, A. De, *Chem. Mater*. **2000**, *12*, 608.

[109] M. G. Kanatzidis, C. G. Wu, H. O. Marcy, C. R. Kannewurf, *J. Am. Chem. Soc.* **1989**, *111*, 4139.

[110] S. N. Wang, Q. S. Gao, Y. H. Zhang, Y. H. J. Gao, X. H. Sun, Y. Tang, *Chem.Eur. J.* **2011**, *17*, 1465.

[111] M. Sindoro, Y. H. Feng, S. X. Xing, H. Li, J. Xu, H. L. Hu, C. C. Liu, Y. W. Wang, H. Zhang, Z. X. Shen, H. Y. Chen, *Angew. Chem. Int. Ed*. **2011**, *50,* 9898

[112] S. H. Im, U. Y. Jeong, Y. N. Xia, *Nat. Mater.* **2005**, *4,* 671.

[113] W. Yin, M. Z. Yates, *Langmuir* **2008**, *24,* 701.

[114] J. Cho, K. -H. Shin, *Thin Solid Films* **2010**, *518*, 5066.

[115] B. H. Lee, B. Yoon, A. I. Abdulagatov, R. A. Hall, S. M. George, *Adv. Funct. Mater.* **2013**, *23*, 532

[116] J. T. McCann, B. Lim, R. Ostermann, M. Rycenga, M. Marquez, and Y. Xia, *Nano Lett*. **2007**, *7*, 2470

[117] J. P. F. Lagerwall, J. T. McCann, E. Formo, G. Scalia, and Y. Xia, *Chem. Commun*. **2008**, 5420

[118] Y. Zhu, L. Feng, F. Xia, J. Zhai, M. X. Wan and L. Jiang, *Macromol. Rapid Commun*. **2007**, *28*, 1135

[119] J. Yu, S. Holdcroft, *Chem. Commun.* **2001**, 1274.

[120] B.-J. de Gans, P.C. Duineveld, U.S. Schubert, *Adv. Mater*. **2004**, *16*, 203.

[121] J. F. Cooley, US 692,631, 1902.

[122] J. Jang, B. Lim, *Angew, Chem, Int. Ed*. **2003**, *2*, 5600.

[123] M. Trojanowicz, *Microchim. Acta*. **2003**, *143*, 75.

[124] S. Brahim, A. M. Wilson, D. Narinesingh, E. Iwuoha, A. Guiseppi-Elie, *Microchim. Acta*. **2003**, *143*, 123.

[125] M. Schierhorn, S. W. Boettcher, D. Kraemer, G. D. Stuck, M. Moskovits, *Nano Lett*. **2009**, *9*, 3262.

[126] S. -W. Zhang, T. M. Swager, *J. Am. Chem. Soc*. **2003**, *125*, 3420.

[127] Y. Ner, C. Asemota, R. R. Olson, G. Sotzing, *ACS Appl. Mater. Interfaces*. **2009**, *1*, 2093.

[128] R. A. Potyrailo, *Angew. Chem. Int. Ed*. **2006**, *45*, 702.

[129] J. I. Lee, S. H. Cho, S. -M. Park, J. K. Kim, J-. W. Yu, Y. C. Kim, T. P. Russell, *Nano Lett*. **2008**, *8*, 2315.

[130] M. E. Roberts, M. C, LeMieux, Z. Bao, *ACS Nano* **2009**, *3*, 3287.

[131] Y. Liao, C. Zhang, Y. Zhang, V. Strong, J. Tang, X.-G. Li, K. Kalantar-zadeh, E. M. V. Hoek, K. L. Wang, R. B. Kaner, *Nano. Lett*. **2011**, *11*, 954.

[132] H. Yan, H. S. Choe, S. W. Nam, Y. Hu, S. Das, J. F. Klemic, J. C. Ellenbogen, C. M. Lieber, *Nature* **2011**, 470.

[133] M. Soreni-Harari, D. Mocatta, M. Zimin, Y. Gannot, U. Banin, N. Tessler, *Adv. Funct. Mater*. **2010**, *20*, 1005.

[134] A. Star, J. -C. Gabriel, K. Bradley, G. Gruner, *Nano Lett*. **2003**, *3*, 459.

[135] H. Zheng, I. Lee, M. F. Rubner, P. T. Hammond, *Adv. Mater*. **2002**, *14*, 569.

[136] F. W. Campbell, S. R. Belding, R. Baron, L. Xiao, R.G. Compton, *J. Phys. Chem. C.* **2009**, *113*, 9053

[137] T. Wen, S. A. Majetich, *ACS Nano* **2011**, *5*, 8868.

[138] A. Vijayalakshmi, Y. Tarunashree, B. Baruwati, S. V. Manorama, B. L. Narayana, R.E. C. Johnson, N. M. Rao, *Biosens. Bioelectron.* **2008**, *23*, 1708.

[139] M. S. Makowski, A, Ivanisevic, *Small* **2011**, *7*, 1863.

[140] J. -S. Lee, M. S. Han, C. A. Mirkin, *Angew. Chem. Int. Ed.* **2007**, *46*, 4093

[141] J. Huang, S. Virji, B. H. Weiller, R. B. Kaner, *Chem. Eur. J.* **2004**, *10*, 1314.

[142] J. Liu, Y. Lin, L. Liang, J. A. Voigt, D. L. Huber, Z. R. Tian, E. Coker, B. Mckenzie, M. J. Mcdermott, *Chem. Eur. J.* **2003**, *9*, 604.

[143] J. Wang, S. Chan, R. R. Carlson, Y. Luo, G. Ge, R. S. Ries, J. R. Heath, H.-R. Tseng, *Nano Lett.* **2004**, *4*, 1693.

[144] A. K. Wanekaya, W. Chen, N. V. Myung, A. Mulchandani, *Electroanalysis* **2006**, *18*, 533.

[145] X. J. Huang, Y.-K. Choi, *Sens. Actuators B.* **2007**, *122*, 659.

[146] D. W. Hatchett, M. Josowicz, *Chem. Rev.* **2008**, *108*, 746.

[147] A. Kros, R. J. M. Nolte, N. A. J. M. Sommerdijk, *Adv. Mater.* **2002**, *14*, 1779.

[148] B. Dong, N. Lu, M. Zelsmann, N. Kehagias, H. Fuchs, C. M. S. Torres, L. Chi, *Adv. Funct. Mater.* **2006**, *16*, 1937.

[149] H. W. Park, T. Kim, J. Huh, M. Kang, J. E. Lee, H. Yoon, *ACS Nano* **2012**, *6*, 7624.

[150] V. Dua, S. P. Surwade, S. Ammu, S. Agnihotra, S. Jain, K. Roberts, S. J, Park, *Angew. Chem. Int. Ed*. **2010**, *49*, 2154.

[151] I. Willner, B. Willner, *Nano Lett.* **2010**, *10*, 3805.

[152] P.K. Mohseni, G. Lawson, C. Couteau, G. Weihs, A. Adronov, R. R. LaPierre, *Nano Lett.* **2008**, *8*, 4075.

[153] P. Wu, L. -N. Miao, E. -F. Wang, X. -G. Shao, X. -P. Yan, *Angew. Chem. Int. Ed.* **2011**, *50*, 8118.

[154] H. Yoon, *Nanomaterials* **2013**, *3*, 524.

[155] X. F. Lu, W. J. Zhang, C. Wang, T. C. Wen, Y. Wei, *Prog. Polym. Sci*. **2011**, *36*, 671.

[156] Rajesh; T. Ahuja, D. Kumar, *Sens. Actuator B Chem*. **2009**, *136*, 275.

[157] Y. Zilberman, R. Ionescu, X. Feng, K. Mullen, H. Haick, *ACS Nano* **2011**, *5*, 6743.

[158] A. J. Heeger, *Angew. Chem. Int. Ed.* **2001**, *40*, 591.

[159] Y. -Z. Long, M. -M. Li, C. Gu, M. Wan, J.-L, Duvail, Z. Liu, Z. Fan, *Prog. Polym. Sci*. **2011**, *36*, 1415.

[160] V. A. Pedrosa, X. Luo, J. Burdick, J. Wang, *Small* **2008**, *4*, 738.

[161] H. Chelawat, S. Vaddiraju, K. Gleason, *Chem. Mater*. **2010**, *22*, 2864.

[162] A. G. MacDiarmid, *Angew. Chem. Int. Ed.* **2001**, *40*, 2581.

[163] L. Huo, J. Hou, S. Zhang, H. -Y, Chen, Y. Yang, *Angew. Chem. Int. Ed.* **2010**, *49*, 1500.

[164]   S. Bencic-Nagale, T. Sternfeld, D. R. Walt, *J. Am. Chem. Soc*. **2006**, *28*, 5041.

[165]   T. J. Dale, J. Rebek,. *J. Am. Chem. Soc.* **2006**, *28*, 4500.

[166]   J. H. Wendorff, A. Greiner, *Adv. Mater.* **2009**, *21*, 3343.

[167]   T. D. Brown, P. D. Dalton, D. W. Hutmacher, *Adv. Mater.* **2011**, *23*, 5651.

[168]   A. Greiner, J. H. Wendorff, *Angew. Chem., Int. Ed.* **2007**, *46*, 5670.

[169]   M. Ma, M. Gupta, A. Li, L. Zhai, K. K. Gleason, R.E. Cohen, M. F. Rubner, G. C. Rutledge, *Adv. Mater.* **2007**, *19*, 255.

[170]   J. Jang, B. Lim, *Angew. Chem., Int. Ed.* **2003**, *42*, 5600.

[171]   A. Larforgue, L. Robitaille, *Macromolecules* **2010**, *43*, 4194.

[172]   R. Sreenivasan, K. K. Gleason, *Chem. Vap. Deposition* **2009**, *15*, 77.

[173]   J. P. Lock, S.G. Im, K. K. Gleason, *Macromolecules* **2006**, *39*, 5326.

[174]   G. Odian, [Principles of Polymerization], 4th ed.; John Wiley &Sons, Inc.: New York, **2004**

[175]   Y. Zilberman, R. Ionescu, X. Feng, K. Mullen, H. Haick, *ACS Nano* **2011**, *5*, 6743.

[176]   A. J. Heeger, *Angew. Chem., Int. Ed.* **2001**, *40*, 2591.

[177]   Y. -Z. Long, M. -M. Li, C. Gu, M. Wan, J. -L. Duvail, Z. Liu, Z. Fan, *Prog. Polym. Sci.* **2011**, *36*, 1415.

[178]   V. A. Pedrosa, X. Luo, J. Burdick, J. Wang, *Small* **2008**, *4*, 738.

[179]   H. Chelawat, S. Vaddiraju, K. Gleason, *Chem. Mater.* **2010**, *22*, 2864.

[180]   A. G. MacDiarmid, *Angew. Chem., Int. Ed.* **2001**, *40*, 2581.

[181] L. Huo, J. Hou, S. Zhang, H. -Y. Chen, Y. Yang, *Angew. Chem., Int. Ed.* **2010**, *49*, 1500

[182] Z. Liu, J. Wang, D. Xie, G. Chen, *small* **2008**, *4*, 462.

[183] L. Y. Wang, J. Luo, M.M. Maye, Q. Fan, R.D. Qiang, M.H. Engelhard, C.M. Wang, Y.H. Lin, C.J. Zhong, *J. Mater. Chem.* **2005**, *15*, 1821.

[184] E.T. Kang, Y.P. Ting, K.G. Neoh, K.L. Tan, *CRC Press, Inc., Boca Raton* **1996**, 5496.

[185] X. Zhang, S.K. Manohar, *J. Am. Chem. Soc.* **2005**, *127*, 14156.

[186] S. J. Ye, L. Fang, Y. Lu, *Phys. Chem. Chem. Phys.* **2009**, *11*, 2480.

[187] V.G. Pol, D.N. Srivastava, O. Palchik, V. Palchik, M.A. Slifkin, A.M. Weiss, A. Gedanken, *Langmuir*, **2002**, *18*, 3352.

[188] B. Zhao, Z. Liu, Z. Liu, G. Liu, Z. Li, J. Wanga, X. Dong, *Electrochemistry Communications*, **2009**, *11*, 1707.

[189] S. Ahmad, U. Riaz, A. Kaushik, and J. Alam, *J. Inorg. Organomet. Polym.* **2009**, *19*, 355.

[190] B. Dong, M. Krutschke, X. Zhang, L. Chi, H. Fuchs, *Small 2005*, *1*, 520.

[191] R. M. Eales, A. R. Hillman, *J. Mater. Sci.* **1990**, *25*, 3806.

[192] T. C. Deivaraj, N. L. Lala, and J. Y. Lee, *J. Colloid Interface Sci.* **2005**, *289*, 402.

[193] D. Hao, S. Cheng-Min, H. Chao, X. Zhi-Chuan, L. Chen, T. Yuan, S. Xue-Zhao, G. Hong-Jun, *Chin. Phys. B* **2010**, *19*, 066102.

[194] L.H. Zhang, Y.M. Zhai, N. Gao, D. Wen, S.J. Dong, *Electrochem. Commun.* **2008**, *10*, 1524.

[195] C.M. Welch, C.E. Banks, A.O. Simm, R.G. Compton, *Anal. Bioanal. Chem.* **2005**, *382*, 12.

[196] B. Zhao, Z.R. Liu, Z.L. Liu, G.X. Liu, Z. Li, J.X. Wang, X.T. Dong, *Electrochem. Commun.* **2009**, 11, 1707.

[197] Z. Liu, B. Zhao, Y. Shi, C. Guo, H. Yang, Z. Li, *Talanta*, **2010**, *81*, 1650.

[198] G. Peng, U. Tisch, O. Adams, N. Shehada, Y. Y. Broza, S. Billan, R. Abdah-Bortnyak, A. Kuten and H. Haick, *Nat. Nanotechnol.* **2009**, *4*, 669.

[199] T. H. Risby and S. F. Solga, *Appl. Phys. B.* **2006**, *85*, 421.

[200] V. T. Savolainen, K. Liesto, A. Mannikko, A. Penttila and P. J. Karhunen, *Alcohol.: Clin. Exp. Res.* **1993**, *17*, 1112.

[201] M. Phillips, J. Herrera, S. Krishnan, M. Zain, J. Greenberg, R. N. Cataneo, *J. Chromatogr. B 1999*, **729**, 75.

[202] J. Liu, X. Wang,Q. Peng, Y. Li, *Adv. Mater.* **2005**, *17*, 764.

[203] A. Manolis, *Clin. Chem.* **1983**, *29*, 5.

[204] H. Mccullough, *Clin. Chim. Acta.* **1967**, *17*, 297.

[205] S. Dubois, S. Eng, R. Bhattacharya, S. Rulyak, T. Hubbard, D. Putnam, D. J. Kearney, *Dig. Dis. Sci.* **2005**, *50*, 1780.

[206] L. Pauling, A. B. Robinson, R. Teranishi, P. Cary, *Proc. Natl. Acad. Sci. U. S. A.* **1971**, *68*, 2374.

[207] M. J. Thorpe, D. Balslev-Clausen, M. S. Kirchner, J. Ye*, Opt. Express.* **2011**, *16*, 2387.

[208] D. Mayr, T. Ma̋rk, W. Lindinger, H. Brevard, C. Yeretzian, *Int. J. Mass Spectrom.* **2003**, *223*, 743.

[209] H. Zhao, B. Rizal, G. McMahon, H. Wang, P. Dhakal, T. Kirkpatrick, Z. Ren, T. C. Chiles, M. J. Naughton, D. Cai, *ACS Nano* **2012**, *6*, 3171.

[210] F. Wang, H. Gu and T. M. Swager, *J. Am. Chem. Soc.* **2006**, *130*, 5392.

[211] F. I. Bohrer, A. Sharoni, C. Colesniuc, J. Park, I. K. Schuller, A. C. Kummel, W. C. Trogler, *J. Am. Chem. Soc.* **2006**, *129*, 5640.

[212] O. S. Kwon, J.-Y. Hong, S. J. Park, Y. Jang, J. Jang, *J. Phys. Chem. C.* **2010**, *114*, 18874

[213] H. Yoon, J. Jang, *Adv. Funct. Mater.* **2009**, *19*, 1567

[214] E. Park, O. S. Kwon, S. J. Park, J. S. Lee, S. You, J. Jang, *J. Mater. Chem.* **2012**, *22*, 1521.

[215] H. Yoon, M. Chang, J. Jang, *J. Phys. Chem. B.* **2006**, *110*, 14074

[216] H. Yoon, J.-Y. Hong, J. Jang, *Small*, **2007**, *3*, 1774.

[217] N. V. Hieu, N. Dung, P. D. Tam, T. Trung, N. D. Chien, *Sens. Actuators, B.* **2009**, *81*, 500.

[218] G. Peng, U. Tisch, O. Adams, N. Shehada, Y. Y. Broza, S. Billan, R. Abdah-Bortnyak, A. Kuten, H. Haick, *Nat. Nanotechnol.* **2009**, *4*, 669.

[219] T. H. Risby, S. F. Solga, *Appl. Phys. B.* **2006**, *85*, 421.

[220] S. V. D. Velde, M. Quirynen, P. V. Hee, D. V. Steenberghe, *Anal. Chem.* **2007**, *79*, 3425.

[221] F. Wang, T. M. Swager, *J. Am. Chem. Soc.* **2011**, *133*, 11181.

[222] K. Balasubramanian, M. Burghard, *Small*, **2005**, 1, 180.

[223] S. Banerjee, M. G. C. Kahn, S. S. Wong, *Chem.–Eur. J.* **2003**, *9*, 1898.

[224] V. Datsyuk, M. Kalyva, K. Papagelis, J. Parthenios, D. Tasis, A. Siokou, I. Kallitsis, C. Galiotis, *Carbon*, **2008**, *46*, 833.

[225] T. J. Simmons, J. Bult, D. P. Hashim, R. J. Linhardt, P. M. Ajayan, *ACS Nano*, **2009**, *3*, 865.

[226] W. Choi, S. Hong, J. T. Abrahamson, J.-H. Han, C. Song, N. Nair, S. Baik, M. S. Strano, *Nat. Med.* **2010**, *9*, 423.

[227] J. Chen, H. Liu, W. A. Weimer, M. D. Halls, D. H. Waldeck, G. C. Walker, *J. Am. Chem. Soc.* **2002**, *124*, 9034.3

[228] Y. Xing, L. Li, C. C. Chusuei, R. V. Hull, *Langmuir*, **2005**, *21*, 4185,

[229] R. V. F. Ramsey, *J. Am. Chem. Soc.* **2000**, *122*, 3254.

[230] A. Sahu, L. Qi, M. S. Kang, D. Deng, D. J. Norris, *J. Am. Chem.Soc.* **2011**, *133*, 6509.

[231] S. J. Park, O. S. Kwon, S. H. Lee, H. S. Song, T. H. Park, J. Jang, *Nano Lett.* **2012**, *12*, 5082.

[232] Y. Paska, T. Stelzner, O. Assad, U. Tisch, S. Christiansen, H. Haick, *ACS Nano*, **2012**, *6*, 335.

[233] J. L. Johnson, A. Behnam, S. J. Pearton, A. Ural, *Adv. Mater.* **2010**, *22*, 4877.

[234] L. K. Randeniya, P. J. Martin, *Carbon*, **2012**, *50*, 1786.

[235] J. Sippel-Oakley, H.-T. Wang, B. S. Kang, Z. Wu, F. Ren, A. G. Rinzler, S. J. Pearton, *Nanotechnology*, **2005**, *16*, 2218.

[236] I. Sayago, E. Terrado, E. Lafuente, M. C. Horrillo, W. K. Maser, A. M.

Benito, R. Navarro, E. P. Urriolabeiti, M. T. Martinez, J. Gutierrez, *Synth. Met.* **2005**, *148*, 15.

[237]   M. K. Kumar, S. Ramaprabhu, *J. Phys. Chem. B*. **2006**, *110*, 11291.

[238]   A. Kaniyoor, R. I. Jafri, T. Arockiadoss, S. Ramaprabhu, *Nanoscale*, **2009**, *1*, 382.

[239]   D. T. Kauffman, A. Star, *Angew. Chem., Int. Ed.* **2008**, *47*, 6550.

국문초록

정보산업의 급격한 발전에 따라 플라스틱 일렉트로닉스(plastic electronics) 소재에 대한 개발이 국제적으로 요구되고 있으며, 특히 소형, 고신뢰성, 고감도 차세대 센서 개발에 대한 관심이 지속적으로 증가하고 있다. 현재 차세대 센서용 소재관련 연구는 탄소 나노튜브, 금속 및 무기반도체 나노재료를 중심으로 활발히 진행되고 있으나 고온에서 검출물과 반응하며 작용기 도입이 어려워 낮은 감응도를 나타내는 한계를 가진다. 이에 반해 전도성 고분자는 분자설계의 다양성, 가공의 용이성, 저중량, 유연성 등과 같은 다양한 장점을 갖고 있다. 이는 전도성 고분자의 공액이중결합 구조가 가역적인 산화·환원 반응에 의해 특정 분석물에 대한 전도도, 무게, 부피, 색깔 등의 변화를 나타낼 수 있기 때문이다.

본 연구에서는 기상증착중합법을 이용하여 다차원적 전도성 고분자 나노재료를 제조하였으며, 이들의 전기적 물성을 체계적으로 고찰하였고, 화학 및 바이오 센서 응용에 대해 살펴보았다. 다차원적 전도성 고분자 나노 구조체는 표면적을 극대화함으로써 고감응성 센서를 유도할 수 있다는 장점을 가진다. 이는 전기방사 방법으로 얻어진 나노 섬유 웹이나 탄소나노튜브, 양극산화알루미늄 템플릿 기반으로 크게 피돗(PEDOT)과 폴리피롤(Pyrrole)의 단량체를 기상으로 도입하여 다차원적 고분자 나노재료를 제조하였다. 기상증착중합 시, 온도와 압력을 조절함으로써 다차원적인 구조체의 모양을 조절하였고, 이를 중합시 전류의 흐름 변화를 통하여 동역학적으로 규명하였으며, 형성된 다차원적인 구조체의 모양과 센서 성능과 상관관계가 깊다는 것을 확인하였다. 특히, 나노 섬유 웹에

형성된 다차원적 전도성 고분자 나노 구조체는 플렉시블 테스트를 수행한 결과, 매우 우수한 결과를 보였다. 이를 통해 기존의 딱딱한 전극에 반해 유기 나노 전도성 고분자를 기반으로 한 유연성을 갖는 전극의 제조에 대한 가능성 및 구체적 방법을 제시하였으며, 섬유간 브리지를 형성하고 이를 통해 표면적을 증대시킴으로써 화학/바이오 센서의 성능을 매우 향상시켰다.

또한, 양극산화알루미늄에 개시제와 금속 나노입자 전구체를 동시에 코팅하는 방식을 통해 무기물 나노입자를 함유한 대표적 전도성 고분자 폴리페돗 및 폴리피롤 나노튜브를 제조하는 방법을 제시하였으며, 환원과정 중 사용한 환원제의 농도를 조절하여 그 응용에 있어 무기물 나노입자의 개수가 성능에 미치는 의존성을 확인하였다. 이를 과산화수소에 대한 바이오센서에 응용하였다.

그 밖에, 기상증착중합으로 탄소나노튜브에 폴리피롤을 극미세하게 도입 후, 팔라듐 나노입자를 도입하여 이를 수소센서에 응용하였다.

본 연구에서 기상증착중합법을 이용하여 제조한 다차원적 전도성 고분자 나노재료는 향후 센서 이외에도 바이오 운반체, 고효율 반응막, 에너지 전기소자 등 다양한 응용분야에 폭넓게 활용될 수 있을 것으로 사료된다.

주요어: 전도성 고분자, 폴리피롤, 피돗, 기상증착중합, 화학센서, 바이오센서

학번: 2009-23949